Multi-pulse laser wakefield acceleration

Jakob Jonnerby

Merton College, Oxford

Submitted in partial fulfilment of the requirements for the degree of

Doctor of Philosophy at the University of Oxford

Hilary Term 2021

Abstract

This thesis presents results towards the realisation of high-repetition rate laser wakefield acceleration (LWFA). I have framed the contributions around the development of multi-pulse laser wakefield acceleration (MP-LWFA), which is a scheme using a train of laser pulses rather than a single pulse to excite a plasma wakefield. High energy but low peak power lasers that can reach multi-kHz repetition rates are already commercially available, and could become viable as drivers in the MP-LWFA scheme in the near future.

First, I discuss the development of a waveguiding mechanism capable of overcoming the diffraction length of the tightly focused laser pulses without suffering laser damage after continuous operation. I describe the novel solution of plasma channel waveguides and focus on the measurement of their densities using optical methods. This is challenging due to the small size ($\sim 100\,\mu$m) and often low densities ($n_e \sim 10^{17}\,\mathrm{cm}^{-3}$) of the plasma structures, leading to a low phase contrast. I discuss several techniques for measuring such structures, and methods for analysing the obtained data. Finally, I show how these methods are applied using data acquired from a recent experiment that was performed to produce plasma channels waveguides.

Second, I discuss the issue of ion motion and wakefield decay. MP-LWFA requires that the wakefields after each pulse in the train interact coherently to excite a wakefield through resonance. However, the interaction between the wakefield and the plasma ions lead to several instabilities which moves energy into other modes, eventually breaking up the wakefield. I present new experimental results measuring the wakefield decay time to be on the order of 100 plasma periods in hydrogen, which is likely to be sufficient for the MP-LWFA scheme.

Acknowledgements

Pursuing graduate studies at the University of Oxford, with its medieval colleges and libraries, academic rigour, and filled with brilliant scientists and scholars of nearly all disciplines, has been a life-changing experience. Summarising these years is nearly impossible, but they will never be forgotten.

I wish to thank of all of those who have made my journey to becoming an independent scientist so enriching. To my supervisors and co-supervisors Simon Hooker, Roman Walczak, and Laura Corner. To all the members of the Hooker group. To my friends at Merton College, and elsewhere at the University of Oxford. And finally, to all my family for supporting me. Thank you!

CONTENTS

List of Figures

LIST OF TABLES

CHAPTER 1

INTRODUCTION

Throughout history, scientific discoveries have been driven as much by the development of new tools as by the conception of new theories. For example, tools such as the polished glass lens has allowed us to study objects as far away as other galaxies and as small as individual biological cells. Sometimes making existing tools smaller and cheaper also have a profound and unexpected impact on scientific progress. For example, the invention of the transistor led to the miniaturisation of computers which allowed their use to become much more widespread in the experimental sciences and in society at large. The particle accelerator has over the past 80 years or so been one of the real workhorses of scientific discoveries; one study concluded that between 1938 and 2009, 28% of all Nobel prizes awarded in physics had direct contributions from the field of accelerator physics [1]. The laser plasma accelerator is based on the latest technological advances in laser physics and is a promising method for accelerating particles to high energies over a short distance. With a footprint small enough to fit inside a university experimental lab, their cost are a fraction of that of a modern synchrotron accelerator. In this thesis, I will investigate the road towards high-repetition rate laser plasma accelerators.

1.1 Engines of discovery

The first particle accelerators were constructed in the early 20th century by Rolf Wideroe (1928), Ernest Lawrence (1929), and John Cockroft and Ernest Walton (1932). The Cockroft-Walton generator [2], pictured in Figure 1.1a was capable of accelerating protons to an energy of 0.7 MeV, sufficient to overcome the strong force and to split atoms for the first time. Since their inception, particle accelerators have found an increasing range of applications. Synchrotron light sources such as the Diamond Light Source in the UK, Figure 1.1b, are used to study the properties of new materials and biological matter. Examples include the structure of green fluorescent protein (Figure 1.2a), used among other things for indicating gene expression, giant magneto-resistance (Figure 1.2b), the enabling principle of modern hard drives, and photo-voltaic materials (Figure 1.2c).

Particle accelerators built purposely for investigating nuclear and particle physics can be found at laboratories such as the European Organisation for Nuclear Research (CERN), where machines such as the Large Hadron Collider (Figure 1.1c) are used to study the properties of fundamental particles.

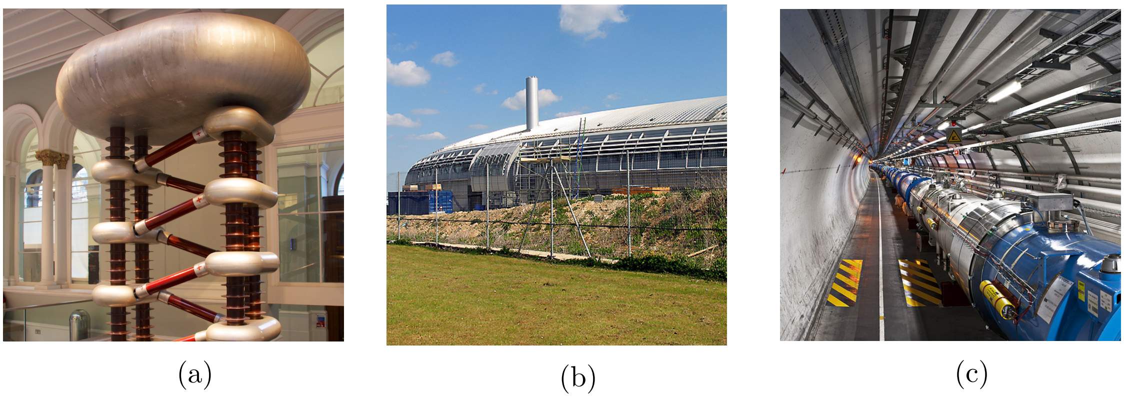
(a) (b) (c)

Figure 1.1: Historical and current particle accelerators. (a) Cockroft-Walton generator, (b) Diamond Light Source, (c) Large Hadron Collider. For image sources see end of this chapter.

(a) (b) (c)

Figure 1.2: Objects studied at synchrotron light sources. (a) E-coli bacteria expressing green fluorescent protein, (b) hard drives, (c) photo-voltaic cells. For image sources see end of this chapter.

1.2 Towards laser-driven particle accelerators

The large number of scientific applications has led to a growing interest in particle accelerators. New methods for accelerating particles are being designed that could overcome some current limitations of conventional accelerators, such as their prohibitive cost and size. One of these methods is laser plasma acceleration (LPA). The performance of LPAs in terms of generated electron beam energy has doubled approximately every 7.4 years (see Figure 1.3). The beam energy currently achievable (≥ 4 GeV) is comparable to that used in synchrotron light sources. However, other important metrics such as the beam emittance (a measure of the electron beam size in position and momentum space) and the repetition rate need to be improved in order for LPA to be useful for many applications in science and industry. In this thesis, the focus is on the issue of how to increase the repetition rate of LPAs. Current high energy ($\geq$ GeV electron energies) LPAs require relatively high intensity lasers to accelerate electrons, which means that the repetition rate currently is restricted to the $1-10$ Hz range due to heating of the optical components. Laser with lower peak power are capable of generating pulses at kHz repetition rates, and have been used to accelerate electron beams up to 5 MeV [3–6]. Low peak power lasers could also be used to excite the plasma wakefield through resonance. This scheme is known a multi-pulse laser wakefield acceleration

(MP-LWFA). In this thesis, two aspects of high-repetition rate LPAs will be covered. The first concerns the issue of plasma structures capable of guiding the drive pulse(s) over several centimetres. The second concerns the lifetime of the plasma wakefield, as this constitutes a critical limit of the feasibility of the multi-pulse scheme.

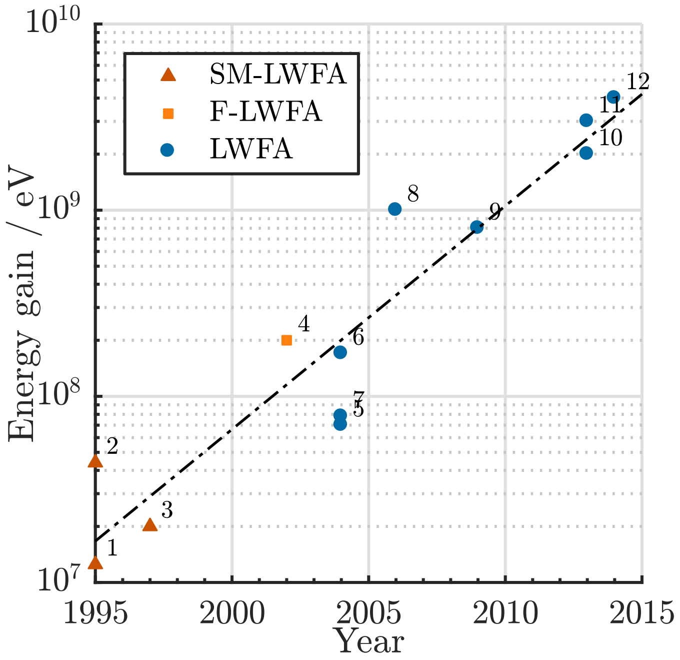

Figure 1.3: Beam energy generated by laser plasma accelerators since their inception. For references see the labels in Table 2.1.

1.2.1 High-repetition rate plasma channels

A crucial aspect of enabling high-repetition rate laser plasma accelerators is finding a device capable of guiding the high-intensity laser pulses over a long (∼ cm) distance. This is similar to how guiding in optical fibres work (Figure 1.4), except that the medium is a plasma instead of glass. In this thesis, I will focus on how to measure their structure to ensure that they have the desired properties. These methods will be covered in Chapters 3 and 4.

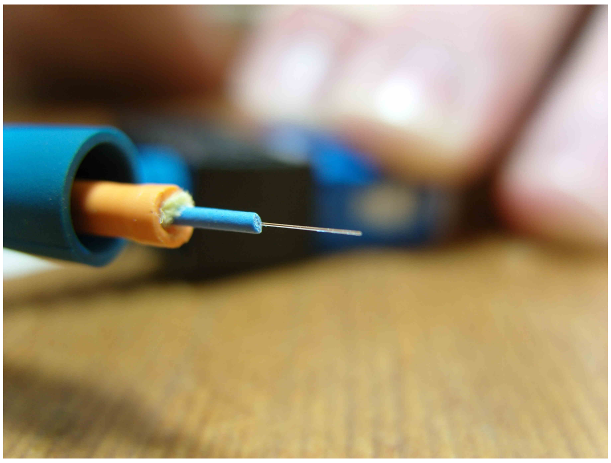

Figure 1.4: Optical fibre waveguide. For image source see end of this chapter.

1.2.2 Plasma wakefield decay

The method used to excite a high-repetition rate plasma wakefield is another important aspect. The MP-LWFA scheme could to achieve this at a repetition rate of several kHz. However, the lifetime of the plasma wakefield could limit the usefulness of this scheme. If the wakefield decays too quickly, additional pulses would not generate a higher amplitude wakefield. In Chapters 5 and 6, I investigate the causes and timescales of wakefield decay, in order to determine whether this constitutes an issue for the feasibility of MP-LWFA.

1.3 Outline of the thesis

In this thesis, I address two issues of multi-pulse laser wakefield and other high-repetition rate laser plasma acceleration schemes. The first, that of diagnosing plasma channels used for guiding high-intensity laser pulses, is covered in Chapters 3 and 4. The second issue pertains to the decay of plasma wakefields, which affects all long-pulse wakefield acceleration schemes. This is covered in Chapters 5 and 6.

CHAPTER 2 - LASER PLASMA ACCELERATION An overview of several schemes to achieve wakefield excitation: laser beatwave acceleration, self-modulated laser wakefield acceleration, laser wakefield acceleration, and multi-pulse laser wakefield acceleration. An introduction to the theory of laser-plasma acceleration is presented. I present a simple scaling law showing that the energy gain achievable in a laser-plasma accelerator stage is inversely proportional to the plasma density. I introduce the concept of ion motion, which leads to plasma instabilities and wakefield decay, and discuss its implication for long-pulse plasma acceleration schemes.

CHAPTER 3 - PLASMA DENSITY DIAGNOSTICS I introduce a theory of low-intensity laser propagation in plasma, leading to a phase shift and deflection of the laser pulse. These effects are proportional to the plasma density, providing a non-destructive method for measuring the plasma density. I present several methods of diagnosing plasma structures using lasers; shadowgraph and schlieren imaging, use of wavefront sensors, deflectometry, and interferometry. I present a novel diagnostic layout allowing the simultaneous measurement of the plasma structure from two different angles.

CHAPTER 4 - INTERFEROMETRY ANALYSIS I discuss the problem of extracting the phase from an interferogram and provide a solution for each step in this process; the phase extraction, unwrapping the phase, and methods to recreate a three-dimensional symmetric structure from a two-dimensional projection. I show that a previously developed method that enables the reconstruction of phase objects that are asymmetric in one transverse direction can be expanded to an arbitrary angle by adding a second projection axis. I provide an example analysis of interferometric data of low-density plasma channels and compare the use of the Fourier transform with the continuous wavelet transform for this purpose.

CHAPTER 5 - WAKEFIELD DECAY: THEORY AND EXPERIMENT I present several mechanisms that can lead to wakefield decay through interaction with plasma electrons and ions; Landau damping, modulational instability, and collisional damping. I provide estimates of the growth rate of each of these instabilities. I also present several methods for measuring the wakefield amplitude, both using electron beams and lasers. Previous experiments that have measured the wakefield decay rate are summarised.

CHAPTER 6 - MEASURING WAKEFIELD DECAY The results of an experiment to measure wakefield decay is presented. I outline the main difference with respect to previous experiments, and use for the first time the recently developed frequency domain holography diagnostic (FDH) to measure the wakefield decay, with the temporally encoded spectral shifting (TESS) analysis method to extract the wakefield amplitude. Finally, I discuss the implications of these measurements on the MP-LWFA and other long-pulse laser plasma acceleration schemes.

CHAPTER 7 - FREQUENCY DOMAIN HOLOGRAPHY I describe an attempt to analyse the wakefield decay data using the frequency domain holography analysis method. I show that due to a limitation in the bandwidths of the laser pulses used to measure the wakefield, this method does not accurately reconstruct the wakefield amplitude. Theoretical and numerical calculations confirm this result, and I discuss why the TESS method is not similarly affected.

Chapter 8 - Discussion and future outlook I summarise the main results of the thesis, together with a future outlook of laser plasma accelerators.

1.4 Role of the author

The main experimental data presented in Chapter 6 in this thesis were collected during an experimental campaign in September to November 2018 at the Central Laser Facility (CLF), UK. The author was responsible for designing the experiment and leading the day-to-day operations in the role of deputy target area operator. The analysis of the collected data has been carried out by the author. The results have been presented as a conference presentation at the European Advanced Accelerators Concepts Workshop 2019, and a journal publication of these results is being prepared.

The results presented in Chapter 4 were collected from a later experimental campaign in 2019, also at the CLF. Here, the author was responsible for the design of an interferometric diagnostic to measure low-density plasma channels. The results of this experiment has been published [7]. In addition the author has assisted during two earlier experimental campaigns, one at Oxford in 2017 and one at CLF in 2018. In the 2017 experiment, the author helped with day-to-day operations and in the 2018 experiment the author was responsible for setting up a transverse diagnostic and writing some of the control software for the experiment. The results of these experiments have resulted in two published articles [8, 9]. The author has also presented this work at the Advanced Accelerators Workshop at Elba in 2017 during a poster session, and again as a speaker at the John Adams Institute annual meeting in 2018.

1.5 Image sources

The Diamond Light Source Project, Chilton - geograph.org.uk - 10269.jpg. (2020, February 16). Wikimedia Commons, the free media repository. Retrieved 16:59, January 16, 2021 from https://commons.wikimedia.org/w/index.php?title=File:The_Diamond_Light_Source_Project,_Chilton_-_geograph.org.uk_-_10269.jpg&oldid=394901155.

File:Cockcroft Walton Accelerator, National Museum of Scotland.jpg. (2020, November 7). Wikimedia Commons, the free media repository. Retrieved 17:04, January 16, 2021 from https://commons.wikimedia.org/w/index.php?title=File:Cockcroft_Walton_Accelerator,_National_Museum_of_Scotland.jpg&oldid=510901791.

File:Views of the LHC tunnel sector 3-4, tirage 1.jpg. (2020, October 4). Wikimedia Commons, the free media repository. Retrieved 17:04, January 16, 2021 from https://commons.wikimedia.org/w/index.php?title=File:Views_of_the_LHC_tunnel_sector_3-4,_tirage_1.jpg&oldid=480033207.

File:Transformed E.coli using green fluorescent protein 2.jpg. (2020, October 24). Wikimedia Commons, the free media repository. Retrieved 17:06, January 16, 2021 from https://commons.wikimedia.org/w/index.php?title=File:Transformed_E.coli_using_green_fluorescent_protein_2.jpg&oldid=499068585.

Photovoltaic cell. Libreshot. Retrieved January 16, 2021 from https://libreshot.com/photovoltaic-cells/

Hard disk. Pixabay. Retrieved January 16, 20201, from https://pixabay.com/photos/hard-disk-hard-drive-hdd-5787755/

File:MultimodeFiber.JPG. (2020, August 11). Wikimedia Commons, the free media repository. Retrieved 17:11, January 16, 2021 from https://commons.wikimedia.org/w/index.php?title=File:MultimodeFiber.JPG&oldid=438780174.

Chapter 2

Laser plasma acceleration

In this chapter I give a brief overview of basic theoretical concepts of plasma wakefields that will underpin the later chapters, including the ponderomotive force and plasma oscillations. I show that the energy gain of a single accelerator stage is proportional to the inverse plasma density, which necessitates the use of low-density plasma channels capable of guiding a high-intensity laser pulse over a long distance. I also review some common laser-driven plasma accelerator schemes: laser beatwave acceleration (LBWA), self-modulated laser wakefield acceleration (SM-LWFA), laser wakefield acceleration (LWFA), and multi-pulse laser wakefield acceleration (MP-LWFA). Finally, I discuss the issue of ion motion in laser plasma accelerators.

2.1 Background

The acceleration of charged particle beams in a plasma wakefield was first envisioned by Tajima and Dawson in 1979 [10]. They noted that plasma waves could sustain strong electric fields with accelerating gradients up to three orders of magnitude greater than those of conventional accelerators. They proposed using short, intense laser pulses ($> 10^{18}\,\mathrm{W\,cm^{-2}}$) propagating through a plasma to drive a trailing wakefield, as shown

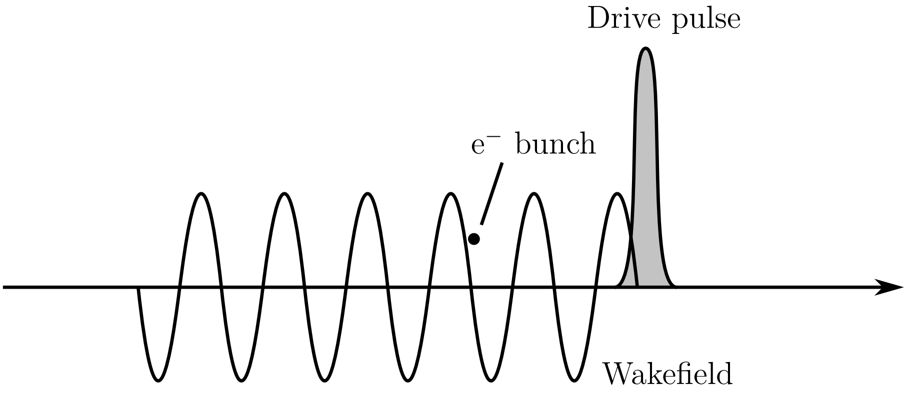

Figure 2.1: Laser wakefield acceleration.

in Figure 2.1. For suitable plasma densities ($10^{17} - 10^{18}\,\mathrm{cm}^{-3}$), the laser pulse duration would need to be less than 100 fs. However, the technology required to generate intense laser pulses this short was not available at the time. Instead, other methods had to be used generate plasma wakefield in the laboratory. I provide an overview of some of these methods in Section 2.8. First, however, I review some of the basic theory of laser plasma acceleration.

2.2 Laser ponderomotive force

A laser pulse with a finite spatio-temporal extent has an intensity gradient which causes an effective transverse and longitudinal force that pushes the plasma electrons away from the laser pulse through the ponderomotive force [11]. Once the laser pulse has propagated past the electrons, they are pulled back towards their original positions by the positive charge from the ions, and subsequently start to oscillate around the axis. The ponderomotive force for an electromagnetic wave is proportional to the gradient of the laser electric field intensity, and is equal to (following Chen [12]):

$$\mathbf{F}_{\mathrm{NL}} = -\frac{\epsilon_0 \omega_p^2}{\omega^2} \nabla \frac{\left\langle E^2 \right\rangle}{4}. \tag{2.1}$$

I obtain this expression by considering the equation of motion for a single electron in an oscillating electromagnetic field with a radial dependence $\mathbf{r}$ and frequency ω:

$$m\frac{d\mathbf{v}}{dt} = -e[\mathbf{E}(\mathbf{r},t) + \mathbf{v}\times\mathbf{B}(\mathbf{r},t)]. \tag{2.2}$$

Evaluating the electric field at the initial position $\mathbf{r}_0$ of the electron and neglecting the magnetic field, I obtain the first-order solutions for the velocity and position of the electron in the field. Expressing the electric field wave as the product of a radially-dependent envelope function $\mathbf{E}_s(r)$ and an oscillating cosinus term:

$$\mathbf{E}(\mathbf{r},t) = \mathbf{E}_s(\mathbf{r})\cos\omega t, \tag{2.3}$$

I rewrite the equation of motion (2.2) as

$$m\frac{d\mathbf{v}_1}{dt} = -e\mathbf{E}\left(\mathbf{r}_0\right), \tag{2.4}$$

with solutions for the velocity $\mathbf{v}_1$ and position $\delta\mathbf{r}_1$:

$$\mathbf{v}_1 = \frac{d\mathbf{r}_1}{dt} = -\frac{e}{m\omega}\mathbf{E}_s(\mathbf{r}_0)\sin\omega t \tag{2.5}$$

$$\delta\mathbf{r}_1 = \left(\frac{e}{m\omega^2}\right)\mathbf{E}_s(\mathbf{r}_0)\cos\omega t. \tag{2.6}$$

Next, I use these expressions in the equation of motion (2.2), to find the second-order equation of motion. No longer neglecting the magnetic field, I obtain an expression of it using:

$$\frac{d\mathbf{B}}{dt} = -\nabla\times\mathbf{E} \tag{2.7}$$

$$\mathbf{B}_1 = -\frac{1}{\omega}\nabla\times\left.\mathbf{E}_s\right|_{\mathbf{r}=\mathbf{r}_0}\sin\omega t. \tag{2.8}$$

Expanding the electric field to first order, $\mathbf{E}(\mathbf{r}) = \mathbf{E}(\mathbf{r}_0) + (\delta\mathbf{r}_1 \cdot \nabla)\,\mathbf{E}(\mathbf{r})|_{\mathbf{r}=\mathbf{r}_0}$, one may write the second-order equation of motion as:

$$m\frac{d\mathbf{v}_2}{dt} = -e\left[(\delta\mathbf{r}_1 \cdot \nabla)\,\mathbf{E} + \mathbf{v}_1 \times \mathbf{B}_1\right]. \tag{2.9}$$

Inserting equations (2.5), (2.6) and (2.8) I obtain:

$$m\frac{d\mathbf{v}_2}{dt} = -\frac{e^2}{m\omega^2}\left[(\mathbf{E}_s \cdot \nabla)\,\mathbf{E}_s \cos^2\omega t + \mathbf{E}_s \times (\nabla \times \mathbf{E}_s)\sin^2\omega t\right] \tag{2.10}$$

$$m\left\langle\frac{d\mathbf{v}_2}{dt}\right\rangle = -\frac{e^2}{m\omega^2}\frac{1}{2}\left[(\mathbf{E}_s \cdot \nabla)\,\mathbf{E}_s + \mathbf{E}_s \times (\nabla \times \mathbf{E}_s)\right], \tag{2.11}$$

where I averaged over time using $\langle\cos^2\omega t\rangle = \langle\sin^2\omega t\rangle = 1/2$. Substituting with the expansion $\mathbf{E}_s \times (\nabla \times \mathbf{E}_s) = \nabla(\mathbf{E}_s \cdot \mathbf{E}_s) - (\mathbf{E}_s \cdot \nabla)\mathbf{E}_s$ I am left with:

$$m\left\langle\frac{d\mathbf{v}_2}{dt}\right\rangle = -\frac{e^2}{m\omega^2}\frac{1}{2}\nabla(\mathbf{E}_s \cdot \mathbf{E}_s), \tag{2.12}$$

I now obtain an expression for the ponderomotive force acting on a single particle,

$$\mathbf{f}_{\mathrm{NL}} \equiv m\left\langle\frac{d\mathbf{v}_2}{dt}\right\rangle = -\frac{1}{2}\frac{e^2}{m\omega^2}\nabla E_s^2 \tag{2.13}$$

I multiply with the plasma density $n_e = \epsilon_0\omega_p^2 m_e/e^2$ to obtain the force per area. Since I assumed an electric field wave of the form $\mathbf{E}(r,t) = \mathbf{E}_s(r)\cos\omega t$ one sees that $\langle\mathbf{E}\rangle = \langle\mathbf{E}_s\rangle/2$. Making these substitutions in equation (2.13) I finally obtain the expression of the ponderomotive force in equation (2.1) [12].

2.3 Plasma oscillations

The laser ponderomotive force acts to push electrons out from the laser axis, while the much heavier, and therefore slower, ions remain in the centre and provide a restoring force for the electrons. The frequency of the resulting plasma electron oscillation can be

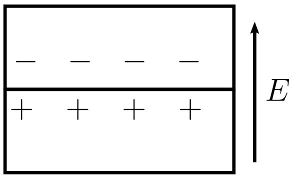

Figure 2.2: Plasma slab model of electron oscillations.

calculated from a simple model assuming an infinite slab of uncharged and homogeneous plasma. By displacing a layer of electrons with surface charge en_e by a distance x an electric field rises between the charge layers, as shown in Figure 2.2. Using Gauss's law I obtain an expression for the electric field in one dimension and neglecting the $v \times B$ term:

$$E = \frac{en_e}{\epsilon_0}x, \tag{2.14}$$

where e is the electron charge, n_e the density, and ϵ_0 the vacuum permittivity. This electric field is responsible for the restoring force and hence the motion of the electrons is given by:

$$m_e\ddot{x} = eE = -\frac{e^2 n_e}{\epsilon_0}x, \tag{2.15}$$

$$\Rightarrow \ddot{x} + \omega_p x = 0, \tag{2.16}$$

where m_e is the mass of the electrons. This is the equation for the harmonic oscillator, with ω_p the plasma electron frequency [13]:

$$\omega_p = \sqrt{\frac{e^2 n_e}{\epsilon_0 m_e}}. \tag{2.17}$$

2.4 Radial and longitudinal plasma oscillations

A two-dimensional model of non-relativistic plasma waves driven by a Gaussian laser pulse was developed by Gorbunov and Kirsanov [14]. The plasma behaviour is derived using the linear plasma fluid equations together with the plasma electrons equation of motion in a ponderomotive force field. The finite width of the drive laser pulse gives rise to oscillating plasma electric fields in both the radial or longitudinal directions. However, a laser plasma accelerator usually requires longitudinal oscillations since the electrons are accelerated along the laser axis.

The longitudinal electron density perturbation is caused by the extent of the laser pulse in time, while the radial perturbation is caused by the spatial extent of the laser. The density modulation is given by the sum of the radial and longitudinal contributions $\delta n = \delta n_r + \delta n_z$: [15]

$$\frac{\delta n}{n_e} = A\left[1+\underbrace{\left(\frac{2c}{\omega_p\sigma}\right)^2\left(1-\frac{r^2}{\sigma^2}\right)}_{\text{Radial wakefield}}\right]\exp\left(-\frac{r^2}{\sigma^2}\right)\sin\Big(\omega_p(t-z/c)\Big)\,, \tag{2.18}$$

where c is the speed of light, σ the focal spot size of the drive laser, and τ_0 the temporal duration of the drive laser. t and z are the temporal and spatial coordinates, respectively. The amplitude term A is proportional to the intensity I of the laser pulse at focus:

$$A = \frac{I\sqrt{\pi}}{c^3 n_c m_e}\left(\frac{\omega_p\tau_0}{2}\right)\exp\left[-\left(\frac{\omega_p\tau_0}{2}\right)^2\right]. \tag{2.19}$$

Here, $n_c = \epsilon_0 m_e/e^2\omega^2$ is the critical plasma density, From this equation, one can calculate the ratio between the radial and the longitudinal components of the wakefield at the centre of the laser focus:

$$\left.\frac{\delta n_r}{\delta n_z}\right|_{r=0} = \left(\frac{\lambda_p}{\pi\omega}\right)^2, \tag{2.20}$$

where $\lambda_p = 2\pi c/\omega_p$ is the plasma wavelength. This equation indicates that when the laser spot size is larger than the plasma wavelength ($\pi\sigma \gg \lambda_p$), the wakefield is mainly longitudinal, whereas when the plasma wavelength is larger ($\pi\sigma \ll \lambda_p$), the radial component is greater. I also investigate the amplitude of the radial and longitudinal oscillations as a function of plasma density. The plasma density at which the wakefield amplitude is maximised is known as the resonant density. For the longitudinal wakefield, I investigate the existence of a resonant density by calculating the derivative of equation (2.18), excluding the radial part. I find that this gives the following condition for the

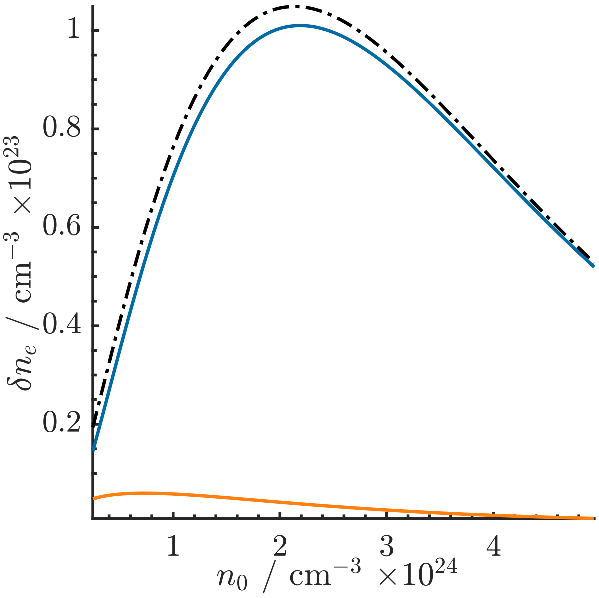

Figure 2.3: Absolute amplitudes of longitudinal and radial wakefields for a range of different plasma densities for a given laser intensity, focal spot size, and wavelength. The values of these parameters are identical to those in the experiment presented in chapter 6. The blue line shows the longitudinal wakefield amplitude, the red line the radial wakefield amplitude, and the black striped line the total wakefield amplitude.

product of the plasma frequency ω_p and the laser pulse duration τ_0:

$$\frac{d}{dn}\left(\frac{\delta n_z}{n_e}\right) = 0 \tag{2.21}$$

$$\Rightarrow \omega_p \tau_0 = \sqrt{2}. \tag{2.22}$$

For a given pulse duration, this relation indicates that the resonant plasma density that maximises the (relative) longitudinal wakefield amplitude $\delta n_z/n_0$: the one such that $\omega_p = \sqrt{n_e e^2/\epsilon_0 m_e} = \sqrt{2}\,/\tau_0$. Similarly, the (absolute) density perturbation δn_e also has a maximum at $\omega_p = \sqrt{6}\,/\tau_0$. Meanwhile, for the radial wakefield amplitude $\delta n_r/n_0$ I find that the derivative does not equal to zero for any combination of parameters ω_p and τ_0, and so it has no resonant plasma density (the amplitude keeps increasing for decreasing plasma densities). However, the absolute density perturbation δn_r has a resonance at $\omega_p = \sqrt{2}\,/\tau_0$. Figure 2.3 shows the behaviour of δn_z and δn_r as a function of the plasma background density.

2.5 Relativistic limit

In intense laser fields, the plasma electrons can acquire relativistic velocities, which modifies the dynamics of the plasma. The velocity acquired by an electron in a linearly polarized oscillating electric field is [13]:

$$v(t) = \frac{eE_0}{m_e \omega}, \tag{2.23}$$

where v is the electron velocity, e the electron charge, m_e the electron mass, E_0 the electric field amplitude, ω the laser angular frequency, and t the time. From this expression one can define the dimensionless unit a_0:

$$a_0 = \frac{eE_0}{m_e \omega c}, \tag{2.24}$$

where c is the speed of light. For $a_0 > 1$, the electrons have relativistic velocities approaching c. More commonly, a_0 can be expressed in terms of the laser intensity I and wavelength λ:

$$a_0 \approx 0.85\sqrt{I\ [10^{18}\ \mathrm{Wcm}^2])(\lambda\ [10^{-6}\ \mathrm{m}])^2}. \tag{2.25}$$

Above the relativistic limit, the plasma electron frequency and wavelength are modified:

$$\omega_p = \sqrt{\frac{e^2 n_w}{\epsilon_0 \gamma m_e}} \tag{2.26}$$

$$\lambda_p = 2\pi c\sqrt{\frac{\epsilon_0 \gamma m_e}{e^2 n_e}}, \tag{2.27}$$

where $\gamma = (1-\beta^2)^{-1/2}$ and $\beta = v/c$.

2.6 Energy gain

The maximum achievable accelerating gradient of a LWFA (in a cold, nonrelativistic plasma, i.e. $T \approx 0$ eV, $a_0 \ll 1$) is determined by the cold plasma wave breaking limit, which occurs when the velocity of the plasma electrons becomes equal to the phase velocity of the plasma wave [16, 17]. This limit can be written as [11]:

$$E[\mathrm{V/m}] \approx 96\sqrt{n_0[\mathrm{cm}^{-3}]}. \tag{2.28}$$

As an example, a plasma density of $n_e = 10^{18}$ cm^{-3} used in experiment corresponds to an accelerating gradient close to 100 GeV/m. The energy gain ΔE in a single accelerator stage is the accelerating gradient times the effective accelerator length: $\Delta E = EL_{\mathrm{Acc}}$, where E is the peak electric field in the plasma wave. For a given accelerating gradient, the total energy gain is therefore limited by the effective accelerator length. That is the shortest among the following:

- The diffraction length
- The dephasing length
- The depletion length

THE DIFFRACTION LENGTH is equal to the Rayleigh range of the laser, the distance from focus over which the laser intensity falls to below $I_{\max}/2$ (typically on the order of a few mm). The diffraction length can be overcome by the use of a guiding mechanism, either self-guiding of the laser pulse (occurs when the laser intensity is above the relativistic limit) [11] or by an external guiding structure such as a capillary discharge waveguide [18] or a plasma channel [8, 19–24] (more on this in Section 2.7).

THE DEPLETION LENGTH is the distance it takes for the drive laser to transfer all of its energy to the wakefield, which in the non-relativistic ($a_0 \ll 1$) case is given by:

$$L_{pd} = \frac{2\lambda_p^3}{\lambda_0^2 a_0^2}, \tag{2.29}$$

where λ_p is the plasma wavelength and λ_0 the laser wavelength.

THE DEPHASING LENGTH is the distance over which the accelerated electrons, with a speed close to c, move into the decelerating phase of the plasma wake, which has a group velocity less than c. This length given by the following equation, valid for $a_0 \ll 1$:

$$L_d = \frac{\lambda_p^3}{\lambda_0^2}, \tag{2.30}$$

Since $\lambda_p \propto n_e^{-1/2}$, the dephasing and depletion lengths scale as $L_d, L_{pd} \propto n^{-3/2}$. The total energy meanwhile scales as (using Eq. (2.29)) $\Delta E \propto EL \propto n^{1/2}n^{-3/2} = n^{-1}$ which means that the use of lower plasma densities allows for longer accelerating lengths and thus higher energy gains. The benefit of using low-density plasma channels is demonstrated in Figure 2.4, using data from Table 2.1, where one observes that the energy gains in previous laser plasma acceleration experiments follow this simple scaling law.

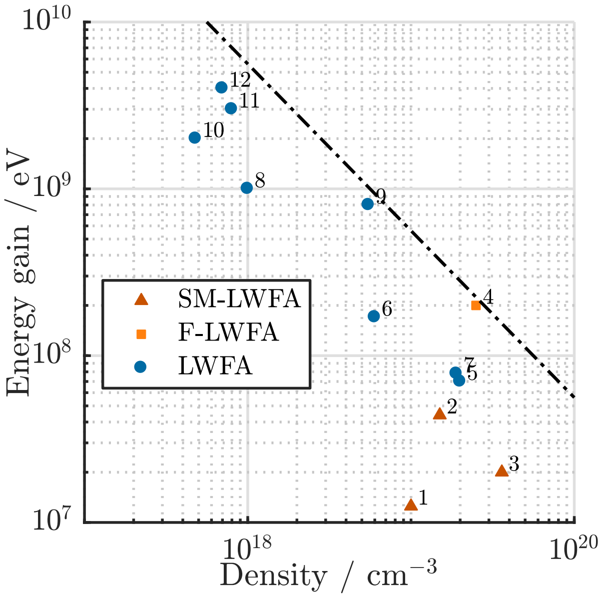

Figure 2.4: Plot showing the plasma density used and energy gain observed in previous laser plasma acceleration experiments. The black line shows the scaling law $\Delta E = EL_d$ (using the dephasing length L_d as the limiting factor) with a drive laser wavelength $\lambda_0 = 800$ nm, driving a wakefield at the wave breaking limit. The references for each experiment are listed in table 2.1

2.7 Plasma waveguides

In the previous section I discussed the diffraction length that limits the energy gain achievable in a single acceleration stage. Pre-formed plasma waveguides is one method that has been successfully used to guide the drive laser over distances much longer than the Rayleigh range (∼ centimetre) distance. In general, gradient refractive index waveguides consist of a high refractive index material in the centre of the waveguide and a lower refractive index material on the edge. In this case total internal reflection occurs, which is what enables light to be guided in optical fibres. This is because the refractive index of glass is higher than that of air. In a plasma channel, where the refractive index depends on the plasma density, similar guiding is achieved by manipulating the

Table 2.1: Experimental parameters used in previous laser plasma acceleration experiments. ΔE: observed energy gain, I_L: laser intensity at focus, n_0: plasma density

Year	Source	Reference	Experiment	ΔE / MeV	I_L / Wcm^{-2}	n_0 / cm^{-3}	Label
1995	K. Nakajima et al. Physical Review Letters. (1995);	[25]	SM-LWFA	12.5	1×10^{17}	1×10^{19}	1
1995	A. Modena et al. Nature. (1995);	[26]	SM-LWFA	44	6×10^{18}	1.5×10^{19}	2
1997	R. Wagner et al. Physical Review Letters. (1997)	[27]	SM-LWFA	20	4×10^{18}	3.6×10^{19}	3
2002	V. Malka et al. Science. (2002)	[28]	F-LWFA	200	3×10^{18}	2.5×10^{19}	4
2004	S. P. D. Mangles et al. Nature. (2004);	[29]	LWFA	70	2.5×10^{18}	2×10^{19}	5
2004	J. Faure et al. Nature. (2004).	[30]	LWFA	170	3.2×10^{18}	6×10^{18}	6
2004	C. Geddes et al. Nature. (2004);	[31]	LWFA	78	1×10^{19}	1.9×10^{19}	7
2006	W. P. Leemans et al. Nature Physics. (2006)	[32]	LWFA	1000	1×10^{18}	1×10^{18}	8
2009	S. Kneip et al. Physical Review Letters. (2009).	[33]	LWFA	800	1.9×10^{19}	5.5×10^{18}	9
2013	X. Wang et al. Nature Communications. (2013).	[34]	LWFA	2000	7×10^{19}	4.8×10^{17}	10
2013	H. T. Kim et al. Physical Review Letters. (2013)	[35]	LWFA	3000	3×10^{19}	8×10^{17}	11
2014	W. P. Leemans et al. Physical Review Letters. (2014)	[36]	LWFA	4000	4.7×10^{18}	7×10^{17}	12

plasma into a certain structure. Because the refractive index decreases with increasing electron density, plasma waveguides require higher densities on the edges than in the centre. This can be seen in the following equation for the refractive index $\eta(r)$ for non-relativistic plasmas, where r is the radius of an assumed axisymmetric plasma channel [37]:

$$\eta(r) = \sqrt{1 - \frac{\omega_p^2}{\omega_0^2}} \simeq 1 - \frac{\omega_\mathrm{p}^2}{2\omega^2}\frac{n_e(r)}{n_0}, \tag{2.31}$$

where $n_e(r)$ is the transverse electron density profile, n_0 the background density, ω_0 the laser frequency, and ω_p the plasma frequency. In underdense plasmas, the plasma to laser frequency ratio satisfies $\omega_p^2/\omega_0^2 \ll 1$. Plasma density profiles with the desired guiding properties have previously been achieved in capillary discharge waveguides [18], where plasmas are generated by a high-voltage discharge in a small diameter gas-filled capillary laser-machined through a sapphire block. Heated electrons from the centre of the capillary thermalise with the cold sapphire, forming a cold, dense plasma near the capillary wall, and a relatively warm, low-density plasma on axis. Capillary waveguides have been successful used to reach high energies [36]. However, the walls of the capillary would be damaged even when hit infrequently by the laser beam which would would burn and eventually destroy the capillary.

Plasma waveguides have also been created hydrodynamically. Here, the plasma is pre-heated through collisional ionisation using a long ($\sim$ ps) laser pulse, causing the plasma to expand outward into the surrounding gas at a speed greater than the local sound speed [19]. This generates a shock wave at the gas-plasma interface, leaving a density minimum in the centre of the plasma channel. A similar approach developed by the author's group is to use a shorter ($\sim$ fs), more intense laser pulse that heats the plasma through optical field ionisation (OFI) where the ionised electrons acquire the excess energy of the ionising laser electric field as kinetic energy. Earlier work on OFI-heated plasma channels [21, 38], showed that plasma channels are formed at densities on the order of $10^{18}\,\mathrm{cm}^{-3}$. At lower densities, on the order of $10^{17}\,\mathrm{cm}^{-3}$, measuring the plasma density profiles becomes challenging due to the low phase contrast of the channels. Methods for diagnosing these low density channels, which were partly developed by me, are discussed in Chapters 3 and 4, and have been used to successfully diagnose plasma channels with on-axis densities as low as $n_e(0) \simeq 10^{17}\,\mathrm{cm}^{-3}$ [22–24].

2.8 Laser plasma acceleration methods

2.8.1 Plasma beatwave acceleration

One of the earliest methods to excite a plasma wakefield was the the plasma beat-wave accelerator (PBWA) [39]. Here, two laser pulses of different frequencies ω_1 and ω_2 interfere to generate beats with frequency $\Delta\omega = \omega_2 - \omega_1$. By choosing ω_1, ω_2, and n_e the beat distance can be made equal to the plasma wavelength λ_p, as shown in Figure 2.5. The concept was first experimentally demonstrated in the 1990s [40, 41], and in 1993 Clayton [42] was the first to demonstrate electron acceleration in a PBWA. In that experiment, a CO_2 laser was used to produce two beams with wavelengths $\lambda_1 = 10.59\,\mu\mathrm{m}$ with $(60 \pm 10)\,\mathrm{J}$ and $\lambda_2 = 10.29\,\mu\mathrm{m}$ with $(10 \pm 5)\,\mathrm{J}$. Electrons were externally injected into the wakefield with an energy of 2.1 MeV and accelerated up to 9.1 MeV. The accelerator length of 3.2 cm (limited by the Rayleigh length of the drive laser) implied an accelerating gradient of 0.7 GeV/m. A drawback of the PBWA scheme is that as the wakefield amplitude grows, the wavelength increases due to relativistic effects. If the beatwave pattern is constant, it will eventually become out of phase with the wakefield, limiting the maximum amplitude achievable [11]. In addition, it is also vulnerable to several instabilities, such as the modulational instability, which will be discussed later.

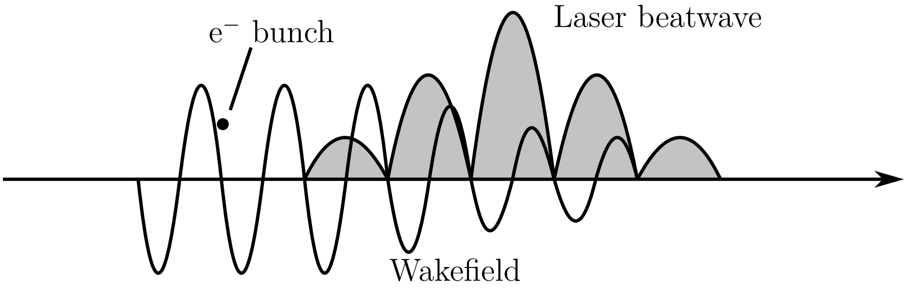

Figure 2.5: Laser beatwave acceleration.

2.8.2 Self-modulated laser wakefield acceleration

Another way to excite a plasma wakefield using a longer laser pulse is by exploiting instabilities through the propagation through the plasma to break up the longer pulse into shorter pulses, with lengths similar to the plasma wavelength. This scheme, known as self-modulated laser wakefield acceleration (SM-LWFA) was described theoretically by Esarey et al. [43]. For pulses with an optical power exceeding the critical power threshold $P > P_{\text{crit}}$, where $P_{\text{crit}} = 17(\omega/\omega_p)^2$, the plasma wake structure starts behaving like a lens and periodically focuses and diffracts the laser beam. In low-density regions of the wake the laser is focused, while in the high-density regions the plasma has a defocusing effect on the laser. The increase in laser intensity in turn drives up the amplitude of the wakefield, further increasing the focussing effect. This process, known as the self-modulation instability, acts to break up the long laser pulse into a series of shorter pulses that excite a wakefield, as shown in Figure 2.6. An advantage of SM-LWFA is that the modulations remain in phase with the wakefield even as the amplitude grows, which enables higher amplitudes to be reached. This method was first demonstrated experimentally by Coverdale et al. [44] and Modena et al. [26]. In the former experiment, a 600 fs long laser pulse with a wavelength of 1053 nm and energy of 3 J was focused to a spot with intensity $10^{18}\,\mathrm{W\,m^{-2}}$ ($a_0 = 0.9$). As it propagated through the plasma, the laser pulse decayed into a plasma wave with frequency ω_p and two forward-propagating daughter waves with frequencies $\omega_0 - \omega_p$ and $\omega_0 + \omega_p$. The first

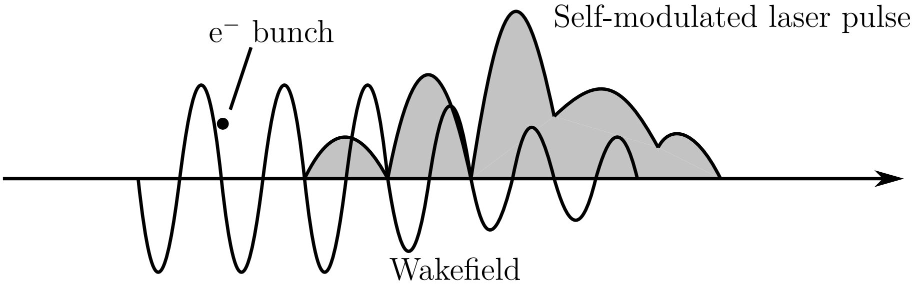

Figure 2.6: Self-modulated laser wakefield acceleration.

is referred to as the 'Stokes' scattered wave and the second as the 'Anti-Stokes' scattered wave. By measuring the laser spectrum after the plasma, a peak corresponding to the Anti-stokes scattered wave was detected, which confirmed the presence of a wakefield. Electrons accelerated up to 2 MeV were detected by a spectrometer. In the latter experiment, electrons were accelerated up to 44 MeV with the use of a 0.8 ps long pulse with a wavelength of 1054 μm, achieving an intensity on target of $6 \times 10^{18}\,\mathrm{W\,cm^{-2}}$.

2.8.3 Laser wakefield acceleration

The development of new laser technology opened up the possibility of testing the theories of Tajima and Dawson in the short-pulse regime that they had originally considered. Chirped pulse amplification (CPA), invented by Mourou and Strickland in 1985 [45] (for which both were subsequently awarded the Nobel prize in physics in 2018), allowed the generation of pulses with high peak intensity and temporal duration below 100 fs. The use of CPA laser systems allowed researchers to demonstrate electron acceleration up to 100 MeV [29–31], with a small ($< 3\,\%$) energy spread and high beam charge (22 pC). This development has since continued and several experiments have reported energy gains above 1 GeV [32, 35, 46, 47] using CPA laser systems. The highest energy gains reported so far is 4.2 GeV [36], and more recently 8 GeV [48]. Several design studies are under way to develop LWFA-based facilities and achieve energies exceeding 10 GeV [49, 50].

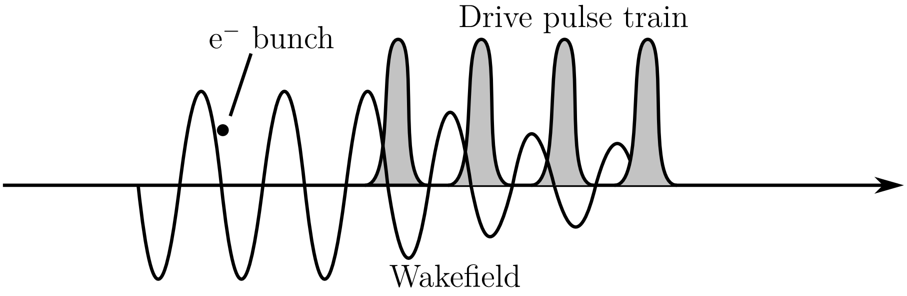

Figure 2.7: Multi-pulse laser wakefield acceleration.

2.8.4 Multi-pulse laser wakefield acceleration

While CPA based lasers have been remarkably successful in producing plasma accelerated electron beams with energies reaching several GeV, they are still fundamentally limited by the relatively poor thermal properties of the gain media. The cooling requirements limits the operation of the laser to a repetition rate to a few Hz (for high energy electron generation), far from the 100's of kHz operation that conventional accelerators are capable of [13]. Relatively lower electron acceleration, up to 5 MeV, have been achieved at kHz repetition rates [3–6]. The low energy efficiency of high intensity lasers is also problematic, since less than 0.1% of the supplied electrical energy is converted to laser energy [51]. Moreover, the single pulse LWFA requires high intensity focus comparable to the plasma wavelength, around 30 μm. This requires large optics with long focal lengths, which takes up space and makes acceleration in several stages more difficult if each stage is to be driven by a single pulse [52]. Multi-pulse laser wakefield acceleration (MP-LWFA), Figure 2.7, builds on the idea of the beat-wave accelerator originally proposed by Tajima and Dawson in 1979 [10]. It has been proposed as a way to overcome some of the challenges with LWFA, by using a different class of lasers with much higher energy efficiency and repetition rates on the order of 10 kHz. For example, commercially developed thin-disc or fibre lasers could be used as the wakefield driver. Commercial fibre lasers can operate with a wall-plug efficiency (electrical energy to optical energy) exceeding 50%[*]. MP-LWFA uses a pulse train, where each pulse is spaced by the plasma wavelength λ_p, to excite a wakefield through resonance. Since the energy is spread over several pulses, the peak intensity of each pulse is lower, potentially limiting the damage on optical elements. Several schemes have been proposed that could be used to generate a pulse train for MP-LWFA: coherent combination of laser pulses [53], divided pulse amplification [54], beam splitters and delay lines [55], and beat wave-type interference of chirped pulses [56].The first experimental demonstration of the MP-LWFA concept was recently reported [57]. In this work, two interfering chirped pulses were used to create a train of 7 pulses and used it to excite a $\delta n_e/n_0 = 1\%$ plasma wake. Another potential benefit of MP-LWFA compared to LWFA is that under optimal conditions it can be more efficient than single-pulse excitation, since the timing between each subsequent pulse can be adapted to the increasing plasma wavelength [58].

2.9 Ion motion

In this chapter, I have so far assumed that ions do not move and do not contribute to the dynamics of the wakefield, other than giving rise to the restoring force as a constant positive background. While they can be assumed to be stationary over the short timescale of a single laser pulse, this assumption no longer holds after the characteristic timescale of ion motion:

$$\tau_i = \frac{2\pi}{\omega_{pi}} \tag{2.32}$$

$$\omega_{pi} = \sqrt{\frac{Z^2 n_i e^2}{m_i \epsilon_0^2}}, \tag{2.33}$$

---

[*] For an example of this, see https://www.ipgphotonics.com/en/products/lasers/high-power-cw-fiber-lasers/1-micron/yls-eco-1-10-kw

where ω_{pi} is the plasma ion frequency, Z the atomic number, n_i the ion density, m_i the ion mass, e the atomic charge, and ϵ_0 the vacuum permittivity. The long-term evolution and eventual decay of a plasma wake is dominated by the dynamics of plasma ions. The above equation shows that the determining factor is the charge to mass ratio Z/m_i of the plasma species (for a given electron density $n_e = Zn_i$) — the lower this ratio, the slower the onset of ion motion. Ion acoustic waves, the plasma equivalent to sound waves in conventional fluids also arise and are driven either by thermal pressure or the ponderomotive pressure from a wakefield [59]. These are different from electron plasma waves, since there is no restoring force — when ions move, the much lighter electrons follow and maintain quasi-neutrality in the plasma. This process leads to density perturbations which trap and modulate electron plasma waves, resulting in the break-up of wakefields and energy eventually dissipating into thermal motion. Due to its longer timescale, ion motion is relevant for all plasma acceleration schemes with laser or particle drivers with lengths greater or equal to the ion timescale $\sigma_z \geq c\tau_i$. In the case of MP-LWFA, simulations have shown that after about $N \approx 70$ pulses the wakefield starts to deteriorate due to ion motion in a hydrogen plasma and after $N \approx 120$ pulses in a xenon plasma [60]. Another case where ion motion is relevant is the proton-driver wakefield accelerator (PDWFA) (for example the AWAKE project at CERN [61]), which uses long ($\sigma_z \approx 10$ cm) proton bunches. It relies on the self-modulation instability to shape the particle beam into a train of smaller bunches, each on the scale of the plasma wavelength (10 μm). Ion motion stops this process from fully developing a modulated beam, which limits the achievable accelerating gradient. Simulations have showed that higher charge-to-mass ratio plasma species yielded higher amplitude wakefields in this case [59]. The processes leading the decay of plasma wakefields will be covered in Chapter 5, and the results of an experiment to measure the wakefield lifetime is presented in Chapter 6.

CHAPTER 3

PLASMA DENSITY DIAGNOSTICS

3.1 Plasma diagnostics for LWFA

The plasma medium is of central importance to both laser-driven and particle-driven wakefield acceleration, as its characteristics determines the performance of the accelerator. Of principal interest is the plasma number density, spatial homogeneity, temporal stability, and shape. In this chapter I cover the principle diagnostic methods for determining the plasma density by means of optical probes (methods for measuring plasma wakefields are covered in a later chapter). The main benefit of light-based probing is that it is fast enough (sub-ps) to capture plasma dynamics on the temporal scale which is relevant for applications in LWFA. Furthermore, in the case of LWFA, there is already a high-performance laser with pico or femto-second resolution used for experiments, and so it is convenient to use a small fraction of the available laser energy to probe the resulting plasma.

3.1.1 Uses of plasma diagnostics

Knowledge of the plasma density is important for LWFA since it determines both the accelerating field strength, the dephasing length, and the depletion length. As I discussed in Chapter 2, current developments in LWFA favours the production of centimetre long plasma cells with low plasma densities (10^{16}-$10^{17}\,\mathrm{cm}^{-3}$). In order to guide the driving laser pulse over that distance, guiding plasma structures are needed where high sensitivity diagnostics are used to infer the on-axis density, as well as the height, width, and thickness of the surrounding plasma walls.

3.1.2 Light-based plasma diagnostics

In this chapter I will focus on light-based methods for measuring plasma densities, since they are sensitive enough to measure the low plasma densities required for LWFA, and fast enough to capture the relevant dynamics. The techniques covered have been used for many different experiments in the field. I begin with two “qualitative” methods which rely on measuring changes in the intensity of the probe pulse to infer either the first order derivative of the plasma refractive index, as in schlieren imaging, or the second order derivative, as in shadowgraph imaging. The rest of methods covered are more sensitive and work either by measuring the wavefront directly, measuring the difference in the group delay between two pulses on a spectrometer (group velocity technique and two-colour spectral interferometry), interfering two pulses to generate a fringe pattern on a camera (interferometry), or measuring the deflection angle with the use of a grating pair (moiré deflectometry). Before I describe each method in more detail, I will show how the propagation of a laser pulse through a plasma generates a measurable quantity (the phase), which is proportional to the density.

3.2 Electromagnetic waves in plasma

Electromagnetic waves in the form of laser light is commonly used to measure plasma densities. Here I show how the interaction with a plasma causes the electromagnetic wave to acquire a phase shift relative to an identical wave that propagated through vacuum. Consider Maxwell-Faraday's equation and Amperès law in vacuum together with a plasma current (see Hutchinson [62] for a full derivation of these results):

$$\nabla \times \mathbf{E} = -\frac{\partial \mathbf{B}}{\partial t}, \quad \nabla \times \mathbf{B} = \mu_0 \mathbf{j} + \varepsilon_0 \mu_0 \frac{\partial \mathbf{E}}{\partial t},$$

where μ_0 and ϵ_0 are the permeability and emittivity of vacuum. The plasma effects are captured by the plasma current $\mathbf{j}$. Combining these two equations yields the wave equation in a medium:

$$\nabla \times (\nabla \times \mathbf{E}) + \frac{\partial}{\partial t}\left(\mu_0 \mathbf{j} + \varepsilon_0 \mu_0 \frac{\partial \mathbf{E}}{\partial t}\right) = 0 \tag{3.1}$$

In an isotropic and homogeneous plasma one is be able to assume solutions of the form $\exp(\mathrm{ik} \cdot \mathbf{r} - \mathrm{i}\omega t)$, however since plasma structures are not necessarily homogeneous I instead use the Wentzel, Kramers, and Brillouin (WKB) approximation. Here one assumes that the scale length of the variations in the plasma, L, is much longer than the plasma wavelength $L \gg \lambda$. One can also write this as $2\pi(kL)^{-1} \ll 1$, where k is the plasma wave number $k = 2\pi/\lambda$ [63]. Starting with rearranging equation (3.1), replacing $c = 1/\sqrt{\varepsilon_0 \mu_0}$:

$$c^2 \nabla \times (\nabla \times \mathbf{E}) + \frac{\partial}{\partial t}\left(\frac{1}{\varepsilon_0}\mathbf{j} + \frac{\partial \mathbf{E}}{\partial t}\right) = 0. \tag{3.2}$$

I then look for solutions $\mathbf{E} = \tilde{\mathbf{E}} \exp\{i\,[\int \mathbf{k}(\mathbf{r}) \cdot \mathbf{dr} - \omega t]\}$, where $\tilde{\mathbf{E}}$ is the electric field amplitude, so that I replace $\nabla \mathbf{E} \to \exp\{i\,[\int \mathbf{k}(\mathbf{r}\} \cdot \mathbf{dr} - \omega t])(\nabla + i\mathbf{k})\tilde{\mathbf{E}}$ and $\partial \mathbf{E}/\partial t \to -i\omega \mathbf{E}$. I also assume that the current is linear in $\mathbf{E}$, so that $\mathbf{j} = \sigma \mathbf{E}$, where $\boldsymbol{\sigma}$ is the conductivity of the plasma.

$$\frac{c^2}{\omega^2}(\mathbf{k}-\mathrm{i}\nabla)\times[(\mathbf{k}-\mathrm{i}\nabla)\times\tilde{\mathbf{E}}] = -\tilde{\mathbf{E}} - \frac{\mathrm{i}}{\epsilon_0\omega}\mathbf{j} \tag{3.3}$$

$$= -\left(\mathbf{I} + \frac{\mathrm{i}}{\epsilon_0\omega}\sigma\right)\tilde{\mathbf{E}} \tag{3.4}$$

$$= -\boldsymbol{\epsilon}\cdot\tilde{\mathbf{E}}, \tag{3.5}$$

where $\mathbf{I}$ is the unity matrix and ϵ the dielectric tensor of the plasma:

$$\boldsymbol{\epsilon} = \left(\mathbf{I} + \frac{\mathrm{i}}{\epsilon_0\omega}\boldsymbol{\sigma}\right). \tag{3.6}$$

I have assumed that the spatial variations are slow compared to the wavelength of the laser pulse. One can therefore expand $\tilde{\mathbf{E}}$ into zero and first orders in $(kL)^{-1}$: $\tilde{\mathbf{E}} \approx \tilde{\mathbf{E}}_0 + \tilde{\mathbf{E}}_1$. Since terms $\nabla\tilde{\mathbf{E}} \approx \nabla\tilde{\mathbf{E}}_0 + \nabla\tilde{\mathbf{E}}_1 = \nabla\tilde{\mathbf{E}}_1$ and $\tilde{\mathbf{E}}_1$ are small compared to $\tilde{\mathbf{E}}_0$ they may be neglected [63]. With these approximations, replacing $\mathbf{k} = k\hat{\mathbf{k}}$, with $\hat{\mathbf{k}}$ a unit vector, I obtain:

$$\left[\frac{c^2k^2}{\omega^2}(\hat{\mathbf{k}}\hat{\mathbf{k}} - \mathbf{I}) + \boldsymbol{\epsilon}\right]\cdot\tilde{\mathbf{E}}_0 = 0, \tag{3.7}$$

which is the plasma dispersion relation. In order solve it, I need an expression for $\boldsymbol{\epsilon}$ and $\boldsymbol{\sigma}$. Assuming a linear plasma, the current can be expressed as:

$$\mathbf{j} = -en_e\mathbf{v} = \boldsymbol{\sigma}\cdot\mathbf{E}. \tag{3.8}$$

In order to find $\boldsymbol{\sigma}$ I need an expression for the plasma velocity $\mathbf{v}$. I do this starting from the equation of motion of a single particle in an electromagnetic field:

$$m_e\frac{\partial\mathbf{v}}{\partial t} = -e\left(\mathbf{E} + \mathbf{v}\times\mathbf{B}_0\right). \tag{3.9}$$

The Lorenz force on a single, nonrelativistic electron of the laser magnetic field $\mathbf{B}_0$ is small compared to that of the electric field [*]. Therefore I will neglect it and obtain:

$$-m_e i\omega\mathbf{v} = -e\mathbf{E} \tag{3.10}$$

$$\mathbf{v} = -\frac{ie}{m_e\omega}\mathbf{E}. \tag{3.11}$$

From equation (3.8) I can now identify:

$$\boldsymbol{\sigma} = \frac{in_e e^2}{m_e\omega}\mathbf{I} \tag{3.12}$$

$$\boldsymbol{\epsilon} = \left(\mathbf{I} + \frac{\mathrm{i}}{\epsilon_0\omega}\boldsymbol{\sigma}\right) = \left(1 - \frac{n_e e^2}{\epsilon_0 m_e\omega^2}\right)\mathbf{I} = \left(1 - \frac{\omega_p^2}{\omega^2}\right)\mathbf{I}, \tag{3.13}$$

where I have used the the definition of the plasma frequency: $\omega_p^2 = n_e e^2/\epsilon_0 m_e$. I now proceed to solve the dispersion relation in equation (3.7) by inserting the expression for $\boldsymbol{\epsilon}$:

$$\left[\frac{c^2k^2}{\omega^2}(\hat{\mathbf{k}}\hat{\mathbf{k}} - \mathbf{I}) + \left(1 - \frac{\omega_p^2}{\omega^2}\right)\mathbf{I}\right] \cdot \tilde{\mathbf{E}}_0 = 0, \tag{3.14}$$

and one sees that for transverse electric fields, i.e. $\mathbf{k} \perp \tilde{\mathbf{E}}_0$, I obtain the following solution:

$$\frac{c^2k^2}{\omega^2} = \left(1 - \frac{\omega_p^2}{\omega^2}\right). \tag{3.15}$$

Using the standard expression for the refractive index η I finally obtain:

$$\eta = \frac{ck}{\omega} = \sqrt{1 - \frac{\omega_p^2}{\omega^2}}. \tag{3.16}$$

---

[*] For a fully relativistic electron, $v \approx c$, the magnetic field contribution to the Lorenz force would be equal to that of the electric field.

This result shows us that in the linear regime, with a probe beam that interacts weakly with the plasma, and with slowly varying plasma features, $\mathbf{E} = \tilde{\mathbf{E}} \exp(i \left[\int \mathbf{k} \cdot \mathbf{dr} - \omega t\right])$ is a solution to the wave equation 3.1. One sees that in the case where the magnetic field of the electromagnetic wave is much weaker than the electric field, I obtain the dispersion relation 3.15 and an expression for the refractive index in equation 3.16. The phase acquired by a probe beam propagating along z is therefore:

$$\begin{aligned} \phi &= \int k dz && (3.17) \\ &= \int \frac{\eta\omega}{c} dz = \int \frac{\omega}{c}\sqrt{1 - \frac{\omega_p^2}{\omega^2}} dz. && (3.18) \end{aligned}$$

For a plasma density $n_e \sim 1 \times 10^{18}\,\mathrm{cm}^{-3}$, the plasma frequency is approximately $\omega_p \sim 50\,\mathrm{THz}$, which I compare to the frequency of a laser of wavelength $\lambda = 800\,\mathrm{nm}$, $\omega \sim 2400\,\mathrm{THz}$. Therefore $\omega_p \ll \omega$ and I expand the square root term above:

$$\begin{aligned} \phi &\approx \int \frac{\omega}{c}\left(1 - \frac{\omega_p^2}{2\omega^2}\right) dz && (3.19) \\ &= \int \left(\frac{\omega}{c} - \frac{\omega_p^2}{2\omega c}\right) dz && (3.20) \\ &= \int \left(\frac{\omega}{c} - \frac{n_e e^2}{2\epsilon_0 m_e \omega c}\right) dz && (3.21) \\ &= \int \left(\frac{\omega}{c} - \frac{n_e e^2 \lambda}{4\pi\epsilon_0 m_e}\right) dz. && (3.22) \end{aligned}$$

By comparing the phase with that of another laser pulse which has propagated the same distance in vacuum, with a phase shift $\phi_0 = \int (\omega/c) dz$ one obtains:

$$\Delta\phi = \phi - \phi_0 = \int \frac{n_e e^2 \lambda}{4\pi\epsilon_0 m_e} dz. \quad (3.23)$$

In order to measure the integrated density along some line of sight in a plasma, it therefore suffices to measure the integrated phase of a probe beam and compare with the phase of a similar beam which has propagated through vacuum.

3.2.0.1 Deflection angle

It is also worth noting that there is a clear connection between the phase of the beam and the deflection angle, and this is used in many diagnostic methods which are sensitive to the deflection angle rather than the phase. The local angle of the wavefront with respect to the transverse axis y is [62]

$$\theta = \frac{\lambda}{2\pi}\frac{\partial\phi}{\partial y}.$$

The derivative of ϕ with respect to y is given by:

$$\frac{\partial\phi}{\partial y} = \int\left(\frac{e^2\lambda}{4\pi\epsilon_0 m_e}\frac{\partial n_e}{\partial y}\right)dz, \tag{3.24}$$

and therefore:

$$\theta = \frac{\lambda}{2\pi}\frac{\partial\phi}{\partial y} = \int\left(\frac{e^2\lambda^2}{8\pi^2\epsilon_0 m_e}\frac{\partial n_e}{\partial y}\right)dz. \tag{3.25}$$

3.3 Qualitative methods

3.3.1 Schlieren and shadowgraph imaging

Two common and relatively simple methods for obtaining qualitative imaging of a plasma structure are schlieren and shadowgraph imaging.

In schlieren imaging, a knife edge is placed in the focal position of an imaging lens located after the plasma. A small deflection angle caused by a density gradient in the plasma is given by equation (3.25)

$$\theta = \int\left(\frac{e^2\lambda^2}{8\pi^2\epsilon_0 m_e}\frac{\partial n_e}{\partial y}\right)dz$$

leads to a deviation of the beam path and a change in the intensity pattern in the

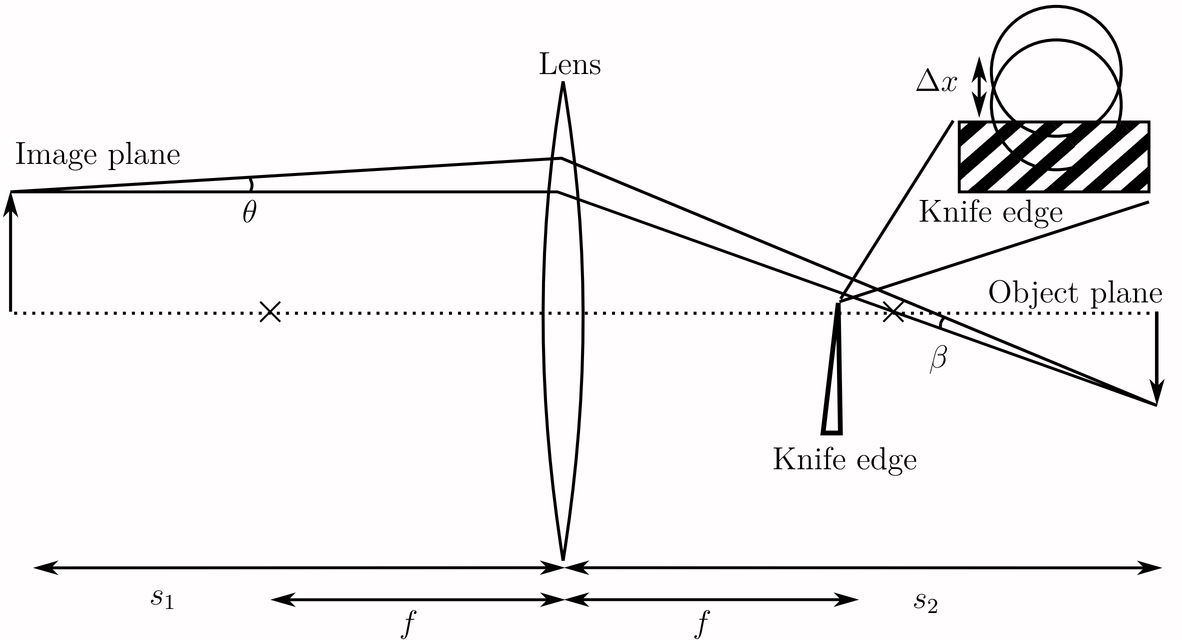

Figure 3.1: Schematic drawing of a schlieren imaging setup. A ray deflected in a plasma with an angle θ produces a focal spot that is shifted by Δx with respect to an unperturbed beam, leading to a difference in intensity at the object plane.

image plane that is proportional to the angle of deflection. I show this by considering the angle emerging from a plasma at a distance s_1 from focusing lens with focal length f_2, and study the intensity at the image plane s_2. Using the thin lens formula, these quantities are related by:

$$\frac{1}{s_1} + \frac{1}{s_2} = \frac{1}{f}. \tag{3.26}$$

In Figure 3.1, one sees that the relation between the angle of deflection θ, and the angle at which the ray approaches the focus is

$$\theta s_1 \approx \beta s_2, \tag{3.27}$$

for small angles. The knife edge at focus reduces the image intensity by an amount that is proportional to the vertical position of the knife edge. Therefore, a beam deflection leads to an increase in intensity by an amount that is proportional to the vertical

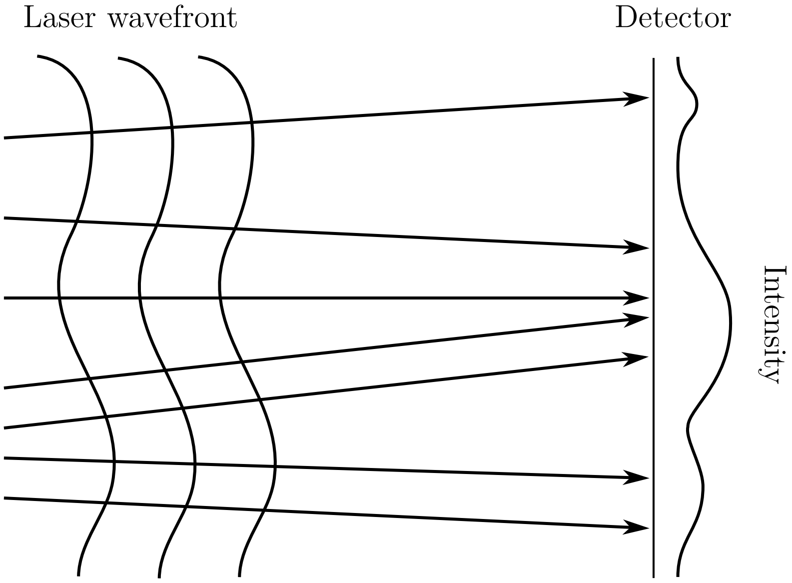

Figure 3.2: In shadowgraph imaging, the light rays of a laser wavefront perturbed by an inhomogenous plasma point at different angles from each other. This produces an intensity pattern proportional to the second derivative of the plasma refractive index.

displacement of the deflected beam above the knife edge: $I \propto \Delta x$ (valid for small displacements). Again, from Figure 3.1, one sees that this displacement is

$$\Delta x \approx (s_2 - f)\beta. \tag{3.28}$$

Combining equations (3.26), (3.27), and (3.28), I find that the vertical displacement is given by $\Delta x \approx f\theta$, and thus I obtain the result that in schlieren imaging the image intensity is proportional to the angle of deflection

$$I \propto f\theta.$$

In shadowgraph imaging, or shadowgraphy, the deflection of the rays in the plasma causes a shift on the detector in the direction of the deflection of

$$y' = y + L\theta = y + L\int\left(\frac{e^2\lambda^2}{8\pi^2\epsilon_0 m_e}\frac{\partial n_e}{\partial y}\right)dz. \tag{3.29}$$

The integrated intensity I_1 of a beam without a plasma present, integrated along the direction of the deflection angle is $\int I dy$. The corresponding integrated intensity on a screen in the presence of a plasma is $\int I' dy'$. Assuming a homogeneous background illumination, and no absorption or emission by the plasma itself, these quantities must be equal and as a result:

$$\int I' dy' = \int I dy \tag{3.30}$$

$$I' dy' = I dy \tag{3.31}$$

$$\frac{I'}{I} = \frac{dy'}{dy} = 1 + \frac{d}{dy} L \int \left(\frac{e^2 \lambda^2}{8\pi^2 \epsilon_0 m_e} \frac{\partial n_e}{\partial y} \right) dz \tag{3.32}$$

$$\frac{\Delta I'}{I} = L \int \left(\frac{e^2 \lambda^2}{8\pi^2 \epsilon_0 m_e} \frac{d^2 n_e}{dy^2} \right) dz. \tag{3.33}$$

From this derivation, one sees that shadowgraph imaging is proportional to the second spatial derivative of the plasma density [62].

While both schlieren and shadowgraph imaging could in principle be used to measure plasma density quantitatively, as the intensity in the image plane is proportional to either the first or second derivative of the plasma density, they are less accurate than other methods. The intensity is affected by noise and shot-to-shot variations, which makes it difficult to measure low-density plasmas.

3.4 Quantitative methods

3.4.1 Wavefront sensors

Using a Shack-Hartmann sensor it is possible to directly measure the wavefront curvature, which is caused by deflection through the plasma. The principle was first developed by Johannes Hartmann in the early 20th century where a mask of regularly spaced holes were used to align astronomical telescopes. In a Shack-Hartmann sensor,

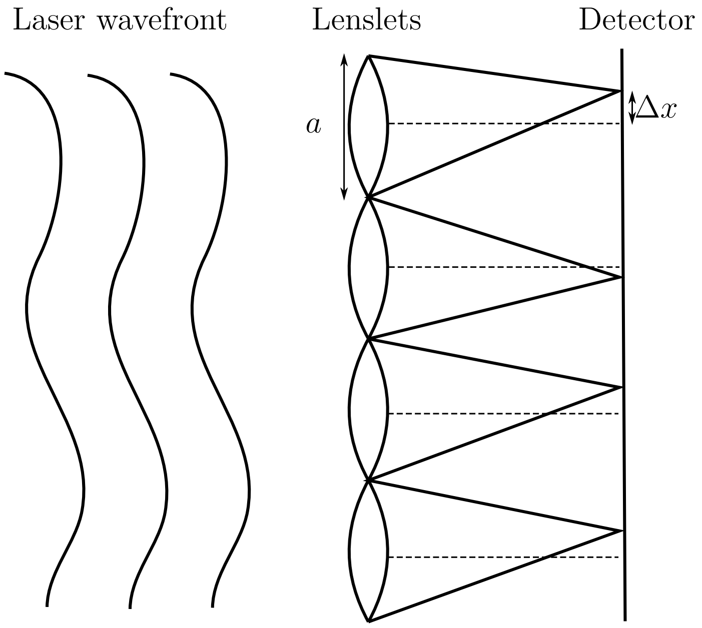

Figure 3.3: Drawing of a Shack-Hartmann wavefront sensors, showing how local perturbations in a laser wavefront leads to changes in the focal positions of an array of lenslets on a detector.

the holes are replaced by lenslets, and local deviations in the wavefront causes the focal spot of each lens to be shifted by an amount that is proportional to the gradient of the phase. The principle of this technique is shown in Figure 3.3. The distance the focal spot is displaced, Δx, is approximately:

$$\Delta x \approx f\theta.$$

The angle θ of the wavefront is related to the gradient of the phase by:

$$\theta = \nabla\phi\frac{\lambda}{2\pi},$$

where λ is the laser wavelength. Thereforet:

$$\Delta x = \nabla\phi f\frac{\lambda}{2\pi}.$$

After each small lens in the array of lenses is a corresponding sensor which measures the displacement Δx and relates it to the local gradient in the wavefront $\nabla\phi$, as outlined in the equation above. Assuming that the smallest deflection the detector can measure is Δh, the smallest measurable angle is $\theta_{\min} = \Delta h/f$. For a typical sensor, assuming that the detection limit is the pixel size, $\Delta h \approx 5\,\mu\mathrm{m}$ and $f \approx 10\,\mathrm{mm}$. Therefore $\theta_{\min} \approx 0.5$ mrad. The spatial resolution is limited by the aperture a of the lenses, approximately $150\,\mu\mathrm{m}$. Using a telescope to magnify the beam by a factor M smaller features can be resolved. However, this comes at the cost of a corresponding M times decrease in the phase sensitivity due to the decrease in the phase gradient.

3.4.2 Group velocity technique

The group velocity v_g of a laser pulse propagating through a medium is dependent on the density of the medium, and this is used to measure the on-axis density in the case of propagation through a plasma channel [64–66]. Using $\beta_g = v_g/c$, it can be shown that the on-axis group velocity is given by:

$$\beta_g = 1 - \frac{4\pi r_e n_0}{2k_0^2},$$

where r_e is the classical electron radius, n_0 the on-axis density, and $k_0 = 2\pi/\lambda$ is the laser wavenumber. A higher density leads to a lower group velocity, which leads to a later arrival time of a laser probe pulse propagating through a plasma channel compared to vacuum. This can be exploited by measuring the relative arrival time between the probe and reference pulses:

$$\Delta t = \frac{L}{\beta_g c} - \frac{L}{c},$$

where L is the length of the channel. In practice, Δt can be measured by interfering the probe-reference pulse pairs on a spectrometer, producing spectral fringes. These can be Fourier transformed to yield the temporal delay Δt, which can be used to calculate the on-axis density n_0 through the equations given above.

3.4.3 Two-colour spectral interferometry

This method is a further development of the group velocity technique described above, and uses two pulses of frequencies ω and 2ω in order to simultaneously measure the group and phase delays with a common-path interferometer [67]. The key advantages of this method is the decreased sensitivity to noise due to the shared optical elements, and the ability to measure plasma objects with large density gradients. A schematic drawing is shown in Figure 3.4. A single broadband laser pulse, for example of central wavelength 800 nm is incident on a BBO type I second-harmonic crystal and a fraction of this pulse is frequency doubled to 400 nm. The two pulses are temporally separated by passing through a glass plate before propagating through the plasma. Being of different wavelengths, the pulses suffer different group and phase delays, which are measured separately. Finally, both pulses pass through a second BBO type I second harmonic crystal and are incident on an imaging spectrometer. The (normalised) intensity $\mathrm{I}(\omega)/\mathrm{I}_{\mathrm{env}}$ (with $\mathrm{I}_{\mathrm{env}}$ the spectral intensity of each pulse measured separately), measured at the image plane of the spectrometer is:

$$\mathrm{I}(\omega)/\mathrm{I}_{\mathrm{env}}(\omega) = 2 + 2\cos\left[\phi_{\mathrm{mat}} + \omega_0 \Delta z_{\phi} + \frac{1}{c}(\omega - \omega_0)\Big(L_{\mathrm{mat}} - \Delta z_{\mathrm{gr}}\Big)\right], \tag{3.34}$$

where ϕ_{mat} and L_{mat} are constants due to the difference in optical path length through the glass and BBO crystals of the different colours and can be measured with no plasma present. The expressions for the phase delay Δz_{ϕ} and group delay Δz_{gr} are given by:

$$\Delta z_{\phi} = \frac{3}{2}\frac{\omega_p^2}{\omega_0^2} L_{\mathrm{plasma}} \tag{3.35}$$

$$\Delta z_{\mathrm{gr}} = -\frac{3}{2}\frac{\omega_p^2}{\omega_0^2} \mathrm{L}_{\mathrm{plasma}} \,. \tag{3.36}$$

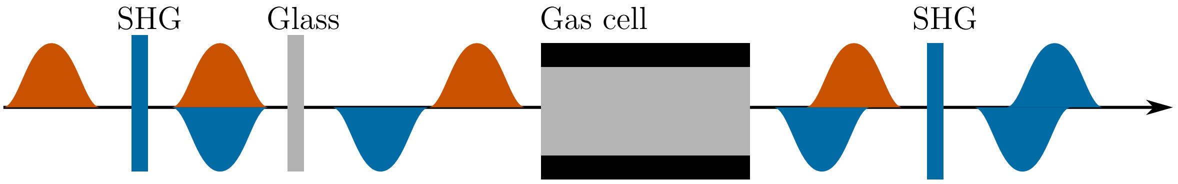

Figure 3.4: Schematic layout of two-colour spectral interferometry. In this example, an 800 nm pulse incident on an SHG generates a pulse with wavelength 400 nm. The two pulses are separated temporally by propagating through a glass block before entering the gas cell. Finally, a second SHG crystal generates another blue pulse (any remaining 800 nm light are removed with a dichroic mirror and filters) and the two are interfered on an imaging spectrometer.

The group delay can be measured by locating the sideband in the amplitude of the Fourier transform of the captured interferogram, while the phase delay is measured by fitting Equation (3.34) to the interferogram. The two quantities differ in sensitivity with the group delay being less sensitive to changes in the refractive index than the phase delay. The lower sensitivity of the group delay can therefore be used to guide the unwrapping of the phase measured by the phase delay, as this would otherwise be limited to one multiple of 2π.

3.4.4 Interferometry

Interferometry is one of the most commonly used methods to measure the plasma density due to its relatively easy setup. I will be focusing on folded wave interferometry, but the principles are very similar for different designs.

When two coherent beams with wavelength λ overlap at an angle θ on a screen, they generate spatial fringes. This is shown in Figure 3.5. Suppose that the two beams have equal phase $\phi_1 = \phi_2$ up to a multiple of 2π at some point x_0. At that point there is constructive interference and a bright fringe appears on the screen. At another point $x_1 = x_0 + \lambda/\sin\theta$, the phase difference is again a multiple of 2π. Between x_0 and x_1, where $\phi_1 - \phi_2 = \pi$ there is destructive interference and a dark fringe appears on the

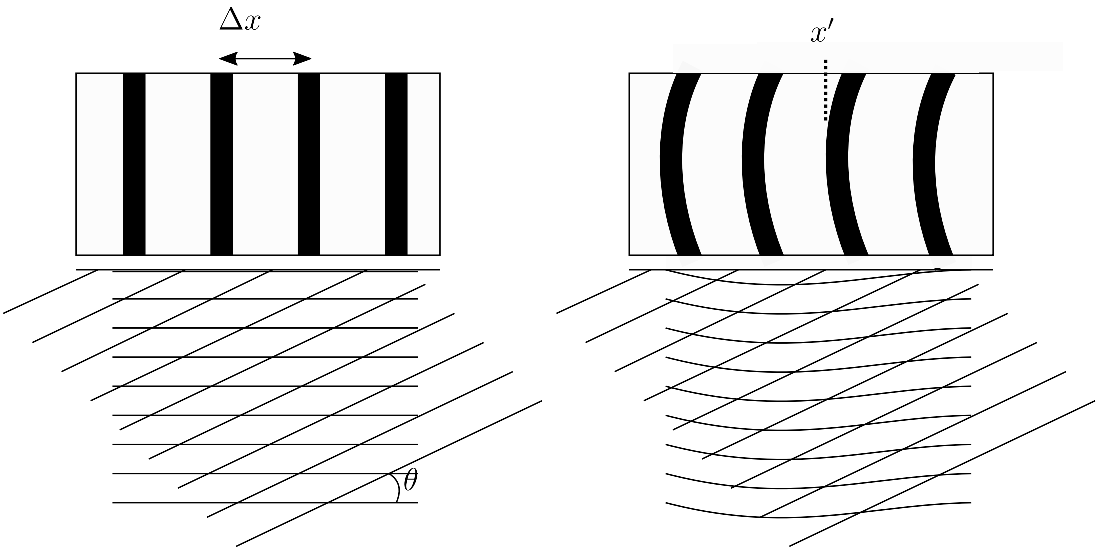

Figure 3.5: Left: illustration of interference between two lasers with a crossing angle θ. Bright and dark fringes with a fringe separation Δx appear on the screen. Right: a phase shift $\Delta\phi$ in one of the beams causes the fringes on the screen to shift by a distance x'.

screen. One therefore obtains a fringe pattern, with fringes separated by

$$\Delta x = \frac{\lambda}{\sin\theta}. \tag{3.37}$$

Assuming instead that one of the beams has an additional phase shift $\Delta\phi$, the fringes are locally displaced by a distance x':

$$x' = \frac{\Delta\phi}{2\pi}\frac{\lambda}{\sin\theta}. \tag{3.38}$$

Dividing by the fringe separation I obtain an expression for the phase shift:

$$\frac{x'}{\Delta x} = \frac{\Delta\phi}{2\pi}, \tag{3.39}$$

which means that relative fringe offset provides a measurement of the phase shift, and that this measurement is independent of the wavelength and angle of incidence θ.

3.4.4.1 Mach-Zehnder interferometer

A versatile design for an interferometer that is frequently used in plasma experiments is the folded wavefront Mach-Zehnder interferometer (Figure 3.6). A single probe beam propagates through the plasma either transversally or longitudinally and suffers a phase shift $\Delta\phi$, given by equation (3.23), relative to propagation through vacuum. The probe beam diameter is chosen to be much larger than the plasma, so that a large part propagates through low-density neutral gas, which has a refractive index n_g close to that of vacuum. By interfering the part of the beam which propagated through plasma with a different part of the beam, an interference pattern is generated and used to measure the phase shift $\Delta\phi$. As was shown in equation (3.37), the fringe spacing is determined by the angle between the two incident beams. The specific design of the Mach-Zehnder shown in Figure 3.6 allows independent control of the angle, as well as the position the two overlapping beams. This setup is required when the plasma is oriented horizontally, as the interferogram fringes need to be oriented perpendicular to the plasma.

When used to probe plasma channels I differentiate between the cases of the probe propagating parallel to the longest dimension of the plasma (longitudinal interferometry) and perpendicular to it (transverse interferometry). An advantage of longitudinal interferometry is that the phase shift is relatively large, which makes it easy to measure. However, this also means that refraction interferometry is only useful up to a length where the phase is less than $\sim 2\pi$ (a larger phase difference than this over a short length causes the interferometry fringes to disconnect which makes analysis difficult). For this reason transverse interferometry should be used for longer plasma columns. The drawbacks of this are that the integrated phase shift is relatively small ($\sim 100\,\mathrm{mrad}$ for a density $n_0 \sim 10^{18}\,\mathrm{cm}^{-3}$), and that the phase needs to be inverted in order to recreate the 3-dimensional phase object from a 2-dimensional projection. This is usually done assuming that the phase object is azimuthally symmetric, and this analysis method is

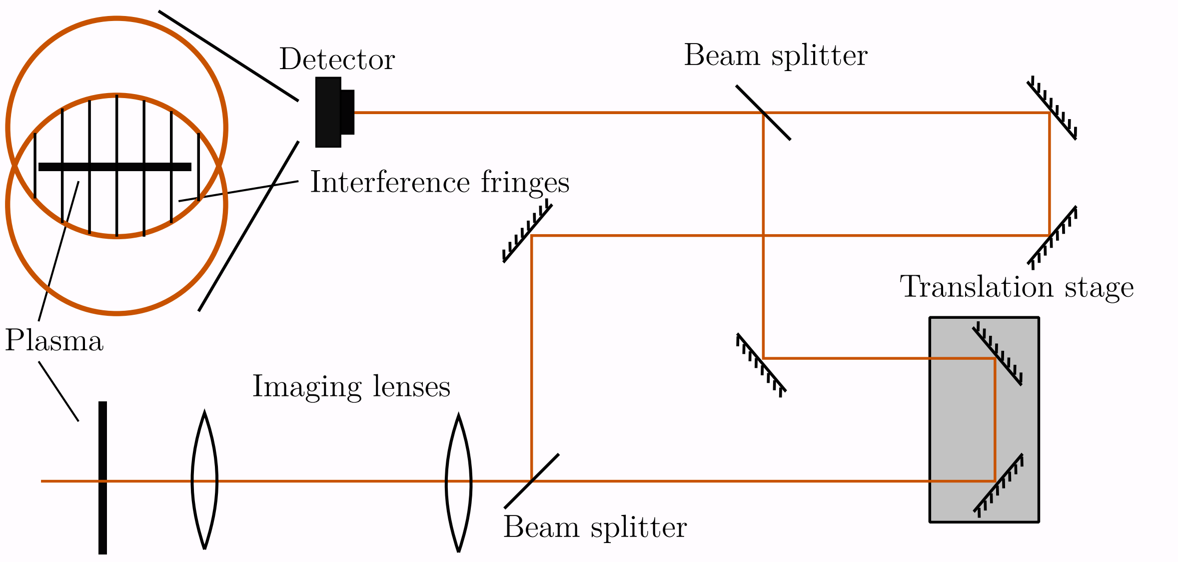

Figure 3.6: Schematic layout of a Mach-Zehnder interferometer for measuring plasma densities. The plasma is imaged by two lenses onto a detector. A pair of beam splitters are used to set up and combine two arms which overlap on the detector with a spatial offset and at an angle θ to generate an interference pattern. A translation stage in one of the arms is used to ensure that the path lengths are identical, in order to ensure temporal overlap.

covered in a later chapter.

3.4.4.2 Tomographic interferometry

In general, plasma columns are not fully symmetric which means that inversion techniques that assume symmetry are not accurate. A simple improvement which was designed by the author is shown in Figure 3.7. Here the probe pulse is split into two arms using a polarising beam splitter; the two orthogonally polarised beams propagate transversely through the plasma at right angles. After the plasma, two mirrors are used to capture the beams and steer them onto a common path using a 50 : 50 beam splitter (this will lead to a 50% loss of intensity in each beam). The rest of the layout is identical to the interferometer detailed in Figure 3.6, with the difference of having a polarising beam splitter located before the camera, and a second camera to capture both the reflected and the transmitted light, as shown in Figure 3.8. See Section 4.3.3 for a discussion on how this setup could be used to aid in the analysis of plasma channels.

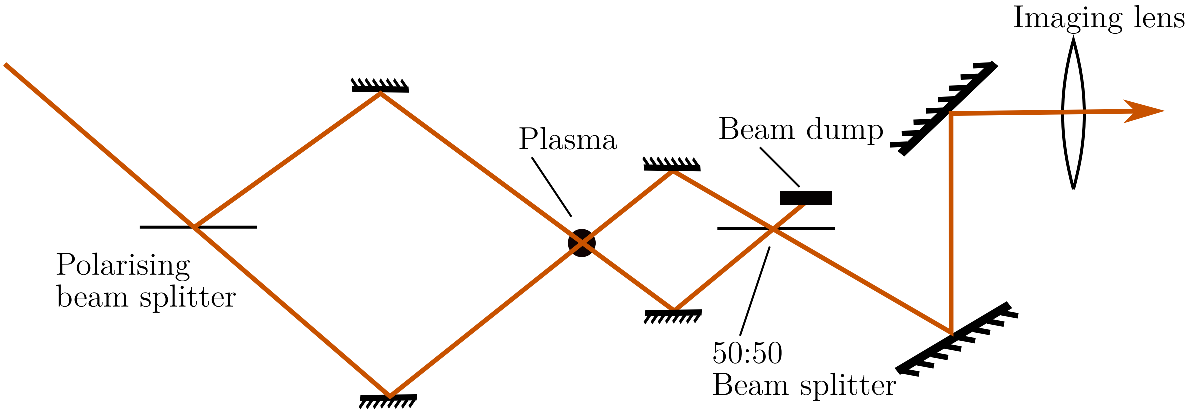

Figure 3.7: Layout of of a tomographic interferometer. Two beams with different polarisations are generated and cross the plasma at right angles, before being imaged and pass through the same Mach-Zehnder interferometer layout as shown in Figure 3.6.

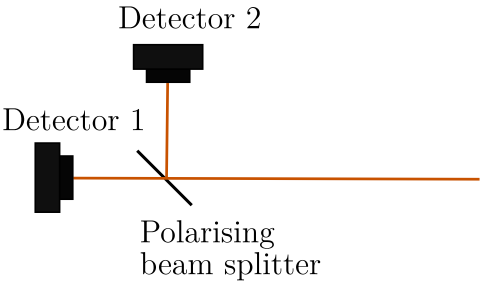

Figure 3.8: Drawing showing how a second camera could be added to the Mach-Zehnder interferometer shown in Figure 3.6 to simultaneously and independently measure two beams with different crossing angles through a plasma, from Figure 3.6.

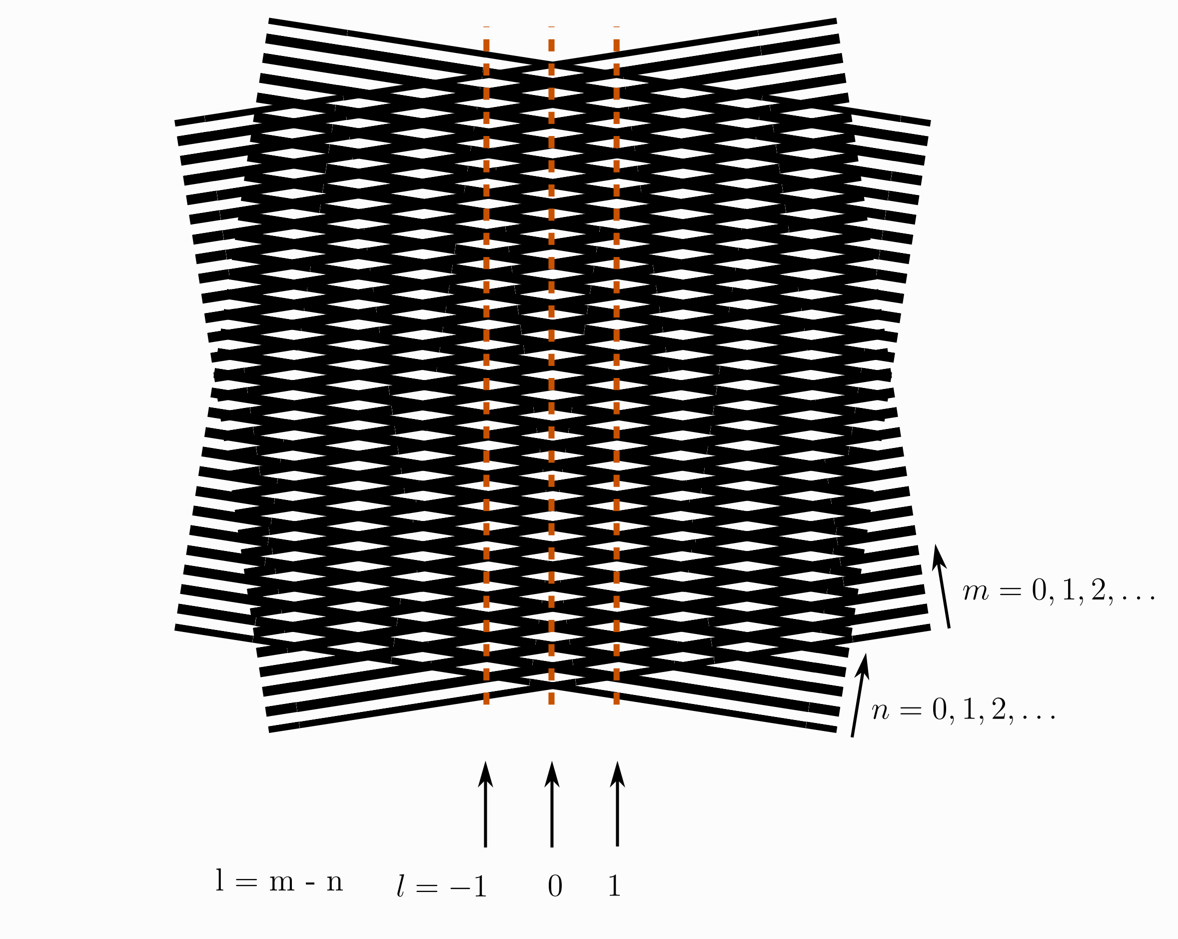

Figure 3.9: Two overlapped gratings, with the resulting bright 'fringes' marked with the red dashed lines. Each fringe can be labelled by $l = m - n$, where m and n are the indices of each line in the gratings.

3.4.5 Moiré deflectometry

In moiré deflectometry, the angular deflection rather than the acquired phase is used to measure the plasma density, which allows the angular sensitivity to be increased at the cost of spatial resolution. I will mainly follow the treatment presented in Kafri and Glatt [68].

3.4.5.1 The moiré pattern

The moiré pattern is caused by two overlapping gratings with a similar pitch (i.e. the distance between each line). Mathematically, I describe the location of the lines of one of the gratings using the coordinates x and y:

$$y = x\tan\frac{\theta}{2} + \frac{np}{\cos\frac{\theta}{2}},\ n = 0 \pm 1 \pm 2 \pm 3, ... \tag{3.40}$$

where $\theta/2$ is its angle with respect to the horizontal, p the pitch, and n the grating index. Rearranging the terms we obtain:

$$y\cos\frac{\theta}{2} = x\sin\frac{\theta}{2} + np,\ n = 0 \pm 1 \pm 2 \pm 3, ... \tag{3.41}$$

Similarly, for the second grating, we assume it to have an angle $\frac{-\theta}{2}$ with respect to the horizontal, so that the angle between the two rulings is θ. The equation for the second ruling is thus:

$$y\cos\frac{-\theta}{2} = x\sin\frac{-\theta}{2} + mp,\ m = 0 \pm 1 \pm 2 \pm 3, ... \tag{3.42}$$

$$y\cos\frac{\theta}{2} = -x\sin\frac{\theta}{2} + mp,\ m = 0 \pm 1 \pm 2 \pm 3, ... \tag{3.43}$$

The two rulings will cross and form a diamond-shape pattern, which is what will give rise to the moiré fringes. I index the line crossings by the new index $l = m - n$ and we see that by subtracting Equation (3.41) from Equation (3.43), I obtain the following equation:

$$0 = -2x\sin\frac{\theta}{2} + lp,\ l = 0 \pm 1 \pm 2 \pm 3, ... \tag{3.44}$$

$$x\sin\frac{\theta}{2} = lp,\ l = 0 \pm 1 \pm 2 \pm 3, ... \tag{3.45}$$

$$\Rightarrow x = \frac{lp}{2\sin\frac{\theta}{2}} \approx \frac{lp}{2\theta}, \tag{3.46}$$

assuming that θ is small. Equation (3.46) tells us that the line crossings, and thus the moiré fringes, are aligned horizontally and spaced by a distance of the pitch divided by the angle between the gratings. There is also a high-frequency interference pattern which is found by setting $l = m + n$, but that is less useful for applications since it is not easily detectable with a camera.

3.4.5.2 Moiré deflectometry

So far, I have assumed that the ruling patterns are on top of each other, but in order to use them for deflectometry they need to be separated by some distance $L > 0$. A schematic of a moiré deflectometer setup is shown in Figure 3.10. It turns out that this configuration leads to moiré fringes that are sensitive to the angle of the incident rays, which I will explore next. Instead of assuming that the incident optical rays are normal to the gratings, let them have some angle ϕ with respect to the normal in the y-direction. In the space between the grating pair, the rays will have travelled a distance ϕL. This changes the projection of the first grating onto the second grating, and so the two grating equations become:

$$y \cos\frac{\theta}{2} = x \sin\frac{\theta}{2} + np,\ n = 0 \pm 1 \pm 2 \pm 3, ... \tag{3.47}$$

$$[y + \phi L] \cos\frac{\theta}{2} = -x \sin\frac{\theta}{2} + mp,\ m = 0 \pm 1 \pm 2 \pm 3, ... \tag{3.48}$$

Combining these equations, using again the definition $l = m - n$, one obtains:

$$\phi L \cos\frac{\theta}{2} = -2x \sin\frac{\theta}{2} + lp,\ l = 0 \pm 1 \pm 2 \pm 3, ... \tag{3.49}$$

$$x = \frac{lp}{2\sin\frac{\theta}{2}} - \phi L \frac{\cos\frac{\theta}{2}}{2\sin\frac{\theta}{2}} \tag{3.50}$$

$$x \approx \frac{lp}{\theta} - \frac{\phi L}{\theta}, \tag{3.51}$$

Thus, a *vertical* angle of the incident beam ϕ leads to a relative *horizontal* shift in the moiré fringe pattern of $\delta x/x \approx \phi L/p$. The fact that the angle is multiplied by L/p means that the sensitivity can be increased by either increasing the distance between the gratings, or use gratings with a smaller pitch.

3.4.5.3 Talbot planes

It is important to note that the process in which moiré fringes are generated in a real deflectometer is more complicated than in the case of our everyday experiences (such as the example of overlaying two gratings in the beginning of this section). As is shown in Goodman [69], the diffracted beams from a grating interfere at fixed distances to generate Talbot images (or self-images), which are interference patterns with the same pitch as the original grating. These images appear at regular positions:

$$z = \frac{2np^2}{\lambda},$$

where n is an integer, p the pitch of the grating and λ the wavelength of the laser. In the situations that are relevant for the work presented here, typical values are $p = 5\,\mu\text{m}$ and $\lambda = 800\,\text{nm}$. I thus obtain

$$z = n\frac{2 \times 5^2}{0.8}\,\mu\text{m} = n \times 62.5\,\mu\text{m},$$

so the Talbot images appear every 62.5 µm, or 16 times per millimetre. When setting up the deflectometer, it is important to make sure to place the second grating at one of the Talbot planes.

3.4.5.4 Resolution and sensitivity

In the standard moiré deflectometry setup shown in Figure 3.10, increasing the distance inevitably leads to poorer spatial resolution, meaning that there is a trade-off between angular sensitivity and spatial resolution. This happens because rays originating from a single point before the grating are diffracted into different orders by the grating. A grating with pitch p diffracts rays with wavelength λ at an angle $\theta = \lambda/p$. A distance

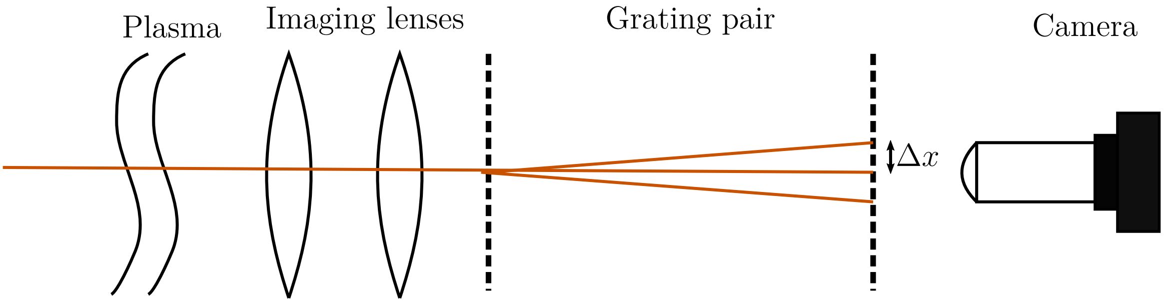

Figure 3.10: Schematic layout of a moiré deflectometer. The two lenses form separate images for each diffracted order of the plasma on the detector. The spatial offset between two orders is Δx, which also determines the spatial resolution attainable.

L away from the grating the first and zeroth diffracted orders are separated by:

$$\Delta x = \theta L = \frac{\lambda}{p} L,$$

which sets the lower of limit of the spatial resolution of the deflectometer. Note that for a broadband pulse with finite bandwidth $\Delta\lambda$ there is additional uncertainty due to the spread in wavelengths, but in practice this will be smaller by a factor of $\Delta\lambda/\lambda$ compared to the above term (this follows from the angular spread $\Delta\theta = \Delta\lambda/p$, and $\Delta\theta/\theta = \Delta\lambda/\lambda$). One can also investigate the angular sensitivity by calling h the lowest fractional fringe shift $\delta x/x$ that can be resolved by the detector: $h = \delta x/x$. This sets the lowest deflection one can measure by:

$$\phi_{\min} = h\frac{p}{L}.$$

By comparing this expression with that of the spatial resolution, one sees that the dependence on p and L are inverted. Taking the product of the sensitivity and resolution, one obtains:

$$\phi_{\min}\Delta x = h\frac{p}{L}\frac{\lambda}{p}L = h\lambda.$$

This relation shows that in the standard moiré deflectometry setup, the product of the resolution and sensitivity is limited by the resolution of the detector and the wavelength of the probe light. For example, increasing the pitch of the gratings used may increase the spatial resolution, but decreases the angular sensitivity. Another way to see this is to consider moiré deflectometry as a form of shearing interferometry [68, 70, 71]. Here, two identical beams are offset in a direction transverse to the propagation direction. Both beams have a phase imprint $\phi(x, y)$ caused by propagation through a plasma structure, and assuming plane waves and neglecting time dependence they are described by:

$$E_1(x, y, z) = E_0 \exp\left(-2\pi i \phi(x, y)\right) \tag{3.52}$$

$$E_2(x, y, z) = E_0 \exp\left(-2\pi i \phi(x + \delta x, y)\right), \tag{3.53}$$

where E_0 is the electric field amplitude and δx is the transverse offset between the beams. The intensity distribution of the overlap of the two beams is:

$$\begin{aligned} I(x, y, z) &= \left|E_1(x, y, z) + E_2(x, y, z)\right|^2 \\ &= 2E_0^2 \left|\exp\left(-2\pi i \phi(x, y)\lambda\right) + \exp\left(-2\pi i z \phi(x + \delta x, y)\right)\right|^2 \\ &= 2E_0^2 \Big(1 + \cos 2\pi \left[\phi(x + \delta x, y) - \phi(x, y)\right]\Big). \end{aligned} \tag{3.54}$$

The term in the cos-function looks similar to a derivative, and one can replace it with (for small offsets):

$$\phi(x + \delta x, y) - \phi(x, y) \approx \frac{\partial \phi(x, y)}{\partial x} \delta x. \tag{3.55}$$

It therefore follows that:

$$I(x, y, z) = 2E_0^2 \left(1 + \cos 2\pi \delta x \left[\frac{\partial \phi(x, y)}{\partial x}\right]\right). \tag{3.56}$$

In a moiré deflectometer, the separation δx is caused by the diffraction angle, and thus the pitch of the grating, and the separation between the gratings. We focus only on the zeroth and first orders, since these contain most of the intensity. The link to

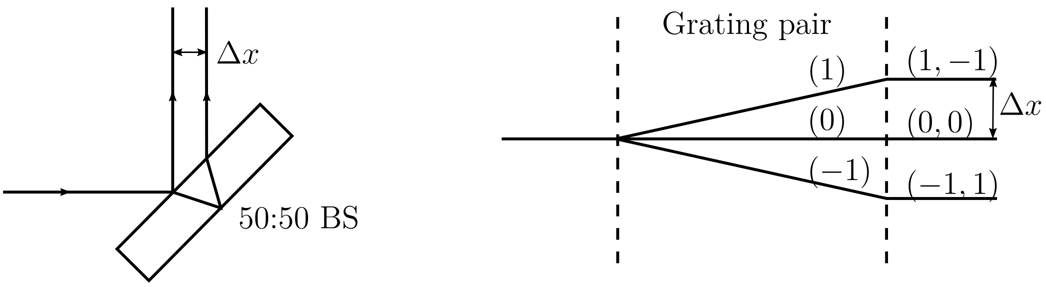

Figure 3.11: Left: drawing of a simple shearing interferometer, commonly used to measure wavefront collimation. Right: diffracted orders in a moiré deflectometer. The first three diffracted orders $(-1, 0, 1)$ of the first grating produce three beams parallel to the zeroth order after the second grating. As an example, the beam diffracted into order (1) by the first grating and -1 by the second grating will be parallel to the beam diffracted into order (0) by both gratings. The other diffracted orders are not shown.

the shearing interferometer can be seen by considering that after the second grating, the first orders are diffracted to parallel with the zeroth order, separated by δx. A comparison between a shearing interferometer and a moiré deflectometer is shown in Figure 3.11. I write:

$$\delta x = \frac{\lambda L}{p}. \tag{3.57}$$

Finally, obtaining:

$$I(x, y, z) = 2E_0^2 \left(1 + \cos 2\pi \frac{\lambda L}{p} \left[\frac{\partial \phi(x, y)}{\partial x} \right] \right). \tag{3.58}$$

This also shows the inherent trade-off between $\partial \phi(x, y)/\partial x$ and δx — increasing L/p increases the sensitivity to angular deflections, but decreases the ability to localise the source of the deflection. Note that approximating $\phi(x + \delta x, y) - \phi(x, y)$ as the differential $(\partial \phi(x, y)/\partial x)\delta x$ is only valid as long as δx is small compared to the length scale of $\phi(x)$. It has been suggested that the trade-off between resolution and sensitivity is not fundamental but can be overcome [72]. The idea behind this concept is that by separating the different orders by a strongly diffracting gratings, blocking the zeroth order, and recombining the first orders at the diffraction angle θ the angular sensitivity can be increased arbitrarily without negatively impacting the spatial resolution. However, this is does not work, since as seen from Figure 3.11, the spatial separation of different orders is necessary in order to measure the gradient of the wavefront.

Chapter 4

Interferogram analysis

After having obtained an interferogram from either an interferometer or a deflectometer, as shown in the previous chapter, I now turn to the problem of how to analyse the interferogram in order to extract the phase shift. The subject of how this is done is an entire field in its own right, and a number of steps need to be taken, each of which will be covered in this chapter. First, the phase shift (determined up to modulo 2π) is extracted from measuring the fringe deformation. Second, the obtained phase is unwrapped, where phase discontinuities in the phase caused by the uncertainty in the absolute phase value are removed. When the measured phase is the transverse projection of the object, an additional step of inverting the phase is required.

4.1 Phase extraction

4.1.1 Fringe tracing

The simplest method of obtaining the phase shift from an interferogram is by tracing each fringe along its axis. The phase is then be obtained by dividing the horizontal deformation x' from the original fringe position by the fringe spacing Δx, as I showed in section 3.4.4:

$$\Delta\phi = 2\pi \frac{x'}{\Delta x}. \tag{4.1}$$

While the fringe tracing method is now outdated and has been replaced by more computationally efficient and sensitive methods that I will discuss below, it is still a very robust method and serves as a simple illustration of phase retrieval. In Figure 4.1a I show a simulated phase map, and the corresponding interferogram in Figure 4.1b. I show how its fringes are traced along the ridge of each fringe in Figure 4.2a. Figure 4.2b shows the resulting extracted phase using equation (4.1). A clear shortcoming of the fringe tracing method is immediately visible from these simulated results: the phase data is only collected from one line per fringe, while any data between the fringes is unused. This leads both to a reduction in the spatial resolution and in the phase resolution.

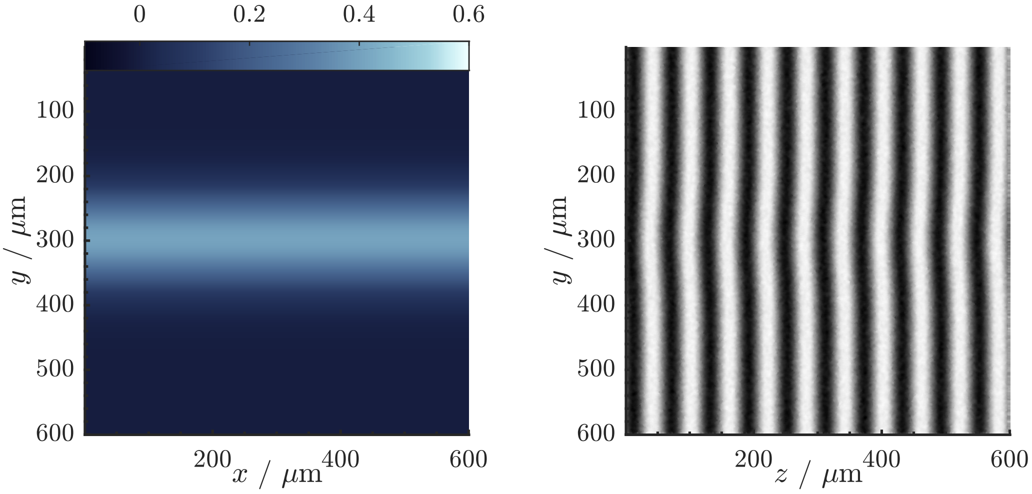

(a) (b)

Figure 4.1: (a) Simulated phase map, in radians, and (b) corresponding interferogram. Gaussian noise with mean 0, peak amplitude 0.1 and variance 1 was added to interferogram.

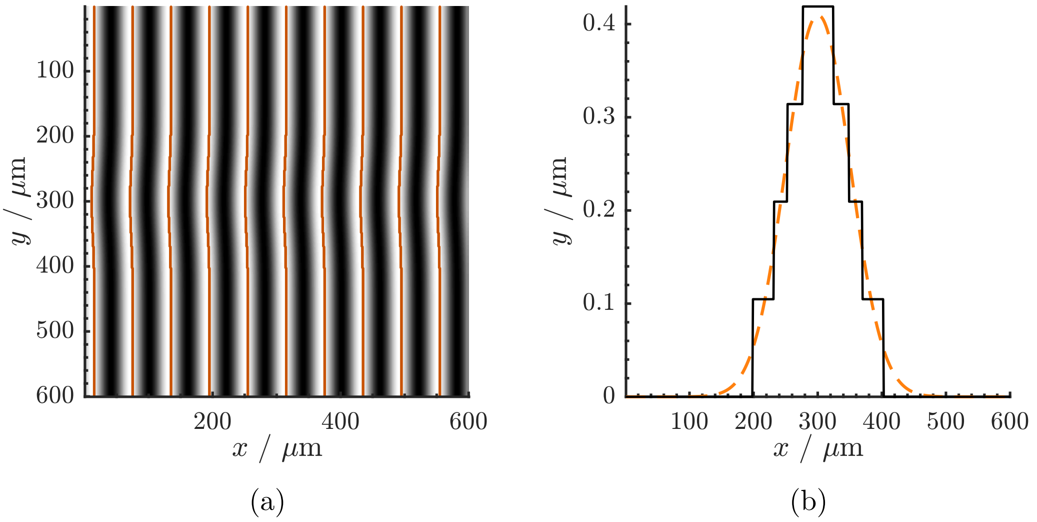

Figure 4.2: Illustration of the fringe tracing method: (a) shows the trace of each fringe, and (b) the extracted phase using equation (4.1), averaged along the x-axis (black solid line), compared with the original averaged phase (red dashed line).

4.1.2 Fourier transform method

A very fast method for obtaining the phase from an interferogram was first reported by Takeda et al. [73], based on the use of the Fourier transform (FT). Whereas in the fringe tracing method only one line was used to represent each fringe, here all pixels in the image are used. Assuming that the pixel intensity in the interferogram $I(x, y)$ has the following general form:

$$I(x, y) = a(x, y) + b(x, y) \cos\left[2\pi f_0 x + \Delta\phi(x, y)\right], \tag{4.2}$$

where a and b are slowly varying compared to the intensity of the fringes f_0. I rewrite this as:

$$I(x, y) = a(x, y) + c(x, y) \exp\left(2\pi i f_0 x\right) + c^*(x, y) \exp\left(-2\pi i f_0 x\right), \tag{4.3}$$

where $c(x, y)$ is defined as:

$$c(x, y) = (1/2) b(x, y) \exp[i\phi(x, y)]. \tag{4.4}$$

The Fourier transform of equation (4.3) is given by:

$$\tilde{I}(\mathrm{f},\mathrm{y}) = A(f,y) + C\left(f - f_0, y\right) + C^*\left(f + f_0, y\right), \tag{4.5}$$

where A and C is the Fourier transforms of a and c, respectively. An illustration of the magnitude of equation (4.5) is shown in Figure 4.3. Since C and A are well separated in the frequency domain, I apply a filter around $C(f - f_0, y)$, shift f by f_0, and perform an inverse Fourier transform to obtain $c(x, y)$. It is then straightforward to obtain the phase shift $\Delta\phi(x, y)$ by taking the logarithm of equation (4.4):

$$\log[c(x,y)] = \log[(1/2)b(x,y)] + i\Delta\phi(x,y). \tag{4.6}$$

The phase shift is thus obtained from:

$$\Delta\phi(x,y) = \Im(\log[c(x,y)]). \tag{4.7}$$

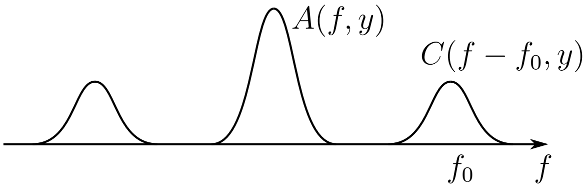

Figure 4.3: Illustration of the magnitude of a Fourier transform of an interference pattern (after [73]).

4.1.3 Continuous wavelet transform method

An alternative approach to performing Fourier analysis to extract the phase from an interferogram is the use of continuous wavelet transform (CWT) [74]. Instead of using infinite-length sinus and cosinus functions as basis functions to represent a function, we use a finite-length basis function, for example the Morlet wavelet:

$$\varphi(x) = g(x)\exp(i\eta x), \tag{4.8}$$

where $g(x)$ is a window function, here the Gaussian function $g(x) = \exp(-x^2/\tau)$; τ and η are fixed parameters that determine the spectral and temporal resolution of the wavelet. The advantage of the CWT compared to the Fourier transform is that it can be used to analyse functions with frequency components that vary in time or space. This is possible since it uses basis functions with a finite, rather than infinite, length. To show how to obtain the phase using the CWT method, I calculate the wavelet coefficients of the interferogram profile, following Mallat [75]:

$$f(x) = a(x)\cos\left[\theta(x)\right], \tag{4.9}$$

where $a(x)$ is the amplitude, $\theta(x) = kx + \phi$, k the spatial frequency of the fringes and ϕ the phase shift. The wavelet coefficients of $f(x)$ are given by:

$$Wf(u,s) = \int_{-\infty}^{+\infty} f(x)\varphi_{s,u}(x)dx. \tag{4.10}$$

Here, $\varphi_{s,u}(x)$ are 'daughter' wavelets generated from the 'mother' wavelet in Equation (4.8). These are generated by introducing a scale parameter s, where s^{-1} is a measure of the instantaneous frequency, and a translation parameter u indicating position, in the mother wavelet:

$$\begin{align} \varphi_{s,u}(x) &= \frac{1}{\sqrt{s}} g\left(\frac{x-u}{s}\right)\exp\left(i\eta\frac{x-u}{s}\right) \tag{4.11}\\ &= g_{s,u,\xi}(x)\exp(-i\xi u) \tag{4.12}\\ g_{s,u,\xi}(x) &= \frac{1}{\sqrt{s}} g\left(\frac{x-u}{s}\right)\exp(-i\xi x), \tag{4.13} \end{align}$$

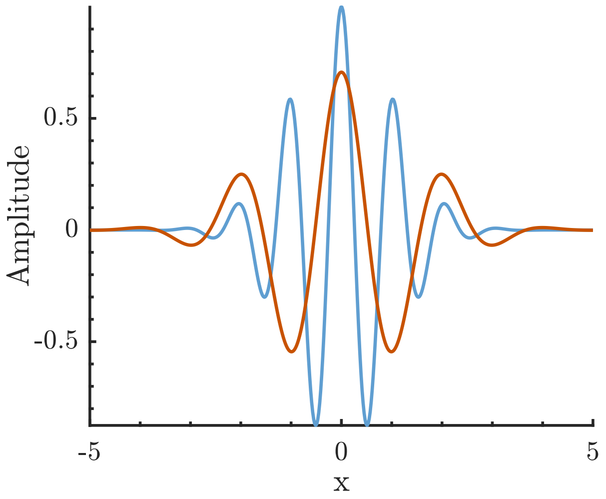

Figure 4.4: Illustration of the Morlet wavelet for the parameters $\tau = 2$, $\eta = 6$ at two different scales $s = 1$ (blue) and $s = 2$ (red).

with $\xi = \eta/s$, and I introduced the scaled and translated window function $g_{s,u,\xi}(x)$. Figure 4.4 shows a plot of two daughter wavelets at the same offset $u = 0$ with two different scale parameters $s = 1$ and $s = 2$. In Appendix A I show that the wavelet coefficients are:

$$Wf(u,s) = \frac{\sqrt{s}}{2} a(u) \exp[i\theta(u)] \hat{g}\left(s\left[\xi - \theta'(u)\right]\right), \tag{4.14}$$

where $\hat{g}(\omega)$ is the Fourier transform of the window function $g(x)$:

$$\hat{g}\left(s\left[\xi - \theta'(u)\right]\right) = \int_{-\infty}^{+\infty} g\left(t'\right) \exp\left(-ist'\left(\xi - \theta'(u)\right)\right) dt'. \tag{4.15}$$

In general, any real interferogram will contain noise with many different frequency components. In order to isolate the signal from the noise, I look for the strongest frequency component of interferogram which should correspond to the fringe frequency. In order to localise this, I calculate the normalised scalogram:

$$\frac{|Wf(u,s)|^2}{s} = \frac{1}{4} a^2(u) \left|\hat{g}\left(s\left[\xi - \theta'(u)\right]\right)\right|^2, \tag{4.16}$$

which is maximum at the frequency of the fringes: $\xi = \eta/s = \theta' = \omega$. The set of scales $s_R(u)$ for each position u for which equation 4.16 is maximum is known as the ridge. This is shown in Figure 4.5 using a simulated 1D interference pattern. One can therefore use the scales $s_R(u)$ at each ridge position to extract the phase directly from the wavelet coefficients in equation 4.14, for example using:

$$\theta(u) = \Im\{\log[Wf(u, s_R)]\}. \tag{4.17}$$

The phase shift ϕ is obtained by subtracting a reference phase $\theta_{\text{ref}}(u)$, from an interferogram with no phase shift, from the phase from an interferogram with an encoded phase shift $\theta_{\text{data}}(u)$:

$$\phi(u) = \theta_{\text{data}}(u) - \theta_{\text{ref}}(u). \tag{4.18}$$

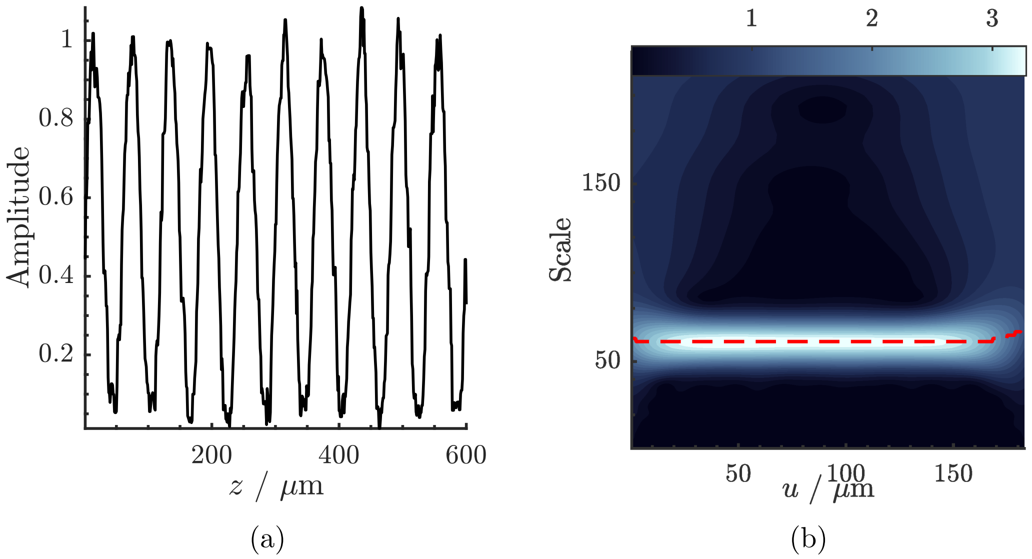

(a) (b)

Figure 4.5: Illustration of the CWT analysis: (a) single row lineout along the x-axis of the simulated interferogram in Figure 4.1b (b) corresponding intensity of the CWT coefficients of the lineout, using equation (4.16) with wavelet parameters $\tau = 2$ and $\eta = 6$. The scale ridge of $s \approx 60$, corresponds to a spatial frequency $\eta/2\pi s \approx 0.016$, which is approximately equal to the simulated fringe frequency 1/60.

4.1.4 Comparing the Fourier transform with the continuous wavelet transform

To compare the FT method with the CWT method I used both techniques on the same simulated interferogram, shown in Figure 4.1. I then obtained the phase maps shown in Figure 4.6. As can be seen, the CWT method does not perform well near the edges of the phase map, so I made cuts in order to remove these artefacts. I then compared the phase in the central square with the corresponding original phase from Figure 4.1, and calculated the standard deviation σ of the discrepancy between the acquired $\phi_1(z, y)$ and the original phase $\phi_0(z, y)$:

$$\sigma = \sqrt{\frac{1}{N}\sum_{i,j}[\phi_1(i,j) - \phi_0(i,j) - \mu]} \tag{4.19}$$

$$\mu = \frac{1}{N}\sum_{i,j}[\phi_1(i,j) - \phi_0(i,j)]. \tag{4.20}$$

I found that the CWT method performed slightly better than the FT method, with $\sigma_{FT} \approx 0.015$, $\sigma_{CWT} \approx 0.013$ ($\sigma_{FT}/\sigma_{CWT} \approx 1.1$), which could be compared to the amplitude of the simulated phase map: $\max(\phi^{sim}(x, y)) = 0.4094$.

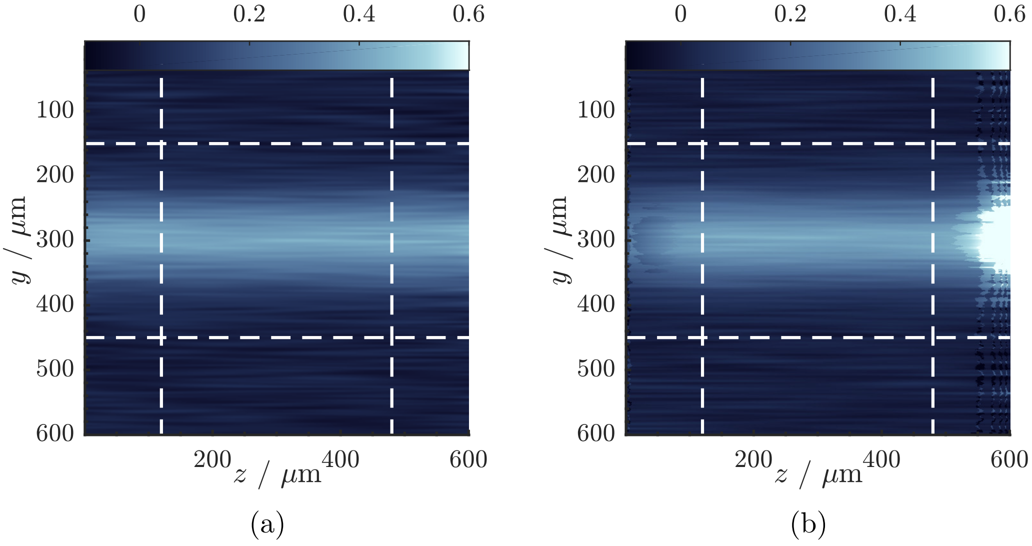

(a)

(b)

Figure 4.6: Comparing the obtained phase using (a) the Fourier transform method and (b) the continuous wavelet transform method. The central square shows the region used to compare the accuracy of the two methods.

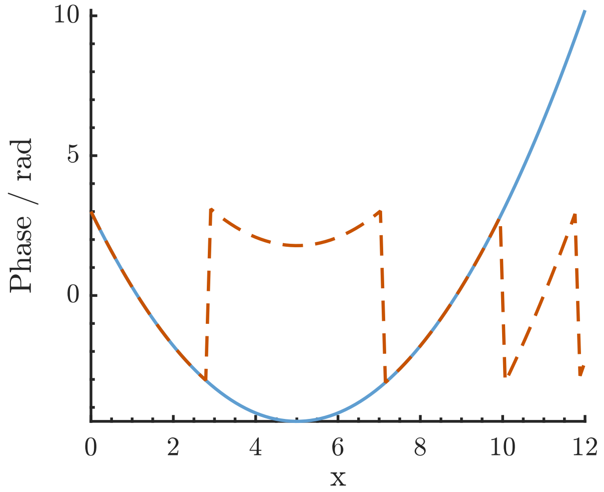

Figure 4.7: Wrapped phase (red striped line) compared to the original phase (blue solid line). The original phase can be recovered by adding a factor 2π to the wrapped phase after each discontinuity.

4.2 Phase unwrapping

After having obtained the phase ϕ through either the methods described above, we need to 'unwrap' the phase. This is because ϕ can only be determined up to modulo 2π: this is illustrated in Figure 4.7. In one dimension, this shows up as a saw-tooth shape. In this example, it is simple to recover ϕ, assuming that the real phase is slowly varying: simply add 2π at each discontinuity in the phase. However, in two dimensions the problem becomes much more difficult since there is not necessarily a unique way to unwrap the phase. To get around this problem, a number of algorithms have been devised.

4.2.1 The Itoh condition

The Itoh condition [76] is an assumption that the signal is sufficiently sampled so that the difference in phase between two points is less than 2π, or

$$\Delta\phi(n) \equiv \phi(n) - \phi(n-1), \quad -\pi < \Delta\phi(n) \leq \pi. \tag{4.21}$$

If this condition holds, the phase may be uniquely unwrapped using the following method. Define the wrapping operator W:

$$\mathrm{W}\phi = \phi - 2\pi k, \tag{4.22}$$

where k is an integer that ensures $-\pi < \mathrm{W}\phi \leq \pi$. The wrapping operator W has the following property:

$$\mathrm{W}\Delta\mathrm{W}\phi = \Delta\phi, \tag{4.23}$$

where

$$\begin{aligned}
\Delta\mathrm{W}\phi &= \mathrm{W}\phi(n) - \mathrm{W}\phi(n-1) & (4.24)\\
&= \phi(n) - 2\pi k_n - \phi(n-1) - 2\pi k_{n-1} & (4.25)\\
&= \Delta\phi(n) - 2\pi(k_n - k_{n-1}). & (4.26)
\end{aligned}$$

I evaluate $\mathrm{W}\Delta\mathrm{W}\phi$ as

$$\begin{aligned}
\mathrm{W}\Delta\mathrm{W}\phi &= \mathrm{W}[\Delta\phi(n) - 2\pi(k_n - k_{n-1})] & (4.27)\\
&= \Delta\phi(n) - 2\pi(k_n - k_{n-1}) - 2\pi k. & (4.28)
\end{aligned}$$

On the left hand side, one has by definition $-\pi < \mathrm{W}\phi \leq \pi$, and on the right hand side we have $\Delta\phi(n)$ which we assumed be in the range $-\pi < \Delta\phi(n) \leq \pi$. Since the k_i are integers, this means that the left hand side of the above expression can not equal the right hand side unless:

$$-2\pi(k_n - k_{n-1}) - 2\pi k = 0. \tag{4.29}$$

It therefore follows that $\mathrm{W}\Delta\mathrm{W}\phi = \Delta\phi$, and for a given sequence of points $\phi_m, \phi_{m-1} \ldots \phi_0$ I can calculate the sum of differences along the path as

$$\sum_{n=1}^{m} \Delta\phi(n) = \sum_{n=1}^{m} \mathrm{W}\Delta\mathrm{W}\phi(n). \tag{4.30}$$

I can expand the sum above using:

$$\sum_{n=1}^{m} \Delta\phi(n) = (\phi_m - \phi_{m-1}) + (\phi_{m-1} - \phi_{m-2}) + \cdots + (\phi_1 - \phi_0) = \phi_m - \phi_0. \tag{4.31}$$

Finally, I obtain by rearranging:

$$\phi_m = \phi_0 + \sum_{n=1}^{m} \mathrm{W}\Delta\mathrm{W}\phi, \tag{4.32}$$

which is the Itoh unwrapping method: assuming an initially correct phase in the point ϕ_0, I then calculate the correct phase in the point ϕ_m by integrating along a path that connects ϕ_m and ϕ_n.

4.2.1.1 Example unwrapping

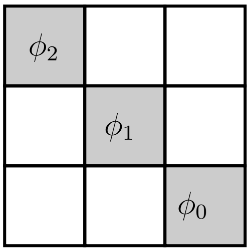

Figure 4.8: Sequence of three phase values to be unwrapped.

Consider the sequence of three points in Figure 4.8 with correct phase values $[\phi_0, \phi_1, \phi_2] = [0.0\pi, 0.75\pi, 1.5\pi]$. The wrapped phase sequence is $[\mathrm{W}\phi_0, \mathrm{W}\phi_1, \mathrm{W}\phi_2] = [0.0\pi, 0.75\pi, -0.5\pi]$, and I consider ϕ_0 to be the correct phase. Using the method described above, I can find the correct unwrapped phase sequence:

$$\phi_1 = \phi_0 + \mathrm{W}\Delta\mathrm{W}\phi_1 = \phi_0 + \mathrm{W}(\mathrm{W}\phi_1 - \mathrm{W}\phi_0) \tag{4.33}$$

$$= 0.0 + \mathrm{W}(0.75\pi - 0.0\pi) = 0.75\pi \tag{4.34}$$

$$\phi_2 = \phi_0 + \phi_1 + \mathrm{W}\Delta\mathrm{W}\phi_2 = \phi_0 + \phi_1 + \mathrm{W}(\mathrm{W}\phi_2 - \mathrm{W}\phi_1) \tag{4.35}$$

$$= 0.0\pi + 0.75\pi + \mathrm{W}(-0.5\pi - 0.75\pi) \tag{4.36}$$

$$= 0.0\pi + 0.75\pi + \mathrm{W}(-1.25\pi) \tag{4.37}$$

$$= 0.0\pi + 0.75\pi + 0.75\pi = 1.5\pi. \tag{4.38}$$

4.2.2 Residues

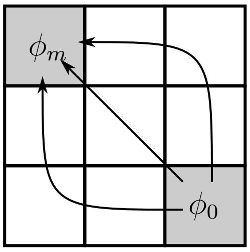

Figure 4.9: Some of the possible paths for unwrapping the phase value ϕ_m, using ϕ_0 as a starting point in a 3 × 3 matrix.

In the Itoh method described above, the path between two points ϕ_m and ϕ_0 was not specified, which means that any path connecting the two points should be valid. Following the example described above, any of the unwrapping paths in Figure 4.9 should be valid choices. However, in reality the obtained result does often depend on the path, which can lead to inconsistent results. The underlying reason for this can be traced to the presence of residues; in 2D phase maps these are 2 × 2 points in a square where the clockwise and counterclockwise path integrals are not equal. In general, an integral of 2 × 2 points, $\sum_{n=0}^{4} \Delta\phi_n = p$ that is path independent must have a value of $p = -p = 0$. However, the value of a counterclockwise integral around a residue is either $p = 2\pi$ (positive residue) or $p = -2\pi$ (negative residue), as shown in Figure 4.10.

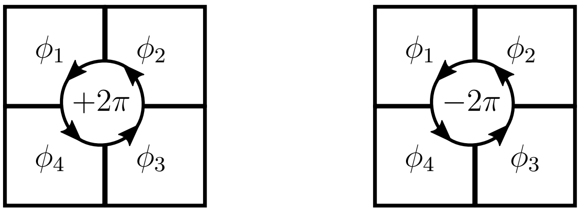

Figure 4.10: Integrating around a closed 4-pixel paths (i.e. where ϕ_1 is both the starting and ending pixel) should yield a path integral of 0, unless there is residue in which case the path integral has a value of $+2\pi$ (positive residue, left) or -2π (negative residue, right)

4.2.3 Goldstein algorithm

The residues thus introduce path dependency in the unwrapping procedure. The foundation of the Goldstein algorithm [77] is to identify the location and sign of each residue, connecting each residue with its closest neighbour of opposite sign (or with the edge of the phase map, whichever is closest) via "branch cuts" that one does not unwrap across. The algorithm is expressed as follows

1. For each pixel in the phase map, add the phases of the pixel itself and its bottom, bottom-right, and right neighbouring pixels. If this sum is not zero, this is a residue with a sign equal to the sign of the sum.

2. For each found residue, find its closest neighbouring residue with opposite sign and join them with the shortest branch cut possible. If the edge of the phase map is closer than other residues, connect the residue with the edge.

3. Starting from any pixel, calculate the phase difference with respect to all its neighbours and add a factor of ±2π if there is a discontinuity (i.e. a phase jump $> 2\pi$), while ignoring discontinuities across branch cuts.

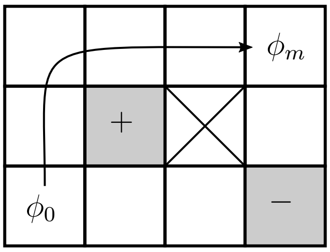

Figure 4.11: Example of a phase unwrapping path that does not cross branch cuts between positive and negative residues, following the Goldstein algorithm.

4.2.4 Quality-guided phase unwrapping

An alternative approach to introducing branch cuts between residues is to remove path dependency by defining a specific unwrapping path. For example, by using a measure of "reliability" of the pixel phase values, a path is defined that first unwraps the phase between pixels that are the most reliable, and so on until the least reliable pixels. These unwrapping algorithms are known as quality guided path methods. A practical measure of reliability is the phase difference between the pixels and its neighbours. For a pixel with indices (i, j) the reliability is then defined as:

$$R = \frac{1}{D(i,j)}, \tag{4.39}$$

where D is defined as:

$$D(i,j) = [H^2(i,j) + V^2(i,j) + D_1^2(i,j) + D_2^2(i,j)]^{1/2}, \tag{4.40}$$

and H the difference between the adjacent horizontal pixels, V the difference between adjacent vertical pixels, and D_1 and D_2 the difference between the diagonals. These functions are given by:

$$\begin{aligned} H(i,j) &= \gamma[\varphi(i-1,j)-\varphi(i,j)]-\gamma[\varphi(i,j)-\varphi(i+1,j)] \\ V(i,j) &= \gamma[\varphi(i,j-1)-\varphi(i,j)]-\gamma[\varphi(i,j)-\varphi(i,j+1)] \\ D_1(i,j) &= \gamma[\varphi(i-1,j-1)-\varphi(i,j)]-\gamma[\varphi(i,j)-\varphi(i+1,j+1)] \\ D_2(i,j) &= \gamma[\varphi(i-1,j+1)-\varphi(i,j)]-\gamma[\varphi(i,j)-\varphi(i+1,j-1)], \end{aligned} \tag{4.41}$$

where γ is an unwrapping function that brings the difference between pixels to the interval $(-\pi, \pi]$. Using this definition of reliability, an unwrapping path is defined that first unwraps the phase between the two pixels with highest summed reliability. The unwrapped pixels join a group of pixels that is then unwrapped with respect to other groups or pixels, and so on until all the pixels are unwrapped [78].

4.2.5 Fringe errors

The Goldstein and quality-guided algorithms can be used to unwrap phase maps that suffers from noise-induced residues. However, it can also give misleading results if applied incorrectly. One such example is with the case of fringe disconnections, which are caused by large changes in the phase over a distance smaller than the spatial resolution of the detector. This is shown in Figure 4.12. This violates the Itoh condition, and the interference fringes may be seen to connect to a neighbouring fringe. In this case, the fringes need to be traced manually in order to preserve the phase information, as was shown in section 4.1.1.

4.3 Inversion techniques

After having obtained a phase map, I need to invert the phase projection in order to obtain the 3D structure of the object from a 2D projection. Consider the projection shown in Figure 4.13: assume that the plasma structure is identical along the z-axis,

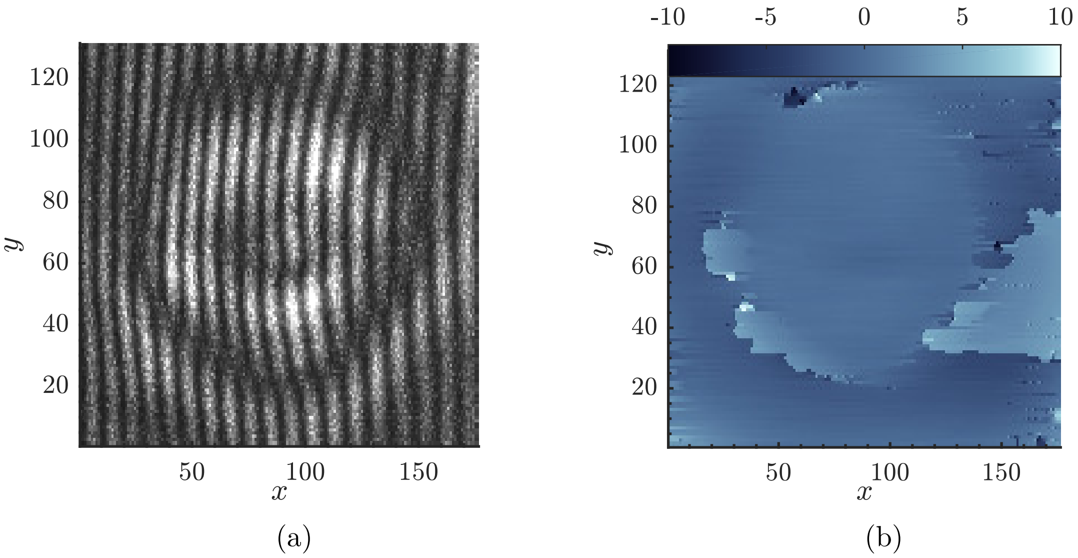

Figure 4.12: Example of a fringe error: the interferogram fringes in (a) are disconnected, leading to phase errors in (b) that can not be corrected by phase unwrapping.

and write it as function of the two transverse dimensions x and y. The phase in each plane is given by $\phi(x, y)$ and I write the 1-dimensional projection as:

$$\Phi(y) = \int_{-\infty}^{\infty} \phi(x, y) dx. \tag{4.42}$$

A fully general object $\phi(x, y)$ cannot be reconstructed with a single or even two axes of

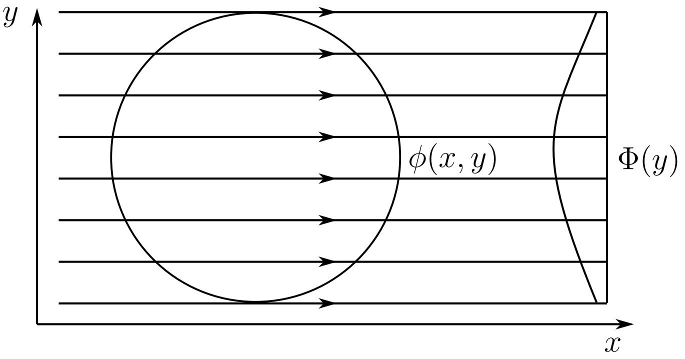

Figure 4.13: Projection of a 2-dimensional structure $\phi(x, y)$ onto a line $\Phi(y)$.

projections, as was demonstrated by Cormack in 1963 [79]. This is a common problem in medical physics, where images of internal organs are recreated using for example X-ray projection images. To achieve this, projections at several angles are used to obtain an increasingly accurate reconstruction of the organ. However, in plasma physics we can often assume that the objects are either fully symmetric under rotation or have one axis of symmetry. In this section we will study some inversion techniques in these simplified cases.

4.3.1 Abel inversion

If the phase $\phi(x, y)$ is assumed to be fully azimuthally symmetric around its centre, I may write it as purely a function of the radius $\phi(x, y) = \phi(r, \theta) = \phi(r)$. In this case, I rewrite equation (4.42) as:

$$\Phi(y) = \int_{-\infty}^{\infty} \phi(r) dx \tag{4.43}$$

$$\left\{ dx = \frac{r dr}{\sqrt{r^2 - y^2}} \right\} \tag{4.44}$$

$$\Phi(y) = 2 \int_{y}^{\infty} \frac{\phi(r) r}{\sqrt{r^2 - y^2}} dr. \tag{4.45}$$

It can be shown [80] that a solution to the above equation is:

$$\phi(r) = -\frac{1}{\pi} \int_{r}^{\infty} \frac{d\Phi}{dy} \frac{dy}{\sqrt{y^2 - r^2}}. \tag{4.46}$$

However, in most cases apart from the purely theoretical the solution cannot be obtained directly from this equation since it is divergent at the lower bound, when $r = y$.

4.3.2 Forward fitting reconstruction

A different approach consists of assuming a trial solution ϕ' and calculating its projection [9]:

$$\Phi^{\text{proj}}(y) = \int_{-\infty}^{\infty} \phi'(x, y) dx. \tag{4.47}$$

By trying a range of different ϕ' and choosing the solution that minimises

$$(\Phi(y) - \Phi^{\text{proj}}(y))^2, \tag{4.48}$$

one obtains an approximate solution to the inversion problem $\phi'(r) \approx \phi(r)$. Since it would be impossible to try an infinite range of solutions ϕ' one usually chooses an orthonormal basis set of functions where the solution is a superposition of these functions, parameterised by m and n: $\phi'(x,y) = \sum_{mn} a_{mn}\phi_{mn}(x,y)$. One choice of basis function are the Laguerre-Gaussian intensity modes [81], in the following way:

$$n_e(x,y) = \sum_{mn} a_{mn} I_{mn}\left(x, y; x_0, y_0, w_0\right), \tag{4.49}$$

where the $a_{m,n}$ are the amplitudes associated with each basis function $I_{m,n}$.

$$\begin{aligned} I_{mn}(x,y) &= |f_{mn}(x,y)|^2 && (4.50)\\ &= \left| \left(\frac{\sqrt{2}}{w_0}\right)^n \left[(x-x_0) + i\left(y-y_0\right)\right]^n \exp\left(-\frac{s^2}{w_0^2}\right) L_m^n\left(2\frac{s^2}{w_0^2}\right)\right|^2, && (4.51)\end{aligned}$$

where $s^2 = (x-x_0)^2 + (y-y_0)^2$ and L_m^n is the generalised Laguerre polynomial of order p and index l, given by:

$$L_m^n(x) = \frac{e^x x^{-n}}{m!}\frac{d^m}{dx^m}\left(e^{-x}x^{m+n}\right). \tag{4.52}$$

Using this basis set asymmetric functions can be generated, by letting x_0 and y_0 take on complex values. The amount of asymmetry along the x-axis is determined by Imag(y_0) and vice versa. With a single axis of projection, the amount of asymmetry in only one axis can be determined.

4.3.3 Two-axis projection forward fitting reconstruction

By adding a second projection axis at 90° to the first, the asymmetry along both axes can be fully determined. I presented a schematic drawing of an experimental setup that could be used for this measurement in Figure 3.7. To show how this analysis works, I generated a simulated plasma channels with the transverse profile shown in Figure 4.14a. I then calculated the projected phase separately along the x and y axes as:

$$\Phi_x^{proj}(y) = \int_{-\infty}^{\infty} \phi(x, y)dx \tag{4.53}$$

$$\Phi_y^{proj}(x) = \int_{-\infty}^{\infty} \phi(x, y)dy. \tag{4.54}$$

as shown in Figure 4.14a. Using the Laguerre-Gaussian basis decomposition, I performed a fit of the projected phases to obtain the inverted phase for each projection which minimised:

$$(\Phi_x(y) - \Phi_x^{proj}(y))^2 \tag{4.55}$$

$$(\Phi_y(y) - \Phi_y^{proj}(x))^2. \tag{4.56}$$

The obtained fits are shown in black dashed lines in Figure 4.14a. Since I used simulated data, the basis parameters of each fit were identical except for the asymmetry parameters $\Im(x_0)$ and $\Im(y_0)$. I could therefore combine the asymmetry parameters from both projected fits to recover the simulated channels with an asymmetry at an arbitrary angle in the plane. The reconstructed channel is shown in Figure 4.14b. While this method would not be able to recover a general 2D object from only two 1D projections, these simulations demonstrate that it is possible to recover objects with a single axis of symmetry using two orthogonal axes of projection. Provided it is experimentally validated, this method could be used to recreate asymmetric plasma channels in future plasma-based accelerators.

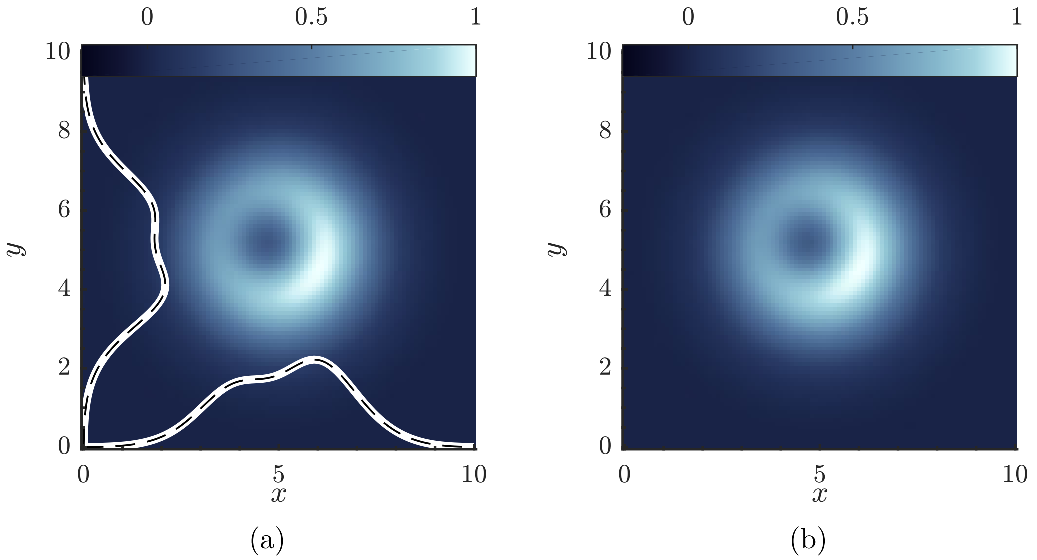

Figure 4.14: (a) Simulated plasma channel with an asymmetry along an axis with an angle of 22.65 degrees. The white solid lines show the projection along the x- and y-axes, and the black dashed lines the projection of the recovered channel in (b).

4.3.4 Deflectometry reconstruction

In deflectometric measurements, for example schlieren imaging (section 3.3.1) or moiré deflectometry (section 3.4.5), the obtained phase is related to the integrated deflection angle $\Theta(y) \propto \int \theta dz \propto \int (\partial\phi/\partial y) dz$. This is similar to the illustration in figure 4.13 for the integrated phase. Following the same procedure as in equation (4.43), I write:

$$\Theta(y) = \int_{-\infty}^{\infty} \frac{\partial \phi(r)}{\partial y} dx \tag{4.57}$$

$$\left\{ dx = \frac{r dr}{\sqrt{r^2 - y^2}}, \frac{\partial \phi(r)}{\partial y} = \frac{\partial \phi(r)}{\partial r} \frac{y}{r} \right\} \tag{4.58}$$

$$\Theta(y) = 2y \int_{y}^{R} \frac{\partial \phi}{\partial y} \frac{\mathrm{d}r}{\sqrt{r^2 - x^2}}, \tag{4.59}$$

with a solution given by the Abel inverse integral, in the special case where the object is symmetrical:

$$\phi(r) = -\frac{1}{\pi} \int_{r}^{R} \Theta(y) \frac{\mathrm{d}y}{\sqrt{y^2 - r^2}}. \tag{4.60}$$

Similarly to the case of inverting interferometric data, the integral is diverging at $x = r$ and so cannot be calculated directly. Instead, numerical integration techniques are employed, for example the two-point algorithm, as described by Kolhe and Agrawal [82]. The electron number density is calculated from the measured deflection angle (assuming rotational symmetry) using the following formula:

$$n_e\left(r_i\right) = \sum_{j=i}^{N+1} D_{ij} \cdot \Theta_j, \tag{4.61}$$

where

$$\begin{aligned} D_{ij} =& \frac{1}{\pi} \cdot \Big(A_{i,j} - A_{i,(j-1)} - j \cdot B_{i,j} + (j-2) \cdot B_{i,(j-1)}\Big) \text{ if } j > i \text{ and } j \neq 2 \\ =& \frac{1}{\pi} \cdot \Big(A_{i,j} - j \cdot B_{i,j} - 1\Big) \quad \text{if } j > i \quad \text{and} \quad j = 2 \\ =& \frac{1}{\pi} \cdot \Big(A_{i,j} - j \cdot B_{i,j}\Big) \quad \text{if } j = i \quad \text{and} \quad i \neq 1 \\ =& 0 \quad \text{if } j = i = 1 \text{ or } j < i, \end{aligned} \tag{4.62}$$

and

$$A_{i,j} = \sqrt{j^2 - (i-1)^2} - \sqrt{(j-1)^2 - (i-1)^2} \tag{4.63}$$

$$B_{i,j} = \ln\left(\frac{j + \sqrt{j^2 - (i-1)^2}}{(j-1) + \sqrt{(j-1)^2 - (i-1)^2}}\right). \tag{4.64}$$

In Figure 4.15a, I show a the deflection angle caused by a simulated plasma object. Using equation (4.61), I recover the plasma number density and compare it with the original density in Figure 4.15b. I found that the difference between the recovered and the original density was less than $0.12 \times 10^{17}\,\mathrm{cm}^{-3}$, for a peak density of $n_0 = 10^{18}\,\mathrm{cm}^{-3}$.

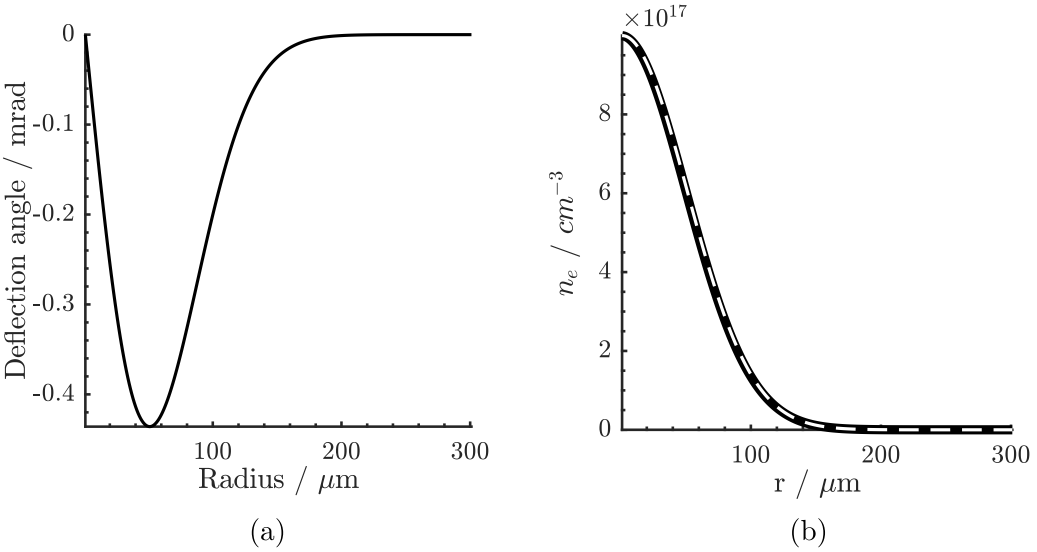

Figure 4.15: (a) Simulated integrated deflection angle caused by a plasma object and (b) reconstructed number density of the plasma object. The black solid line shows the original object and the white dashed line shows the reconstructed object.

4.4 Example interferogram analysis

In the following section, I provide an example of phase extraction from an interferogram, shown in Figure 4.16, using the Fourier transform and CWT methods. I perform phase unwrapping and forward-fitting phase reconstruction in order to recover the original plasma channel. The interferogram was captured by an interferometer diagnostic set up by the author and was used to measure the density and shape of an axicon-generated plasma channel using the optical field ionisation method, described in section 2.7. The channel was formed in a hydrogen plasma by an ionising laser pulse of peak intensity $I \approx 7 \times 10^{15}\,\mathrm{W\,cm^{-2}}$ and radius $r \approx 7.1\,\mu\mathrm{m}$. The density was measured approximately 25 mm downstream of the beginning of the plasma channel [7].

The extracted phase can only be determined up to modulo 2π, and therefore needs to be unwrapped. This is done following the quality-guided phase unwrapping algorithm described in section 4.2.4. After the phase has been unwrapped, a reference phase is subtracted. The reference phase is captured and analysed using the same steps as above, but without any plasma in the beam path, in order to reduce errors introduced

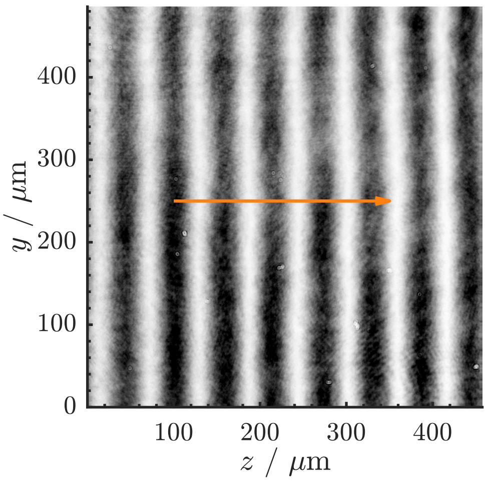

Figure 4.16: Interferogram of a plasma channel. The arrow indicates the direction of laser propagation through the plasma channel waveguide.

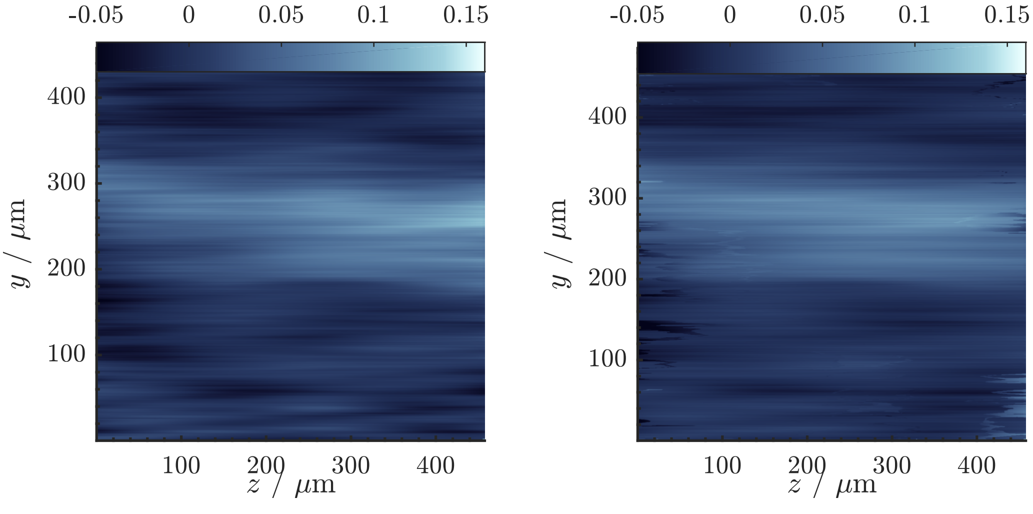

(a) (b)

Figure 4.17: Comparing the obtained phase using (a) the Fourier transform method and (b) the continuous wavelet transform method.

by imperfections in the probe pulse wavefront.

After the unwrapping procedure, residual quadratic background phase is removed by fitting a two-dimensional quadratic surface to the phase map with the signal region removed. The fitted surface is then subtracted from the entire phase map, and the resulting phase is shown in Figure 4.17. Average phase lineouts for both the FT and CWT methods, calculated along the horizontal (z) axis of Figure 4.17, are shown in Figure 4.18.

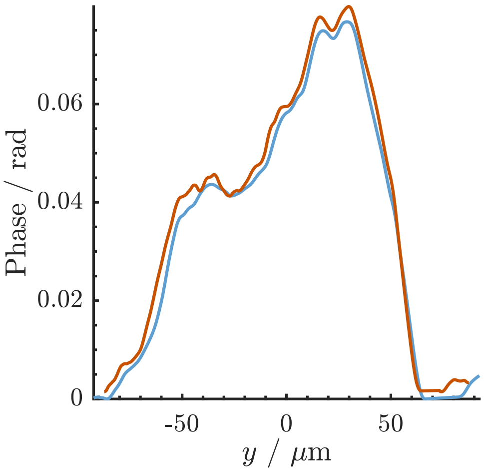

Figure 4.18: Obtained phase projections using the FT (blue) and CWT (red) methods.

Finally, the obtained average phase lineout was inverted – as the obtained phase was highly asymmetric, the standard Abel inversion method could not be used. Instead, I used the Laguerre-Gaussian basis set expansion, as explained in Section 4.3.2. The projected fits are shown together with the average phase lineouts in Figure 4.19.

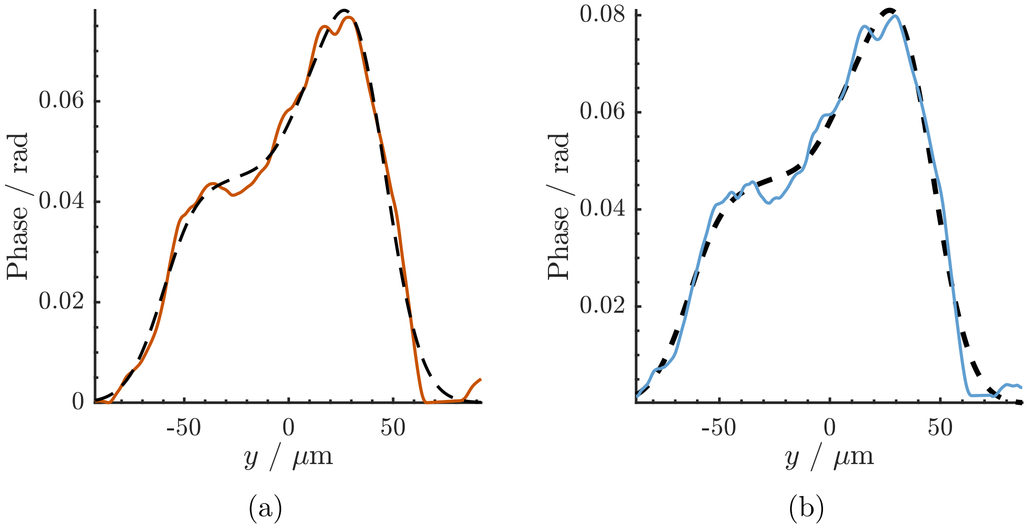

(a)
(b)

Figure 4.19: Comparing the obtained phase using (a) the Fourier transform method and (b) the continuous wavelet transform method. The dashed lines shows the fit to the density lineouts using the Laguerre-Gaussian intensity modes.

In section 3.2, I showed that the phase acquired by propagating through a plasma

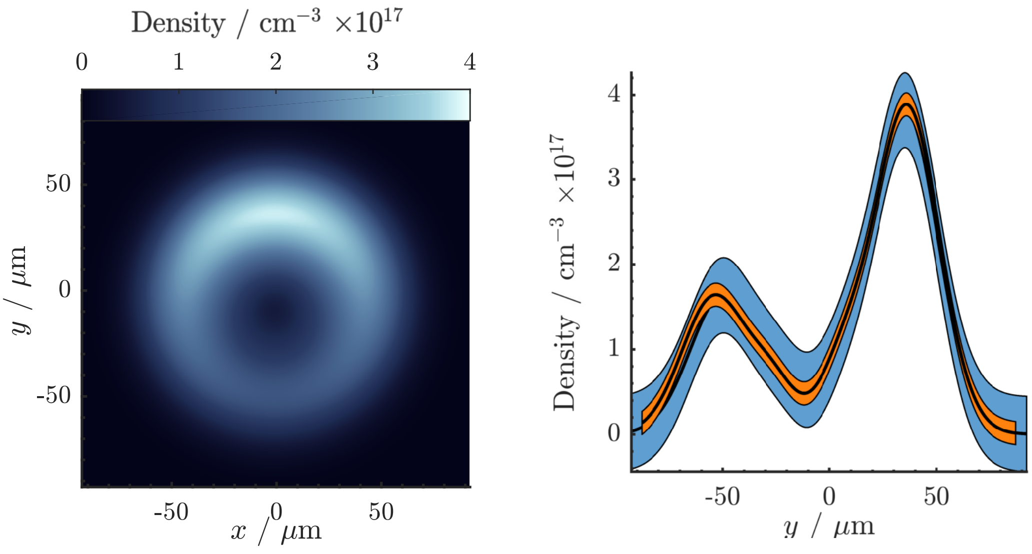

(a) (b)

Figure 4.20: (a) The reconstructed 2D density profile, using the FT method and (b) lineout through $x = 0$ (i.e. $\theta = \pi/2$) comparing the CWT method (blue) with the FT method (red). The filled areas correspond to the uncertainty of the reconstructed density, estimated by calculating the standard deviation of the phase backgrounds, $\sigma(\phi)$, in Figure 4.17, from which the minimum detectable density Δn_e could be obtained.

is given by

$$\Delta\Phi = \int \frac{n_e e^2 \lambda}{4\pi\epsilon_0 m_e} dz. \tag{4.65}$$

Using Equation (4.42), the density from the inverted phase $\phi(x, y)$ can now be calculated as:

$$n_e(x, y) = \frac{4\pi\epsilon_0 m_e}{e^2\lambda}\phi(x, y). \tag{4.66}$$

I use this expression to calculate the plasma density profile, based on the obtained inverted phase using the FT and CWT methods. This is plotted in Figure 4.20, where we can see that the on-axis density of this experimentally measured plasma channel is as low as $n_e \approx 0.5 \times 10^{17}\,\mathrm{cm}^{-3}$. As can be seen, both the CWT and FT yield similar results, with the estimated error of the CWT result being somewhat lower than the FT, due to the smaller background noise as observed in Figure 4.17. The assymmetry observed in Figure 4.20b is most likely due to asymmetries in the intesity of the axicon beam focus, rather than through e.g. a bifurcation process as observed by Sarri et al. [83]. This process occurs when a low-intensity focused laser beam propagates through a plasma; the phase difference between the inner part of the beam (focused by the plasma channel with a diameter smaller than the beam spot size) and the outer part leads to a bifurcation of the ionised plasma. This process may be overcome through the use of relativistic, self-focusing laser beams, which has been studied extensively in the context of inertial confinement fusion [84–87]. However, in an axicon-focused laser beam each part of the line focus corresponds to a distinct part of the incident beam, so the bifurcation process as described above would not be expected to occur here.

4.5 Conclusions

In this chapter I have reviewed the analysis methodology for obtaining density profile of a phase object such as a plasma channel measured using either an interferometer or a deflectometer setup. Using both fake data and experimental data, I showed that the Fourier transform method and continuous wavelet transform methods perform similarly, with the CWT having somewhat lower uncertainty in the reconstructed density. I also discussed the fringe tracing method, which has been all but fully replaced by more advanced methods, but due to being very intuitive and robust can be used to when there are fringe errors in the interferogram. I provided a brief overview of the problems of phase unwrapping and inversion, and introduced methods for inverting the phase profiles of asymmetric objects. I showed that using two projection axes an asymmetric object with a single axis of symmetry can be fully recovered. This concludes my investigation of optical-based plasma density diagnostics, and in the next two chapters I will shift focus to the measurement of plasma wakefields, and the causes of plasma wakefield decay.

Chapter 5

Wakefield decay: theory and experiment

In Chapter 2 I covered the physics underlying the excitation of plasma wakes using either a single pulse (the LWFA scheme) or a train of laser pulses (the MP-LWFA scheme). I showed that the number of pulses that can be used in MP-LWFA is limited by the lifetime of the plasma wakes, which is determined by the interaction between the electrons and the plasma ions. In this chapter, I discuss three mechanisms that contribute to the decay of wakefields: Landau damping, collisional damping, and modulational instability. I also cover experimental aspects of measuring the wakefield amplitude over time, using either electron beam or laser probes, focussing on the Fourier domain holography (FDH) method, together with the temporally encoded spectral shifting (TESS) analysis technique. Lastly, I discuss previous experiments that have been conducted to measure the temporal evolution of plasma wakefields.

5.1 Wakefield decay mechanisms

5.1.1 Parametric instabilities

Viewing plasma oscillations as simple harmonic oscillators, the question arises what happens when several oscillations (e.g. among the electrons and ions in the plasma) interact. It turns out that these interactions can excite new modes of oscillation that draw energy from the fundamental mode — through processes known as parametric instabilities [12]. In the following example, a pump wave excites two coupled oscillators x_1 and x_2 with amplitudes $\bar{x}_1$, $\bar{x}_2$, and resonant frequencies ω_1 and ω_2:

$$\frac{d^2x_1}{dt^2} + \omega_1^2 x_1 = c_1 x_2 E_0 \tag{5.1}$$

$$\frac{d^2x_2}{dt^2} + \omega_2^2 x_2 = c_2 x_1 E_0, \tag{5.2}$$

with coupling parameters c_1 and c_2, and E_0 is a time-dependent pump wave with amplitude $\bar{E}_0$ and frequency ω_0. Assuming solutions of the form $y = A\cos(\omega t)$, we look for the frequencies of the driven oscillators $x_1(\omega)$ and $x_2(\omega')$ that satisfy the above equations. Equation (5.2) becomes:

$$\left(\omega_2^2 - \omega'^2\right) \bar{x}_2 \cos(\omega')t = c_2 \bar{E}_0 \bar{x}_1 \frac{1}{2} \left\{\cos\left[\left(\omega_0 + \omega\right) t\right] + \cos\left[\left(\omega_0 - \omega\right) t\right]\right\}. \tag{5.3}$$

One sees that the frequencies of x_2 satisfy $\omega' = \omega_0 \pm \omega$. The frequencies ω and ω' can be complex; in this case the sign of the imaginary part $\Im(\omega)$ determine whether the oscillation is a decaying mode ($\Im(\omega) < 0$) or an instability mode ($\Im(\omega) > 0$). Assuming that the driven frequencies ω and ω' are close to the resonant frequencies ω_1 and ω_2 one obtains the frequency matching condition for this system of oscillators:

$$\omega_0 = \omega_2 \pm \omega_1. \tag{5.4}$$

In plasmas, there is a corresponding wavelength matching condition between the pump wave and the excited modes, analogous to the conservation of momentum in quantum mechanics:

$$\mathbf{k}_0 \approx \mathbf{k}_2 \pm \mathbf{k}_1. \tag{5.5}$$

In this chapter, I am investigating the decay of plasma wakefields which correspond to the pump wave E_0 in the example above. The other waves x_1 and x_2 may be either electron, ion, or light waves depending on the instability in question. The frequency and wavenumber matching of two electron plasma wave and one ion-acoustic wave is illustrated in Figure 5.1. The parabolic curve shows the electron plasma wave dispersion relation, given by:

$$\omega^2 = \omega_p^2 + 3k^2 v_{\text{th}}^2 \tag{5.6}$$

$$v_{\text{th}} = \sqrt{\frac{k_B T_e}{m_e}}, \tag{5.7}$$

where k_B is the Boltzmann constant, T_e the electron temperature, and m_e the electron mass. Ion acoustic waves are assumed to be one-dimensional and have the dispersion relation [12]:

$$\omega = c_s k \tag{5.8}$$

$$c_s = \sqrt{\frac{k_B T_e + 3k_B T_i}{m_i}}, \tag{5.9}$$

where c_s is the sound speed in a plasma, T_i ion temperature, and m_i the ion mass. The ion acoustic wave dispersion relation is illustrated by the straight lines in Figure 5.1.

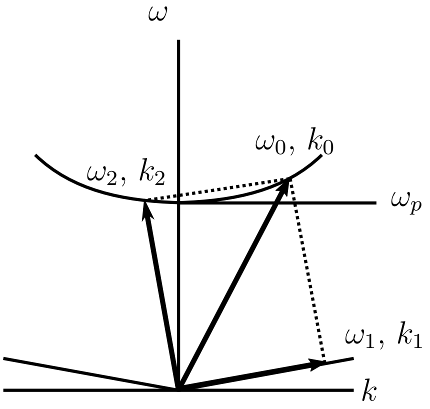

Figure 5.1: Illustration of a parametric decay instability. The arrow marked ω_0, k_0 represents the pump electrostatic wave, which couples into a second, backward-propagating electrostatic wave ω_2, k_2 and an ion acoustic wave ω_1, k_1. The parabolic-shaped curve shows the electron plasma wave dispersion relation, equation (5.6), and the the straight lines shows the dispersion relation of ion acoustic waves, equation (5.8).

5.1.1.1 Modulational instability

The modulational instability* was originally studied to answer the question whether deep-water ocean waves are stable over long distances† [90]. In the modulational instability, the original pump wave is “modulated” by co-propagating sideband waves with frequencies $\omega_1 = \omega_0 - \omega$ and $\omega_2 = \omega_0 + \omega$ and an ion acoustic wave with frequency ω. A simplified illustration the resulting modulation is shown in Figure 5.2. In cases where this modulation is self-reinforcing an instability develops that eventually break up the pump wave into smaller incoherent wave-packets. In plasma physics, the modulational instability has been under theoretical investigation since 1965 [91–93] owing to its importance in the beat-wave accelerator [94]. In this case, the modulational instability progresses through an interaction between an electron plasma wave as the pump and an ion-acoustic wave. The density perturbation of the ion-acoustic wave, with a phase velocity close to the group velocity of the pump, traps pump wave energy in the low-density troughs. This in turn leads to a modulation of the pump which further

---

[*] In the literature, the term oscillating two-stream instability is used interchangeably with modulational instability, however the former term refers to the special case of an infinite wavelength pump [88, 89]

[†] It turns out that they are not, due to the modulational instability

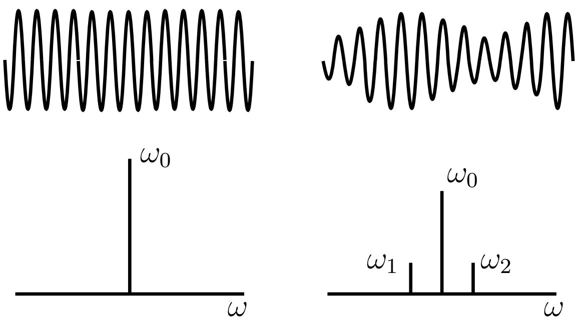

Figure 5.2: Illustration of a modulated wave. The left shows a wave at the unique frequency ω_0, and the right a superposition of a wave with frequency ω_0 and two sidebands with frequencies ω_1 and ω_2 (after [90]).

increases the ion acoustic wave density perturbation through the ponderomotive force [89]. This process is shown in Figure 5.3.

An important parameter in the theoretical calculation of the growth rate of the modulational instability is the ratio of peak oscillation velocity in the wake (v_L) to the thermal velocity (v_t) [95], where:

$$v_L = \frac{eE_L}{m_e\omega_p} \tag{5.10}$$

$$v_t = \left(\frac{k_BT_e}{m_e}\right)^{1/2}, \tag{5.11}$$

where E_L is the electric field of the wakefield. When $v_L/v_t < 1$ the thermal velocity is greater than the oscillation velocity, called the weak field regime. Conversely, the case $v_L/v_t > 1$ is the strong field regime. Henceforth, I will use the decay parameter W to refer to this ratio, which I express in the following way:

$$W = \left(\frac{v_L}{v_t}\right)^2 = \frac{e^2E_L^2}{m_ek_BT_e}\frac{\epsilon_0 m_e}{n_e e^2} = \frac{\epsilon_0 E_L^2}{n_e k_B T_e}. \tag{5.12}$$

An approximate expression for the growth rate γ as a function of the wavenumber k of

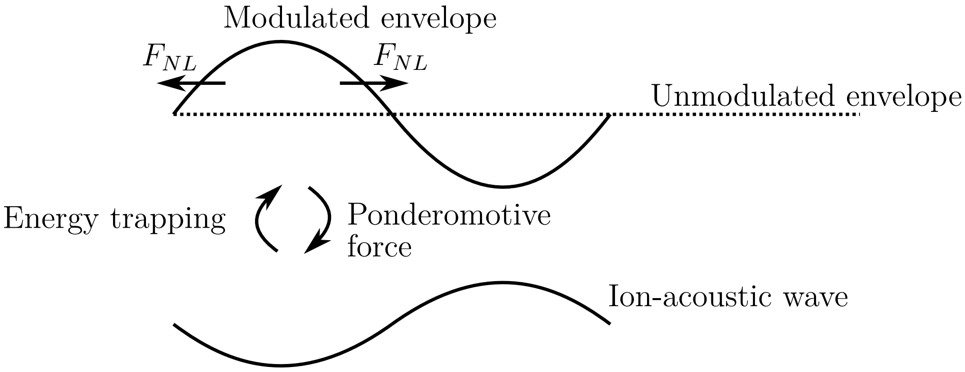

Figure 5.3: Illustration of the modulational instability in a plasma, with the horizontal direction representing a spatial dimension, and the vertical direction the amplitude of the waves. An initially modulated pump electric field associated with an electron plasma wave (due to random fluctuations), top, exerts a non-linear ponderomotive force on the plasma ions, generating an ion-acoustic wave, bottom. The low-density regions of the ion acoustic wave in turn traps pump wave energy and further modulates the pump, leading to the development of an instability (after [89]).

the instability in the case of $k\lambda_{\mathrm{D}} \ll 1$ was given by Mora et al. [94]:

$$\gamma(k)^2 = \omega_{pi}^2 \frac{6k^2\lambda_{\mathrm{D}}^2}{9k^4\lambda_{\mathrm{D}}^4 + 4\gamma^2/\omega_{pe}^2} J_1^2\left(k\lambda_{\mathrm{D}}\frac{v_{\mathrm{L}}}{v_{\mathrm{t}}}\right). \tag{5.13}$$

where the J_1 is the Bessel function of the first kind and λ_{D} the Debye length. Since γ appears both on the left and right hand sides in the above expression, I am required to solve it numerically to obtain the maximum growth rate $\gamma_{\max}$ and the wavenumber $k_{\max}$ at which it occurs. I show a numerical solution to Equation (5.13) at electron density $n_e = 9.7 \times 10^{17}\,\mathrm{cm}^{-3}$, as a function of the decay parameter W in Figure 5.4a, and the obtained wave numbers $k_{\max}$ in Figure 5.4b.

It was found that the weak field limit extends up to $v_L/v_t \leq (\omega_{pe}/\omega_{pi})^{1/3}$ [94], or $W \leq (\omega_{pe}/\omega_{pi})^{2/3} \approx 12$, in which case the maximum growth rate can be written using the simplified expression, in units of rad/s:

$$\gamma_{\max}^{\mathrm{wf}} = 6^{-1/2}\omega_{pi}\left(v_{\mathrm{L}}/v_{te}\right). \tag{5.14}$$

In the strong field regime, $W \geq (\omega_{pe}/\omega_{pi})^{2/3}$, the following simplified expression is

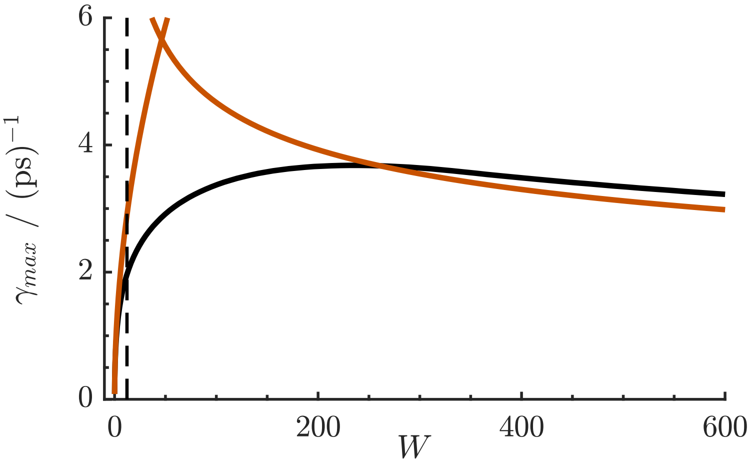

(a)

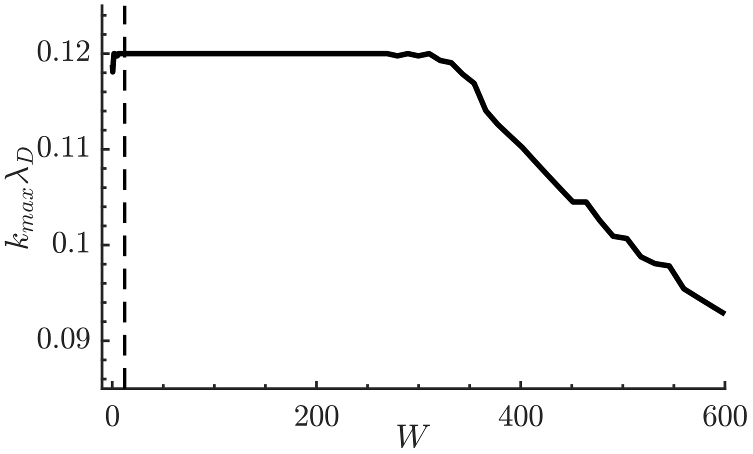

(b)

Figure 5.4: (a) Plot showing the growth rate of the modulational instability as a function of the decay parameter W. The black line shows a numerical solution to equation (5.13), and the horizontal dashed line the limit between the weak field ($W \leq 12$) and the strong field ($W \geq 12$) growth rates. The red lines show the approximate expressions for the growth rate in these regimes. (b) Plot of the wave number k_{max} that maximises the growth rate of the modulational instability in equation (5.13). The horizontal line shows the limit between the weak and strong field regimes, as explained in (a).

obtained:

$$\gamma_{\text{max}}^{\text{sf}} = \left(\frac{3}{2}\right)^{1/4} \omega_{pi} \left(\omega_{pe} v_{te} / \omega_{pi} v_{\text{L}}\right)^{1/2}. \tag{5.15}$$

For $k_B T_e = 2$ eV, $n_e = 9.7 \times 10^{17}$ cm^{-3} and a relative wakefield amplitude $\delta n_e / n_0 = 0.08$ in hydrogen (the same parameters of the experiment presented in Chapter 6) I find the following time scale of the modulational instability using equation (5.13):

$$\tau \sim (\gamma^{\mathrm{sf}}_{\mathrm{max}}/2\pi)^{-1} \approx 3.11\,\mathrm{ps}, \tag{5.16}$$

occurring at the wavenumber $k_{\mathrm{max}} \approx 0.09/\lambda_{\mathrm{D}}$. Note that the growth rate of the instability does not necessarily equal the damping rate of the wakefield, but it is usually assumed to be within a factor of 5 of the decay rate [94]. Also, the growth rate depends on the plasma species, through a dependence on the ion mass m_i and atomic number Z.

5.1.2 Landau damping

Landau damping is a collisionless process through which a plasma can lose energy to thermal electrons in the plasma. Since the electrons have a Maxwellian distribution of velocities, some will be in vicinity of the v_ϕ, the phase velocity of the plasma wake. These electrons are effectively “injected” into the wake and draws energy from oscillating within the electrostatic potential of the wakefield. The damping rate of an electron plasma wave due to Landau damping is given by [96]:

$$\gamma_L = \sqrt{\frac{\pi}{8}} \frac{\omega_{pe}}{k^3\lambda^3_{De}} \exp\left[-\left(1+3k^2\lambda^2_{De}\right)/2k^2\lambda^2_{De}\right], \tag{5.17}$$

where k is the plasma wave vector $k \approx \omega_p/c$ and λ_D is the Debye length $\lambda_D = \sqrt{\epsilon_0 k_B T_e/n_e e^2}$. For a plasma of density $n_e = 9.7 \times 10^{17}\,\mathrm{cm}^{-3}$ and $k_B T_e = 2$ eV we find:

$$\tau \sim \gamma_L^{-1} \approx 3\,\mathrm{ms}. \tag{5.18}$$

5.1.3 Collisional damping

Electron-electron, ion-ion, electron-ion, as well as collisions with neutrals all contribute to removing energy from the wakefield into thermal energy of the plasma. In the following, I will assume a fully ionised plasma, which is reasonable given the relatively high laser intensities used in LWFA. The damping rate of electron plasma waves due to collisions between electrons and ions in this case has been shown to be close to the Braginskii collision frequency [97]:

$$\nu_{\mathrm{coll}} \simeq [4/(3\sqrt{2\pi})]\nu_{ei,th}/2, \tag{5.19}$$

where the thermal collision frequency $\nu_{ei,th}$ is given by:

$$\nu_{\mathrm{ei,th}} = 2\pi \frac{Ze^4 N_e \log\Lambda}{m_e^2 v_{\mathrm{the}}^3}, \tag{5.20}$$

and v_{the} the electron thermal velocity. The Coulomb logarithm ($\log\Lambda$) for electron-ion collisions is given by [98]:

$$\log\Lambda = 23 - \ln\left(n_e^{1/2}[\mathrm{cm}^{-3}]Zk_B(T_e[eV])^{-3/2}\right). \tag{5.21}$$

The above equation is valid for $T_i m_e/m_i < k_B T_e < 10Z^2\mathrm{eV}$, which is the case for LWFA with cold ions and electron plasma temperatures $k_B T < 10$ eV. For $k_B T_e = 2$ eV and $n_e = 9.7 \times 10^{17}\,\mathrm{cm}^{-3}$ we find $\log\Lambda \approx 12$. This gives a collisional damping decay rate of:

$$\tau \sim \nu_{\mathrm{coll}}^{-1} \approx 40\,\mu\mathrm{s}. \tag{5.22}$$

5.1.4 Conclusion: wake decay mechanisms

In this section I have covered three possible decay mechanisms for electron plasma waves; the modulational instability, Landau damping, and collisional damping. I have shown that the modulational instability is significantly faster than the other two, and here we compare these timescales with that of plasma oscillations $\tau_p = 2\pi/\omega_p \approx 0.11\,\mathrm{ps}$. For the $k_B T_e = 2$ eV, $n_e = 9.7 \times 10^{17}\,\mathrm{cm}^{-3}$ and a relative wakefield amplitude $\delta n_e/n_0 = 0.08$, we obtain the typical time scale in units of the plasma period are $\tau^{MI}/\tau_p \sim 30$ for the modulational instability, $\tau^{L}/\tau_p \sim 3\times10^{10}$ for Landau damping, and $\tau^{coll}/\tau_p \sim 4\times10^{8}$ for collisional damping. In Figure 5.5, I show a plot of how the growth or decay rates of these mechanisms depend on the plasma density. In the next section, I will review several methods for measuring the wakefield amplitude, and in Section 5.3 I review previous work on measuring the decay rates of plasma wakefields.

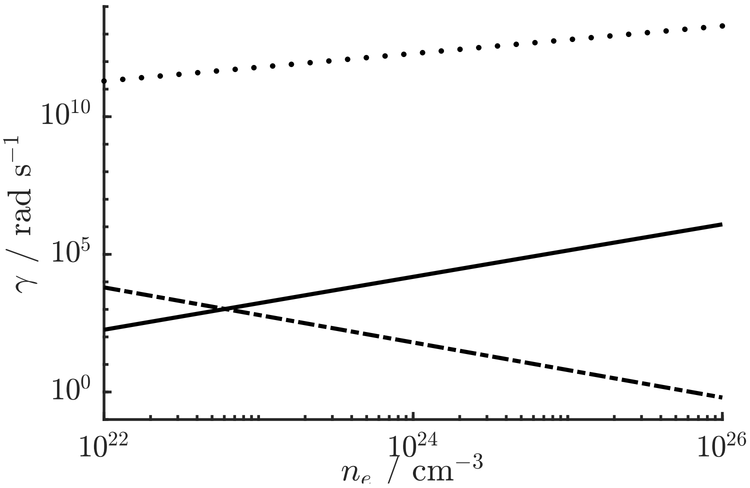

Figure 5.5: Plot showing the growth rate γ in units of rad/s of the three wakefield instabilities and decay rates presented in this chapter. The dotted line shows the strong field modulational instability, the solid line the collisional damping rate, and the dashed line the Landau damping rate.

5.2 Measuring the wakefield amplitude

The ability to accurately measure the structure and temporal evolution of the accelerating wake is crucial for the development of plasma-based accelerators. This is much more challenging than for conventional RF-cavity based particle accelerators, where the macroscopic fields are directly accessible. The plasma wake accelerator is small in size, for laser-drivers typically less than 100 μm in width and with a sub-structure on the order of 30 μm (a single plasma wave). The highly nonlinear processes taking place within the plasma, together with the fluctuating energy and pointing differences of the drive laser pulse means that the shot-to-shot variability is large. The plasma dynamics takes place over many different timescales, from the femtosecond level (electron plasma wave) up to picoseconds (ion motion), nanoseconds (hydrodynamics) and microseconds (plasma recombination). The plasma wave is also not static but travels with a velocity close to c over a distance of typically several centimetres for laser-driven plasma accelerators, and as high as several metres for particle-beam-driven accelerators [99]. While an electrode is often sufficient to measure the oscillating electric fields within an RF-cavity, plasma diagnostics require an altogether different set of measurement techniques. Here I will review some of the most important techniques, based either on electron or light beams.

5.2.1 Electron beam probes

Electron beam probing was one of the first methods used to diagnose a plasma accelerator. In the earliest experiment [100] an electron beam generated at the Argonne National Laboratory Advanced Accelerator Test Facility was used to excite a plasma wakefield. A probe beam was cut out from the main drive beam by introducing a carbon target on a portion of the beam, producing a lower energy beam. The probe beam was then reintroduced onto the same beam axis after passing through a delay line with a variable temporal delay. The experimental layout of the drive-probe electron beam

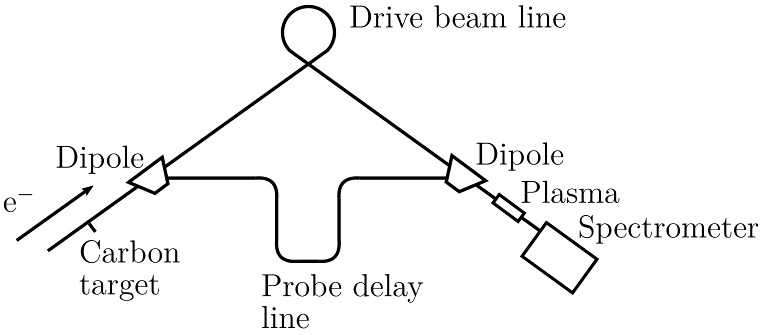

Figure 5.6: Schematic diagram showing how an electron beam can be used to probe the plasma wakefield driven by an electron beam driver (after Rosenzweig et al. [100]).

lines is shown in Figure 5.6. By measuring the spectrum of the probe beam using a dipole magnet with and without the presence of a plasma wakefield, the experimenters could detect energy gains caused by the wakefield. More recently, LWFA-generated electron beams have been used to transversally probe a laser-driven wakefield [101]. This requires electron beams which are shorter than the plasma period ($< 100\,\text{fs}$) and highly energetic ($\gamma \gg 1$), where $\gamma = \sqrt{\frac{1}{1-\beta^2}}$, $\beta = v/c$, and v the electron velocity. When passing through the wakefield, the electrons receive a transverse momentum kick through the interaction with the electric field in the wakefield; this translates into a density modulation which can be detected on a fluorescent screen.

5.2.2 Laser probes

5.2.2.1 Collective Thomson scattering

Some of the earliest methods to diagnose wakefields with laser pulses was to scatter a probe beam off the wakefield either longitudinally or transversely. With this method the wake structure acts as a refractive index grating and scatter the light to frequencies $\omega_{\text{probe}} \pm \omega_p$, with ω_{probe} the probe frequency and ω_p the plasma frequency. The longer wavelength scattered light is known as the Stokes sideband and the shorter wavelength the anti-Stokes sideband. This process is called collective Thomson scattering (CTS), and measuring the frequency separation of the sideband provides a direct measurement of the plasma wavelength. The ratio of the intensities of the (anti-) Stokes sidebands (P_s) to the unscattered light (P_0) can also be used to estimate the amplitude of the plasma wakefield (δn_e) using the equation presented in Reference [102]:

$$\frac{P_s}{P_0} = \frac{1}{4}\delta n_e^2 r_0^2 \lambda^2 L^2 \frac{\sin^2(\Delta K L)}{(\Delta K L)^2}, \tag{5.23}$$

where r_0 is the classical electron radius, λ the probe wavelength, L the plasma length, $\Delta K = k_{pr} - k_s \pm k_p$, with k_{pr} the probe wavenumber, k_p the plasma wavenumber, and k_s the Stokes wavenumber.

5.2.2.2 Frequency domain interferometry

With the development of ultra-short laser pulses ($\sim$ 30 fs) came the possibility of probing the inner structure of the wakefield since the probe was shorter than a plasma wave. The measurements are taken by using a probe-reference pulse pair, where a phase $\phi(r,\zeta)$ due to the wakefield are acquired by the probe beam, co-propagating with a time delay ζ with respect to the wakefield. A simplified drawing of the setup is shown in Figure 5.7a. The phase is retrieved by interfering the probe with the reference pulse that propagated ahead of the wake. It is then read out on a spectrometer by measuring the shift of the spectral fringes generated by the time delay between the probe and reference. This is known as frequency domain interferometry (FDI). The full wakefield is reconstructed by taking multiple shots, each time incrementing the probe-pump delay. This also means that several measurements have to be stitched together to form a single picture, which risks giving rise to errors due to the shot-to-shot variation [99].

5.2.2.3 Frequency domain holography

A further development came with frequency-domain holography (FDH), which was experimentally demonstrated in 2006 [103] with the use of a frequency-doubled probe to distinguish it from the main drive beam. A simple sketch showing the main principle of FDH is shown in Figure 5.7b. FDH relies on a linearly chirped probe that is long enough to cover a few plasma periods in the wakefield and is made to interfere with a similarly chirped reference pulse, as in FDI. The difference with FDI is that the phase imprint on the probe beam covers several plasma wavelengths. Thus one can map the phase structure imprinted on the spectrum of the beam $\varphi(\omega)$ to the temporal phase $\phi(\zeta)$, where $\zeta = t - v_g/c$ is a co-propagating time variable. The captured spectrum can then be used to fully reconstruct the wakefield structure. The spectral interferogram can also be analysed in a slightly simpler way where the plasma wake is assumed to be sinusoidal, and the amplitude averaged over the length of the wake. This approach, known as temporally encoded spectral shifting (TESS), was first published in 2016 [104] and since then extended to also include quasi-nonlinear wakes [105]. The theory behind TESS will be covered in detail in Section 5.2.3.

5.2.2.4 Photon acceleration

Another method for measuring the wakefield amplitude consists of measuring the amount of photon acceleration caused by the plasma refractive index gradient [106]. It is detectable through a frequency shift in the laser pulse spectrum, and for a linear wake, the maximum shift in frequency ($\Delta\omega$) of a laser is given by the following expression:

$$\Delta\omega \approx \frac{\omega_p^2}{2\omega_0}\frac{\delta n_{e_0}}{n_{e_0}} k_p \Delta z \cos\left(k_p \zeta\right). \tag{5.24}$$

Here, ω_0 is the laser frequency, k_p is the plasma wavenumber, ζ the co-propagating time, Δz the total interaction length, and $\delta n_{e0}/n_{e0}$ the relative wakefield amplitude. However, for nonlinear wakes no analytic expression has been developed, and experimental results should instead be compared to simulations.

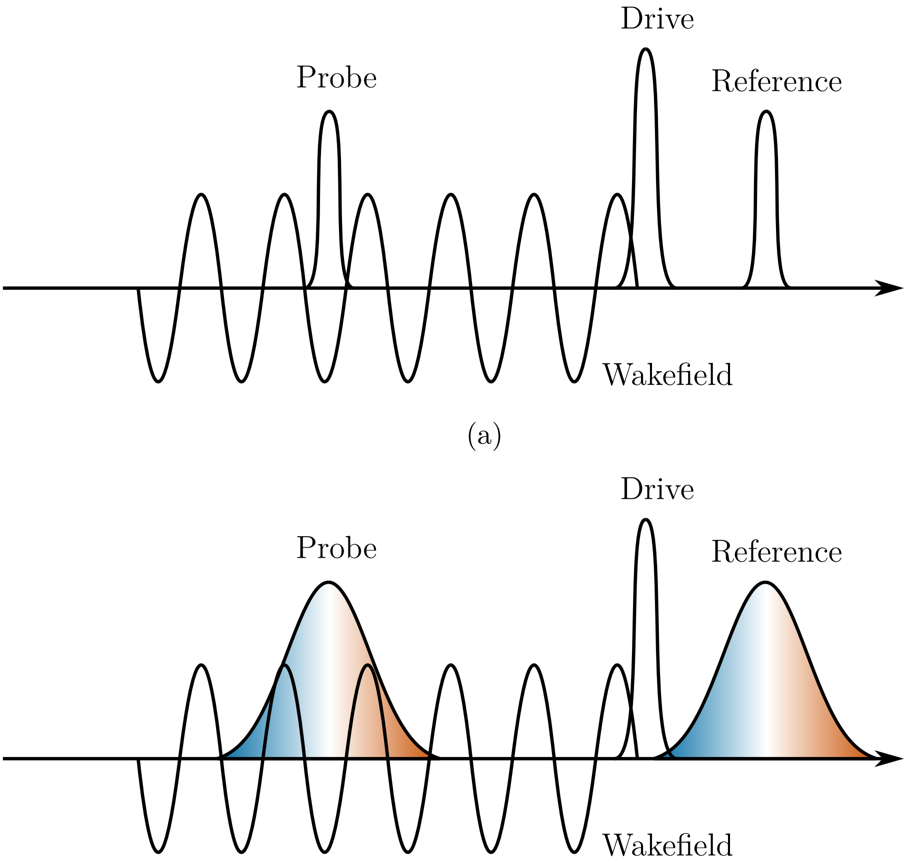

(a)

(b)

Figure 5.7: (a) Frequency domain interferometry (b) Frequency domain holography. A reference pulse precedes the drive beam and is unaffected by the wakefield. A similar probe pulse co-propagates with the wakefield and suffers a phase shift, which can be extracted by interfering it with the reference pulse on a spectrometer. The wakefield causes a modulation of the spectral fringes from which the phase is read out. In FDI, both reference and probe pulses are compressed whereas in FDH they are chirped and stretched in time.

5.2.3 Temporally encoded spectral shifting analysis

TESS is a simplified analysis method to obtain the wakefield amplitude from spectral interferometric data obtained using an FDH diagnostic setup, as outlined above. In the following section, I will follow the method described by Matlis [104]. We start by describing a propagating reference pulse, ahead in time of the pump and probe pulses, by $E_{\mathrm{ref}}(\zeta)$. The probe pulse, co-propagating with the wakefield, acquires a phase $\phi(\zeta)$. In TESS a sinusoidal wake is assumed, and I write the phase in the form:

$$\phi(\zeta) = \phi_0 \sin(\omega_p \zeta), \tag{5.25}$$

where ϕ_0 is the phase amplitude of the sinusoidal wave, and ω_p the plasma frequency. Adding the phase term from Equation (5.25) to the the unperturbed electric field of the probe pulse $E_{\mathrm{probe}}(\zeta)$ I obtain:

$$E'_{\mathrm{probe}}(\zeta) = E_{\mathrm{probe}}(\zeta) \exp[i\phi_0 \sin(\omega_p \zeta)]. \tag{5.26}$$

The Fourier transform of Equation (5.26) is:

$$\mathcal{E}'_{\mathrm{probe}}(\omega) = \frac{1}{\sqrt{2\pi}} \int_{-\infty}^{\infty} E_{\mathrm{probe}}(\zeta) \exp[i\phi_0 \sin(\omega_p \zeta)] \exp(-i\omega\zeta)\, \mathrm{d}\zeta. \tag{5.27}$$

Since the phase is assumed to be sinusoidal, I use the Jacobi-Anger expansion to express the phase term as an infinite sum of Bessel functions of the first kind:

$$\exp[i\phi_0 \sin(\omega_p \zeta)] = \sum_{k=-\infty}^{\infty} J_k(\phi_0) \exp(ik\omega_p \zeta). \tag{5.28}$$

This allows me to rewrite the Fourier transform as:

$$\begin{aligned}\mathcal{E}'_{\mathrm{probe}}(\omega) &= \frac{1}{\sqrt{2\pi}} \int_{-\infty}^{\infty} E_{\mathrm{probe}}(\zeta) \sum_{-\infty}^{\infty} J_k(\phi_0) \exp(ik\omega_p\zeta) \exp(-i\omega\zeta)\,\mathrm{d}\zeta && (5.29)\\ &= \sum_{-\infty}^{\infty} J_k(\phi_0) \frac{1}{\sqrt{2\pi}} \int_{-\infty}^{\infty} E_{\mathrm{probe}}(\zeta) \exp[i(k\omega_p - \omega)\zeta]\,\mathrm{d}\zeta && (5.30)\\ &= \sum_{-\infty}^{\infty} J_k(\phi_0) \mathcal{E}_{\mathrm{probe}}(\omega - k\omega_p). && (5.31)\end{aligned}$$

One sees that the probe spectrum is composed of an infinite number of copies of the unmodulated probe spectrum, each offset by an integer number k times the plasma frequency ω_p, multiplied by a Bessel function $J_k(\phi_0)$. Using a spectrometer allows one to measure the spectral interference pattern between the probe and reference pulses:

$$S(\omega) = |\mathcal{E}_{\mathrm{probe}}(\omega) + \mathcal{E}_{\mathrm{ref}}(\omega)|^2. \tag{5.32}$$

Using Equation (5.31), this can be expanded into a sum of the cross-terms of the probe and reference spectra, as well as the different copies contained in the probe spectrum:

$$\begin{aligned}S(\omega) &= |\mathcal{E}_{\mathrm{probe}}(\omega)|^2 + |\mathcal{E}_{\mathrm{ref}}(\omega)|^2 + \mathcal{E}^*_{\mathrm{probe}}(\omega)\mathcal{E}_{\mathrm{ref}}(\omega) + \text{c.c.} && (5.33)\\ &= \sum_{m,n} J_n(\phi_0) J_m(\phi_0) \mathcal{E}^*_{\mathrm{probe}}(\omega - n\omega_p) \mathcal{E}_{\mathrm{probe}}(\omega - m\omega_p) + |\mathcal{E}_{\mathrm{ref}}(\omega)|^2 && (5.34)\\ &\quad + \sum_k J_k(\phi_0) \mathcal{E}^*_{\mathrm{ref}}(\omega) \mathcal{E}_{\mathrm{probe}}(\omega - k\omega_p) \exp(-i\omega\Delta\zeta) + \text{c.c.},\end{aligned}$$

where c.c. stands for the complex conjugate of the previous term, and I have used the Fourier shift theorem to introduce $\Delta\zeta$, the temporal delay between probe and reference pulses. By calculating the Fourier transform of the spectral interferogram in Equation (5.34), one obtains a temporal representation of the interferogram:

$$S(\zeta) = \sum_m g_m(\phi_0, \zeta, \omega_p) H(\zeta, m\omega_p) + H(\zeta, 0) + \sum_k J_k(\phi_0) H(\zeta - \Delta\zeta, k\omega_p) + \text{c.c.}, \tag{5.35}$$

where the function H is given by:

$$H(\zeta,\omega_p) = \frac{1}{\sqrt{2\pi}} \int_{-\infty}^{\infty} \mathcal{E}^*_{\mathrm{ref}}(\omega)\mathcal{E}_{\mathrm{probe}}(\omega-\omega_p)\exp(i\omega\zeta)\,\mathrm{d}\omega, \tag{5.36}$$

and the function g is given by the sum:

$$g_m(\phi_0,\zeta,\omega_p) = \sum_n J_n(\phi_0)J_{m+n}(\phi_0)\exp(in\omega_p\zeta). \tag{5.37}$$

My approach is now the following:

1. Evaluate $S(\zeta)$ without a wakefield (setting $\omega_p = 0$)
2. Evaluate $S(\zeta)$ with a wakefield (setting $\omega_p \neq 0$)

In the following, I assume that the probe and reference pulses have identical Gaussian spectra, but the calculations are similar for non-Gaussian spectra [105]. Starting with first point, I evaluate the function $H(\zeta,\omega_p)$ at $\omega_p = 0$. For a Gaussian spectrum, I write $\mathcal{E}_{\mathrm{ref}}(\omega)$ as:

$$\mathcal{E}_{\mathrm{probe}}(\omega) = \mathcal{E}_{\mathrm{ref}}(\omega) = A\exp\left[-\frac{1}{2}\left(\frac{\omega-\omega_0}{\delta\omega}\right)^2 + i\varphi^{(2)}\left(\frac{\omega-\omega_0}{\delta\omega}\right)^2\right], \tag{5.38}$$

with amplitude A, centre frequency ω_0, bandwidth $\delta\omega$, and group delay dispersion $\varphi^{(2)}$. Using equation (5.38) I obtain:

$$H_0(\zeta) \equiv H(\zeta,\omega_p=0) = \frac{1}{\sqrt{2\pi}} \int_{-\infty}^{\infty} \mathcal{E}^*_{\mathrm{ref}}(\omega)\mathcal{E}_{\mathrm{probe}}(\omega)\exp\left(i\omega\zeta\right)\mathrm{d}\omega \tag{5.39}$$

$$= \delta\omega\frac{A^2}{\sqrt{2}}\exp\left[i\omega_0\zeta - \frac{1}{4}\left(\zeta\delta\omega\right)^2\right]. \tag{5.40}$$

Using equation (5.40) I can then evaluate $S(\zeta)$ using $\omega_p = 0$ and $\phi_0 = 0$. Since all Bessel functions of the first kind apart from $k = 0$, $J_{|k|>0}(\phi_0)$ are zero at $\phi_0 = 0$, I obtain:

$$S(\zeta) = 2H_0(\zeta) + H_0(\zeta-\Delta\zeta) + H_0(\zeta+\Delta\zeta), \tag{5.41}$$

and upon evaluating the magnitude $|S(\zeta)|$ I obtain three peaks: one at $\zeta = 0$, one at $\zeta = \Delta\zeta$, and one at $\zeta = -\Delta\zeta$. A sketch of this is shown in Figure 5.8a.

In the case of $\omega_p \neq 0$, I instead have [104]:

$$H(\zeta, k\omega_p) = \mathcal{F}(k\omega_p) \exp\left(\frac{ik\omega_p\zeta}{2}\right) H_0(\zeta + \varphi^{(2)}k\omega_p), \tag{5.42}$$

and using this I rewrite equation (5.35) as:

$$S(\zeta) = \underbrace{\sum_m g_m(\phi_0, \zeta, \omega_p) f(m\omega_p) H_0(\zeta + m\tau) + H_0(\zeta)}_{\text{DC peak}} \tag{5.43}$$

$$+ \underbrace{\sum_k J_k(\phi_0)\mathcal{F}(k\omega_p) H_0(t - \Delta\zeta + k\tau) + \text{c.c.}}_{\text{Sidebands+satellites}}, \tag{5.44}$$

where I have introduced $\tau \equiv \varphi^{(2)}\omega_p$, and $\mathcal{F}(k\omega_p)$ is a spectral overlap factor:

$$\mathcal{F}(k\omega_p) = \exp\left\{-\frac{1}{4}\left(\frac{k\omega_p}{\delta\omega}\right)\right\}. \tag{5.45}$$

In the above equation the overlap function $\mathcal{F}(k\omega_p)$ was evaluated assuming that the spectrum is Gaussian, using equation (5.38). For non-Gaussian spectra, a more general form of the overlap factor is given by [105]:

$$\mathcal{F}(k\omega_p) = \frac{\int_{-\infty}^{\infty} |\mathcal{E}_{\text{probe}}(\omega + k\omega_p)||\mathcal{E}_{\text{ref}}(\omega)| d\omega}{\int_{-\infty}^{\infty} |\mathcal{E}_{\text{probe}}(\omega)||\mathcal{E}_{\text{ref}}(\omega)| d\omega}. \tag{5.46}$$

The “sideband” term in equation (5.44) contains TESS satellite peaks ($k \neq 0$) and the sideband caused by interference ($k = 0$). The magnitude $|S(\zeta)|$ in the presence of a wakefield is shown in Figure 5.8b. The ratio r between the first TESS satellite in equation (5.44) ($k = 1$ term, evaluated at $\zeta = \Delta\zeta - T$) and the sideband ($k = 0$ term, evaluated at $\zeta = \Delta\zeta$), is:

$$r = \frac{J_1(\phi_0) f(\omega_p)}{J_0(\phi_0)}. \tag{5.47}$$

For small amplitudes $\phi_0 \ll 1$, the Bessel functions of the first kind J_α can be expanded as:

$$J_\alpha(\phi_0) \approx \frac{1}{(\alpha - 1)!} \left(\frac{\phi_0}{2}\right)^\alpha \tag{5.48}$$

$$J_0(\phi_0) \approx 1 \tag{5.49}$$

$$J_1(\phi_0) \approx \frac{\phi_0}{2}. \tag{5.50}$$

The phase amplitude ϕ_0 can therefore be expressed as:

$$\phi_0 = \frac{2r}{f(\omega_p)}. \tag{5.51}$$

Using ϕ_0 I can now calculate the density modulation $\delta n_e / \delta n_{e0}$. I have already assumed that the wakefield is sinusoidal over the duration of the probe pulse. Over the co-propagating time ζ, I write the plasma density as:

$$n_e(\zeta) = n_{e0} + \delta n_e \sin(\omega_p \zeta). \tag{5.52}$$

Previously, in Section 3.2, I found that the phase difference acquired by a laser propagating through plasma is:

$$\Delta\phi(\zeta) = \int \frac{n_e(\zeta) e^2 \lambda}{4\pi\epsilon_0 m_e} \, \mathrm{d}z. \tag{5.53}$$

Inserting Equation (5.52) I obtain:

$$\Delta\phi(\zeta) = \int \frac{e^2 \lambda}{4\pi\epsilon_0 m_e} [n_{e0} + \delta n_e \sin(\omega_p \zeta)] \, \mathrm{d}z. \tag{5.54}$$

Removing the constant density term n_{e0} and replacing $\omega_p^2/n_{e0} = e^2/\epsilon_0 m_e$:

$$\Delta\phi(\zeta) = \int \frac{\omega_p^2 \lambda}{4\pi} \frac{\delta n_e}{n_{e0}} \sin(\omega_p \zeta)\, \mathrm{d}z. \tag{5.55}$$

Assuming that there is no significant longitudinal spatial variation we can integrate over the length L of the plasma:

$$\Delta\phi(\zeta) = \frac{\omega_p^2 \lambda}{4\pi} \frac{\delta n_e}{n_{e0}} \sin(\omega_p \zeta) L. \tag{5.56}$$

Comparing the above expression with equation (5.25) I identify:

$$\phi_0 = \frac{\omega_p^2 \lambda}{4\pi} \frac{\delta n_e}{n_{e0}} L. \tag{5.57}$$

Using Equation (5.51) we obtain an expression for the relative wakefield amplitude $\delta n_e/n_{e0}$ as a function of the satellite-to-sideband ratio r and the spectral overlap $\mathcal{F}(\omega_p)$:

$$\begin{aligned} \frac{\delta n_e}{n_{e0}} &= \phi_0 \frac{4\pi}{\omega_p^2 \lambda L} && (5.58) \\ &= \frac{2r}{\mathcal{F}(\omega_p)} \frac{4\pi}{\omega_p^2 \lambda L}. && (5.59) \end{aligned}$$

5.2.4 Frequency domain holography analysis

Using the frequency domain holography data I not only obtain the wakefield amplitude using the TESS method, as shown above, but also recreate the probe beam electric field amplitude and phase. From this measurement I obtain the wakefield amplitude over the co-propagating time coordinate ζ, $\delta n_e(\zeta)/n_0$. Following Matlis et al. [103], I assume that the reference pulse is unperturbed by the plasma, while the probe pulse suffers a phase shift $\phi_{\mathrm{wake}}(\zeta)$ after propagation through the plasma. I write the perturbed probe

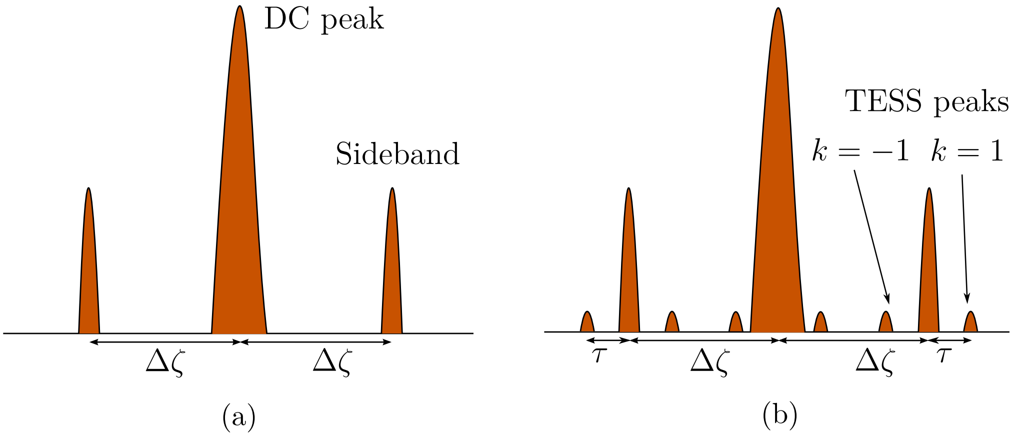

Figure 5.8: Amplitude of the Fourier transform of a spectral interferogram: (a) without a wakefield, (b) modulated by a wakefield, with the first order ($k = \pm 1$) TESS peaks separated by τ from the DC peak and sidebands. The sidebands are due to the probe-reference interference.

electric field $E'_{\text{probe}}(\zeta)$ as:

$$E'_{\text{probe}}(\zeta) = E_{\text{probe}}(\zeta) \exp\left[i\phi_{\text{wake}}(\zeta)\right]. \tag{5.60}$$

The FDH measurement is made in the frequency rather than temporal domain, so I perform forward Fourier transforms of the probe and reference pulses. These are simply:

$$\mathcal{E}'_{\text{probe}}(\omega) = \frac{1}{\sqrt{2\pi}} \int_{-\infty}^{\infty} E_{\text{probe}}(\zeta) \exp[i\phi_{\text{wake}}(\zeta)] \exp(-i\omega\zeta) \mathrm{d}\zeta \tag{5.61}$$

$$\mathcal{E}_{\text{ref}}(\omega) = \frac{1}{\sqrt{2\pi}} \int_{-\infty}^{\infty} E_{\text{ref}}(\zeta + \Delta\zeta) \exp(-i\omega\zeta) \mathrm{d}\zeta, \tag{5.62}$$

where, as in the TESS analysis above, the factor $\Delta\zeta$ accounts for the earlier time-of-arrival of the reference pulse on the spectrometer (see Figure 5.7b). Measuring both probe and reference pulses simultaneously on an imaging spectrometer, I obtain a spectral interference pattern

$$S(\omega) = \left|\mathcal{E}_{\text{probe}}(\omega) + \mathcal{E}_{\text{ref}}(\omega)\right|^2 \tag{5.63}$$

$$= |\mathcal{E}_{\text{probe}}(\omega)|^2 + |\mathcal{E}_{\text{ref}}(\omega)|^2 + \mathcal{E}^*_{\text{probe}}(\omega)\mathcal{E}_{\text{ref}}(\omega) + \mathcal{E}_{\text{probe}}(\omega)\mathcal{E}^*_{\text{ref}}(\omega), \tag{5.64}$$

where the first two terms are just the spectral intensities of the individual laser pulses, while the two latter terms are interference terms. As was shown in Equation (5.44), the Fourier transformed interference pattern $S(\zeta)$ reveals that the interference terms are separated from the background intensity terms by $\Delta\zeta$. It is therefore possible to isolate the interference terms in the temporal domain, and then transform back to the frequency domain in order to obtain:

$$S_{\text{interference}}(\omega) = \mathcal{E}_{\text{probe}}(\omega)\mathcal{E}^{*}_{\text{ref}}(\omega), \tag{5.65}$$

which I write as:

$$S_{\text{interference}}(\omega) = \left|\mathcal{E}_{\text{probe}}(\omega)\right| \left|\mathcal{E}_{\text{r}}(\omega)\right| \exp\left[\mathrm{i}\varphi_{\text{probe}}(\omega) - \mathrm{i}\varphi_{\text{ref}}\left(\omega\right)\right]. \tag{5.66}$$

To a first approximation, I assume that the spectral phases $\varphi_{\text{probe}}\left(\omega\right)$ and $\varphi_{\text{ref}}\left(\omega\right)$ of the probe and reference pulses only contain terms up to the third order:

$$\varphi_{\text{ref}}(\omega) \approx \varphi^{(0)}_{\text{ref}} + \varphi^{(1)}_{\text{ref}}\left(\omega-\omega_0\right) + \frac{1}{2}\varphi^{(2)}_{\text{ref}}\left(\omega-\omega_0\right)^2 + \frac{1}{6}\varphi^{(3)}_{\text{ref}}\left(\omega-\omega_0\right)^3 \tag{5.67}$$

$$\varphi_{\text{probe}}(\omega) \approx \varphi^{(0)}_{\text{probe}} + \varphi^{(1)}_{\text{pr}}(\omega-\omega_0) + \frac{1}{2}\varphi^{(2)}_{\text{probe}}(\omega-\omega_0)^2 + \frac{1}{6}\varphi^{(3)}_{\text{probe}}(\omega-\omega_0)^3 + \varphi_{\text{wake}}(\omega), \tag{5.68}$$

where ω_0 is the central frequency and $\varphi^{(2)}$ is the group delay dispersion (GDD). By measuring the spectral phase and amplitude of the reference pulse separately (this is covered in Section 6.2.3), I reconstruct the probe electric field in the frequency domain as:

$$\frac{\left|\mathcal{E}_{\text{probe}}(\omega)\right| \left|\mathcal{E}_{\text{ref}}(\omega)\right|}{\left|\mathcal{E}_{\text{ref}}(\omega)\right|} \exp\left[\mathrm{i}\varphi_{\text{probe}}(\omega) - \mathrm{i}\varphi_{\text{ref}}(\omega)\right] \exp\left[\mathrm{i}\varphi_{\text{ref}}(\omega)\right] \tag{5.69}$$

$$= \left|\mathcal{E}_{\text{probe}}(\omega)\right| \exp\left[\mathrm{i}\varphi_{\text{probe}}(\omega)\right] \tag{5.70}$$

$$= \mathcal{E}_{\text{probe}}(\omega). \tag{5.71}$$

One thus sees that:

$$\mathcal{E}_{\mathrm{pr}}(\omega) = S_{\mathrm{interference}}(\omega) \exp\left[\mathrm{i}\varphi_{\mathrm{ref}}\left(\omega\right)\right] / \left|\mathcal{E}_{\mathrm{r}}(\omega)\right|. \tag{5.72}$$

I can recover the electric field in the temporal domain by performing an inverse Fourier transform

$$E'_{\mathrm{probe}}(\zeta) = \frac{1}{\sqrt{2\pi}} \int_{-\infty}^{\infty} \mathcal{E}_{\mathrm{probe}}(\omega) \exp(-\mathrm{i}\omega\zeta) \mathrm{d}\zeta. \tag{5.73}$$

The probe temporal phase is also recovered from the electric field:

$$\phi'_{\mathrm{probe}} = \arg[E'_{\mathrm{probe}}(\zeta)] \approx \phi_{\mathrm{probe}}(\zeta) + \phi_{\mathrm{wake}}(\zeta), \tag{5.74}$$

where $\phi_{\mathrm{probe}}(\zeta)$ is the unmodulated probe phase. The phase shift induced by the wakefield is thus either be recovered from ϕ_{probe} by subtracting the phase recovered from a reference measurement, $\phi_{\mathrm{probe}}(\zeta)$, taken without any plasma in the gas cell:

$$\phi_{\mathrm{wake}}(\zeta) = \phi'_{\mathrm{probe}}(\zeta) - \phi_{\mathrm{probe}}(\zeta). \tag{5.75}$$

The phase is only determined up to a factor of 2π, and therefore needs to be unwrapped. This procedure is covered in Section 4.2. Assuming again that the longitudinal variation of the density within the gas cell is small, I integrate Equation (5.53) over the plasma length L to obtain (having subtracted a constant background):

$$\Delta\phi(\zeta) = \frac{\delta n_e(\zeta) e^2 \lambda}{4\pi\epsilon_0 m_e} L. \tag{5.76}$$

The wakefield amplitude is therefore:

$$\delta n_e(\zeta) = \frac{4\pi\epsilon_0 m_e}{e^2\lambda L}\Delta\phi(\zeta) \tag{5.77}$$

$$\frac{\delta n_e(\zeta)}{n_{e0}} = \frac{4\pi}{\omega_p^2\lambda L}\Delta\phi(\zeta). \tag{5.78}$$

5.3 Previous wakefield decay experiments

I will now review some of the previous experimental work that has been carried out to both measure the wakefield decay rate as well as to determine the leading causes of wakefield decay. The relevant experiments, parameters, and key results are summarised in Table 5.1. I have also listed the experimental parameters and results obtained in this thesis; this is presented in detail in Chapter 6. In addition to the measured decay rate, which is presented in normalised in units of plasma periods, some experimental parameters are of particular importance. The first is $(\lambda_p/\pi w_0)^2$, which I showed in Section 2.4 is the ratio between the radial and longitudinal components of the wakefield. As was shown by Marqués *et al.* [15], radial wakefields decay from different mechanisms than longitudinal wakefields, as they interact with the surrounding neutral gas. Of the experiments presented here, that of Marqués *et al.* mentioned above and Kotaki *et al.* [107] were performed in the radial regime $(\lambda_p/\pi w_0)^2 > 1$, and the others in the longitudinal regime. A second important parameter is $W = (v_L/v_t)^2$, the ratio of electron plasma wave energy to thermal energy in the plasma, as this determines the rate of the modulational instability. While the importance of the pump beam length relative to the plasma period has not yet been firmly established, it is noteworthy that most experiments used drive lasers with temporal durations much longer than the plasma period, except for the those by Marqués *et al.* and Kotaki *et al.* This fact complicates the theory behind the modulational instability presented in Section 5.1.1.1, as the pump wave also needs to be added to the calculations. Finally, the choice of gas target may also be significant; with the use of a gas jet, there is considerably longitudinal variation in the density which could affect the measurements by averaging over regions with different plasma frequencies. In comparison, gas chambers and gas cells are capable of providing plasmas with a much more stable plasma density.

Using the results presented in Table 5.1 I produced a plot comparing these results with those predicted from the modulational instability theory presented in Section 5.1.1.1. I excluded the experiments conducted in the radial wakefield regime. The resulting plot is shown in Figure 5.9, with the measured decay time plotted as a function of the parameter W. As can be seen, all the reported results show a decay time on $\sim$ 100 plasma periods, and are consistent with the theory of modulational instability.

Table 5.1: Laser and plasma parameters in wakefield lifetime experiments.

Source	Experiment	Diagnostic	Gas	Target	n_e / cm^{-3}	T / eV	$\left(\frac{\lambda_p}{\pi\sigma}\right)^2$	W	$\delta n_e/n_0$	E_z / (GV/m)	τ_{wf}/T_p
Marqués et al., 1998	LWFA	FDI	He	Chamber	$4e15 - 1e17$	14	31.4	365	0.1	4.3	$2 - 50$
Kotaki et al., 2002	LWFA	FDI	He	Gas jet	$7.4e17$	13	1.93	1148	0.75	20	9.7
Ting et al., 1996	SM-LWFA	CTS	H & He	Gas jet	$1e19$	10	0.62	255	0.1	30	171 ± 29
LeBlanc et al., 1996	SM-LWFA	CTS	He	Gas jet	$3e19$	2500	0.023	5.11	0.15	110	132 ± 14
Chen et al., 2000	SM-LWFA	CTS	He	Gas jet	$3.7e19$	1000	0.041	4.60	0.1	83	139
Moulin et al., 1994	LBWA	CTS	D	Gas cell	$1.07e17$	20	0.113	274	0.05	3.7	63 ± 59[a]
This work	LWFA	FDH	H & D	Gas cell	9.7×10^{17}	2	0.042	,750 (H) 260 (D)	0.055	7.6	97 ± 32, 178 ± 102

Source	τ_L / fs	λ / nm	E_{laser} / J	w_0 / µm	τ_{probe} / ps	$I_{\max}$ / W cm^{-2}	a_0
Marqués et al., 1998	120	800	40×10^{-3}	6 ± 1	120	2×10^{17}	0.3
Kotaki et al., 2002	52	800	108×10^{-3}	8.9	52	8.4×10^{17}	0.62
Ting et al., 1996	400	800	0.8	4.25	400	7×10^{18}	2.21
LeBlanc et al., 1996	400	1053	1.2	8.9	400	1.2×10^{18}	0.98
Chen et al., 2000	400	1053	0.4	6.8	400	6.9×10^{17}	0.74
Moulin et al., 1994	160×10^3, 90×10^3	1064, 1053	7, 7	100 ± 20	160×10^3	3×10^{14}, 6×10^{14}	0.016, 0.022
This work	48.9 ± 6.3	800	1.68 ± 0.06	52.3 ± 0.8	48.9 ± 6.3	6.5×10^{17}	0.54 ± 0.18

---

[a] This result was reported as the time between the wakefield saturation and the (later) peak of the drive laser. We converted this to wakefield lifetime by assuming that the wakefield started at $(1/e^2)$ of the maximum intensity of the drive pulse.

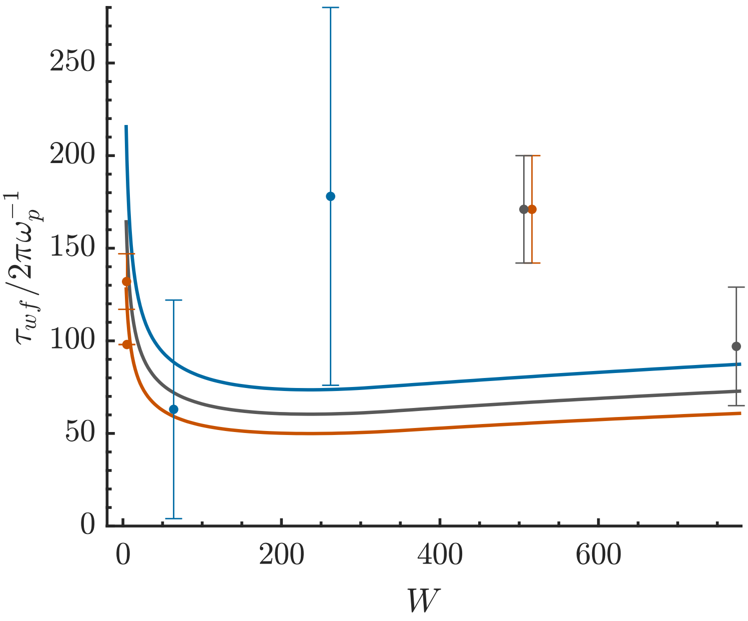

Figure 5.9: Plot showing the measured wakefield lifetime, in units of the plasma period, as a function of initial wakefield amplitude for the experiments presented in Table 5.1. The three lines shows the time scale $\tau \sim 2\pi\gamma^{-1}$ of the modulational instability using Equation (5.13), multiplied by a factor of 4. This factor corresponds to the number of e-foldings of the instability before it causes the wakefield to decay, and was chosen by hand to approximately fit the data. Each point represents a different experiment and the vertical lines the corresponding errors (the experiments by Marqués *et al.* and Kotaki *et al.* were excluded as they were in the radial wakefield regime). The colours of the lines and the points represent the plasma species that was used: hydrogen (gray), deuterium (blue) and helium (red).

Chapter 6

Measuring wakefield decay

In this chapter, I present the results of an experiment that was conducted at the Central Laser Facility, UK, to measure the decay rates of linear wakefields in hydrogen and deuterium. As was shown in the previous chapter, there are numerous decay processes taking place simultaneously in the plasma. I also reviewed several previous experiments that have measured the wakefield lifetime. The experiment discussed here differs from these previous experiments in the following ways:

1. The parameter regime: this is the first experiment in the linear, short-pulse LWFA regime. This represents a significant simplification in the setup compared the earlier LBWA and SM-LWFA experiments, where a pulse much longer than the plasma wavelength is used to excite a plasma wakefield. In these latter schemes, the plasma instabilities are developing alongside the pump, which is not the case in the short-pulse regime. Secondly, in the present work the wakefield generated was in the linear regime. Thirdly, I used a gas cell which is much uniform in the longitudinal plasma density compared to a gas jet, which was used in many of the earlier works.

2. Diagnostic: I used for the first time a frequency domain holography (FDH) diagnostic to measure the wakefield decay. While I do not expect the results to

be significantly different from, for example, a frequency domain interferometry diagnostic, FDH has the advantage of being single-shot. This allows in principle the measurement of several plasma oscillations with a single shot. Since in the present work I seek to measure the wakefield decay over several picoseconds, I still scan over a range of temporal delays, but still require many fewer shots compared to FDI.

This chapter is organised in the following way. First, I discuss particle-in-cell simulations that were conducted to estimate the initial plasma temperature in the experiments. I also discuss simulations of the wakefield decay process that were conducted by group member Alexander von Boetticher. Next, I explain the experimental layout and the diagnostic design. I present measurements to characterise the focal spot size and spectral phase of the drive pulse. Finally, we analyse the results using the TESS analysis method and compare the obtained results to the particle-in-cell simulations and discuss the implications for the MP-LWFA scheme.

6.1 Particle-in-cell simulations

6.1.1 Estimating the temperature

Table 6.1: Simulation parameters used in 2D PIC simulations to estimate the plasma electron temperature.

Parameter	Value	Unit
Particles per cell	32	-
Simulation length	150	μm
Simulation width	300	μm
Resolution (along laser axis)	0.05	λ
Resolution (perpendicular to laser axis)	0.1	λ
Gas species	H_2	-
Plasma density	9.7×10^{17}	cm^{-3}
Laser temporal duration	48.9	fs
Laser spot width	52.3	μm
Laser intensity	6.5×10^{17}	Wcm^{-2}

In Section 5.1.1.1 I introduced the decay parameter W that determines the growth rate of the modulational instability. It depends on the wake electric field, plasma density, and plasma electron temperature:

$$W = \frac{\epsilon_0 E_L^2}{n_e k_B T_e}. \tag{6.1}$$

Experimentally I was able to directly measure both the plasma density (n_e) and the wake electric field (E_L). However, in the experiment presented in this chapter we did not directly measure the temperature (T_e). In order to obtain an estimate of the temperature, I performed 2D particle-in-cell (PIC) simulations in the code Extendable PIC Open Collaboration (EPOCH) [108]. In this code, the plasma is simulated as a number of macro-particles, each representing several real particles. The space is divided up into a grid of smaller cells on which the electromagnetic forces are calculated. At each discrete time step, the position of each macroparticle is used to calculate the forces on the grid, which in turn is used to update the particles velocities and their new positions. EPOCH also includes ionisation models, which take into account both tunnelling and barrier suppression ionisation pathways [109]. Collisional ionisation is a third pathway that is less important in the case of short-pulse laser ionisation; with a measured ionisation cross-section of hydrogen of $\sigma \approx 5 \times 10^{17}\,\mathrm{cm}^2$ [110] for non-relativistic electrons with quiver velocities $v_{\mathrm{osc}} = a_0 c \approx 0.5c$ (with $a_0 \approx 0.5$), the ionisation rate is approximately given by:

$$W = n_e \sigma v_{\mathrm{osc}} [\mathrm{s}^{-1}] \approx 0.72\,\mathrm{ps}^{-1}. \tag{6.2}$$

Hence I conclude that collisional ionisation is important over the scale of picoseconds rather than femtoseconds, as is the case for short-pulse laser ionisation. I therefore neglected this contribution in the simulations. The simulation parameters, which were chosen to be equal to the experimental parameters, are summarised in Table 6.1. Two different methods were used for estimating the temperature from these simulations.

In the first, which is a built-in temperature probe in EPOCH, the temperature is approximated as the standard deviation of the total momentum in each simulation cell i,

$$k_b T_i \approx \frac{\langle p^2 \rangle_i}{2m}. \tag{6.3}$$

The obtained temperature map, recorded after the laser pulse had passed through the plasma is shown in Figure 6.1. Averaging along the axis of laser propagation, I obtain the transverse temperature profile plotted in Figure 6.4 and find an average on-axis temperature of 2.75 eV.

The second way of approximating the temperature is by measuring the random (thermal) motion of the electrons, from which I obtain the thermal energy distribution $E_{\text{thermal}} = p^2_{\text{thermal}}/2m$. However, during the time that the drive laser spends in the plasma slab, there is a strong coherent quiver motion at the laser frequency. By filtering out this low-frequency component from the momentum $\vec{p} = \vec{p}_{\text{quiver}} + \vec{p}_{\text{thermal}}$, I am left with only the thermal component from which can estimate the thermal energy distribution. I then obtain the temperature by fitting using the Maxwell-Boltzmann distribution, using the temperature T as the fitting parameter:

$$f_E(E,T) = 2\sqrt{\frac{E}{\pi}}\left(\frac{1}{k_B T}\right)^{3/2} \exp\left(\frac{-E}{k_B T}\right). \tag{6.4}$$

The ionisation processes described above do not lead to a thermal distribution of electrons at the instance of ionisation. Over time however, the electrons will equilibrate to a thermal distribution through collisions. I found that the simulation results could be well characterised as a sum of two electron populations with different temperatures T_1

and T_2, with a total distribution given by:

$$f_E(E, T_1, T_2) = f_{E,1}(E, T_1) + f_{E,2}(E, T_2). \tag{6.5}$$

Figure 6.3 shows the obtained energy distribution together with the two electron populations of $T_1 = 0.26$ eV and $T_2 = 1.54$ eV. The transverse average of the higher of these is compared to the EPOCH temperature in Figure 6.4. These two electron populations will equilibrate through Coulomb collisions, which leads to a thermal distribution after a short time. The equilibration process may be described by [98]:

$$\frac{dT_\alpha}{dt} = \sum_\beta \bar{\nu}_\epsilon^{\alpha\backslash\beta} \left(T_\beta - T_\alpha \right), \tag{6.6}$$

where the Spitzer collision frequency is given by:

$$\bar{\nu}_\epsilon^{\alpha\backslash\beta} = 1.8 \times 10^{-19} \frac{\left(m_\alpha m_\beta \right)^{1/2} Z_\alpha^2 Z_\beta^2 n_\beta \ln \lambda}{\left(m_\alpha T_\beta + m_\beta T_\alpha \right)^{3/2}} \mathrm{s}^{-1}. \tag{6.7}$$

For electron-electron equilibration I have that $m_{\alpha,\beta} = m_e$, $Z_\alpha = Z_\beta = 1$. I found that the populations were approximately equal in size, thus $n_\alpha = n_\beta = 0.5 n_e$. The Coulomb logarithm for these parameters is $\ln \lambda \approx 13.7$ (using Equation (5.21)). I define an equilibration time as [98]

$$\tau_\epsilon^{\alpha/\beta} \equiv \frac{1}{\bar{\nu}_\epsilon^{\alpha\backslash\beta}} \approx 1.7 \times 10^5 \frac{\left(T_\alpha[\mathrm{eV}] + T_\beta[\mathrm{eV}] \right)^{\frac{3}{2}}}{n_\beta \, [\mathrm{cm}^{-3}] \ln \lambda} \mathrm{s} \approx 0.1 \, \mathrm{ps}. \tag{6.8}$$

With the low temperatures obtained in the simulation, one sees that $\tau \ll 1$ ps. The two different plasma electron will also isotropize on a similar timescale [111], and will therefore be fully thermalised on a time scale much shorter than the picosecond timescale relevant for the wakefield decay processes discussed in this thesis.

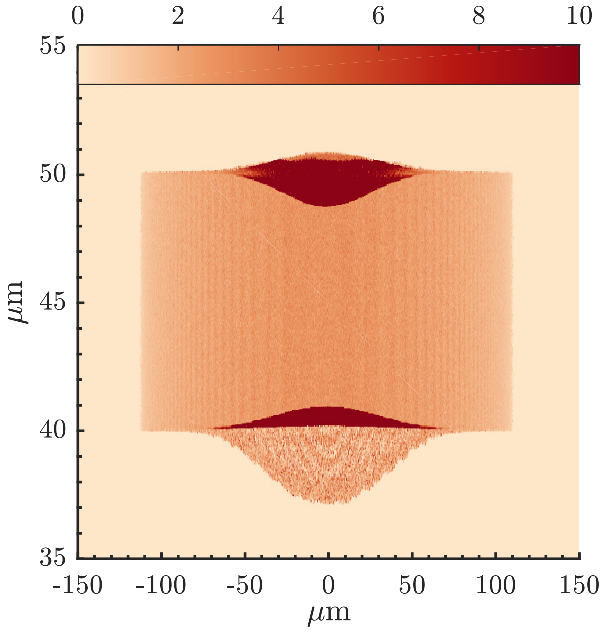

Figure 6.1: The two-dimensional temperature distribution after the passage of the ionising pulse, as calculated by the temperature probe built into EPOCH (colour scale in eV).

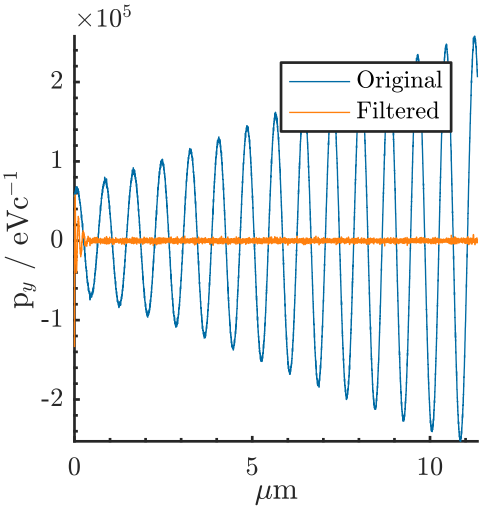

Figure 6.2: The transverse momentum p_y before and after filtering out low-frequency quiver motion to obtain the thermal fluctuations.

6.1.2 Wakefield decay simulations

2D PIC simulations were also performed by group member Alexander v. Boetticher to study the decay of the laser-driven linear wakefields using the same design parameters as the experimental study. The simulations were done using the relativistic PIC code

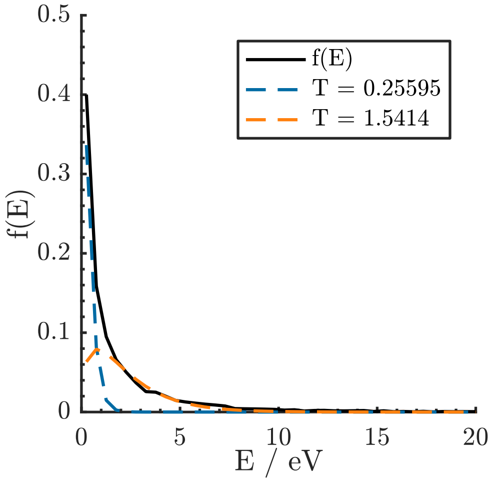

Figure 6.3: Plasma electron energy. The distribution is modelled using a sum of two Maxwell-Boltzmann distributions.

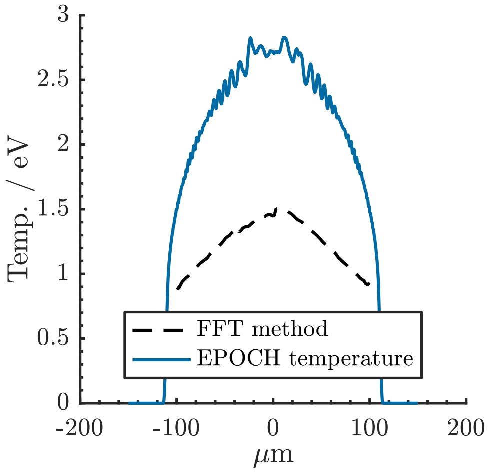

Figure 6.4: Transverse temperature distributions using the two different methods.

smilei [112], using cartesian coordinates. The simulations had a longitudinal (along the laser axis of projection) spatial resolution $\Delta x = 1\lambda_D$, and transverse spatial resolution of $\Delta y = 5\lambda_D$, where λ_D is the Debye length. It used 64 particles per cell and an extent of $8\lambda_D$ in the longitudinal direction and 160 μm in the transverse direction. The wakefield amplitude was measured by performing a Fourier transform of the density perturbation $\delta n_e = n_e - n_i$ along the laser propagation axis and identifying the highest amplitude peak. By performing this measurement at regular timepoints the temporal evolution of the wakefield was obtained, which I used to compare with the experimentally obtained amplitudes. A convergence scan was performed over the non-physical parameters (particles per cell, grid resolution), in order to ensure that artifacts due to these parameters did not influence the simulation.

6.2 Wakefield decay experimental design

The experiment was conducted during an 8-week campaign using the Astra Gemini TA3 laser at the Central Laser Facility (CLF), part of the Rutherford Appleton Laboratory, UK. The experiment was set up to measure the temporal evolution of laser-driven linear plasma wakes, comparing two plasma species with different ion masses, but identical charge: hydrogen and deuterium. The plasma wakes were measured using the TESS and FDH techniques discussed earlier. The experimental parameters are summarised in Table 6.2.

Table 6.2: Experimental parameters.

Parameter	Symbol	Value	Units
Plasma species	-	H & D	-
Target	-	Gas cell	-
Cell length	L	4	mm
Plasma density	n_e	9.7×10^{17}	cm^{-3}
Wavelength (drive)	λ_{drive}	800	nm
Pulse energy (drive)	E	1.68 ± 0.06	J
Pulse duration (drive)	τ_{drive}	48.9 ± 6.3	fs
Spot radius ($1/e^2$)	w_0	52.3 ± 0.8	μm
Intensity at focus	I_{max}	6.5×10^{17}	Wcm^{-2}
Normalised momentum	a_0	0.54 ± 0.18	-
Wavelength (probe)	λ_{probe}	400	nm
Pulse duration (probe)	τ_{probe}	1.35	ps

6.2.1 Experiment layout

The Astra Gemini TA3 laser consists of two separately amplified and compressed beams originating from the same oscillator, ensuring temporal synchronicity between the beams. The initial amplification stages provides 1.5 J pulses at 10 Hz stretched to 0.53 ns FWHM. Half of these pulses (5 Hz) are compressed and provided to users in TA2, while the other half (5 Hz) are further stretched to 1.06 ns before they are transported to the Gemini laser area. They are then split into two beams, called “North” and “South”, where each is amplified to a maximum of 15 J and compressed to 45 fs measured as the full width at half the maximum (FWHM) before they are delivered to TA3. A delay stage located in the South beam allows the relative timings between the two beams to be adjusted to allow for temporal overlap at the interaction point (IP).

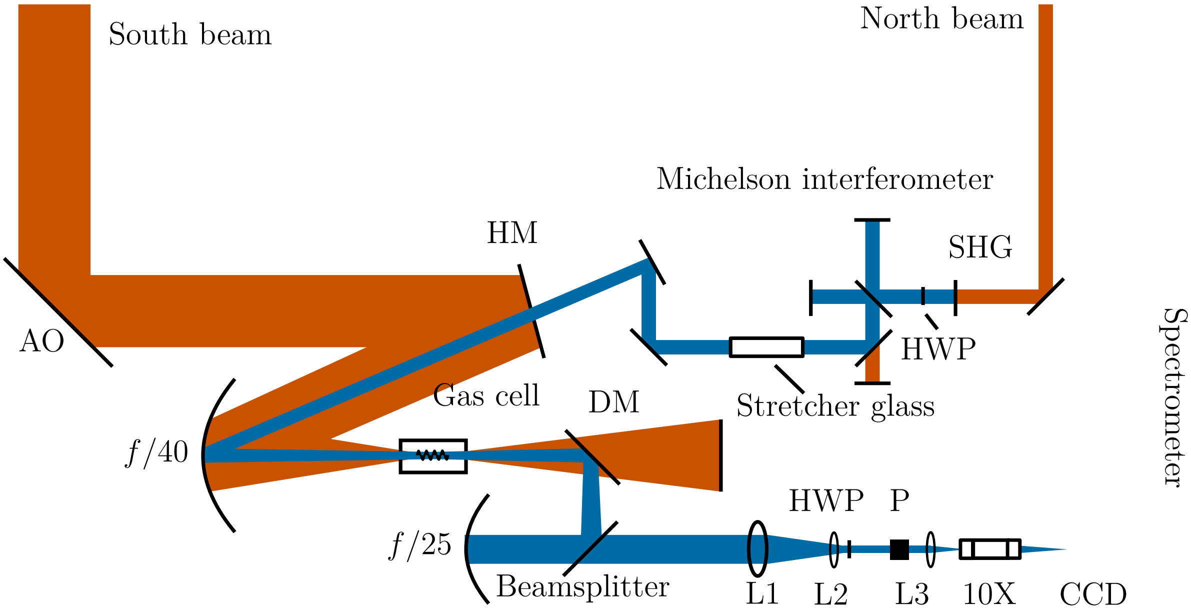

Figure 6.5: Simplified layout of the experiment. AO — adaptive optic, HM — holed mirror, SHG — second harmonic generating crystal, HWP — half wave plate, DM — dichroic mirror, L — lenses, CCD — charged coupled device.

The experiment layout is shown in Figure 6.5 and is described as follows: the Astra Gemini South beam, with centre wavelength 800 nm, temporal duration (FWHM) 45 fs, and energy at focus 1.68 J, was used as the drive beam. It was focused onto a gas cell (Figure 6.6) mounted on a 5-axis stage and pressurised to between 10-40 mbar of either hydrogen or deuterium. The laser was coupled into and out of the gas cell through a pair of coaxial pinholes mounted at each end of the cell. The pinholes used were 3D printer nozzles with a pinhole diameter

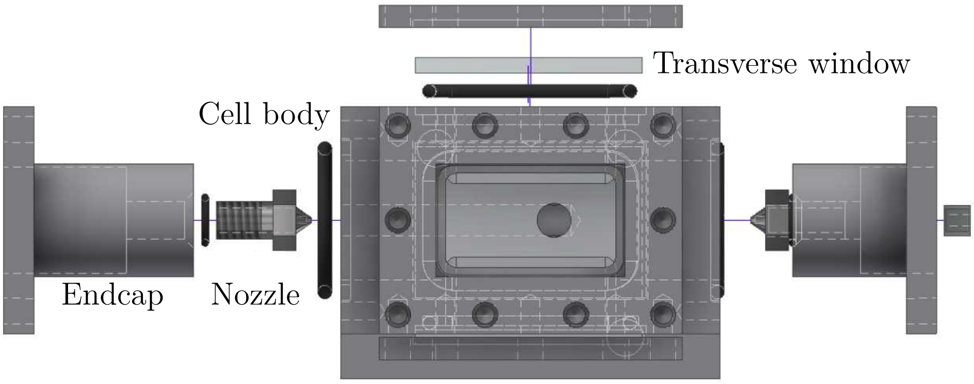

Figure 6.6: CAD drawing showing an exploded view of the design of the gas cell.

of 400 µm. A spot size of $w_0 = (52.3 \pm 0.8)\,\mu\text{m}$ (defined as the radius over which the intensity falls by a factor $1/e^2$ from its peak value) was achieved using a $6''$ diameter, 6.096 m focal length (f/40) spherical mirror. A camera fitted with a 10X magnifying objective was used to locate and image the drive beam focus so that the gas cell could be centred around it. An adaptive optic (AO) was used together with a wavefront sensor that imaged the focus in order to correct for any wavefront aberrations.

The second Gemini beam (North beam), was used as the probe beam to diagnose the wakefield using the FDH diagnostic described in Section 5.2.2.3. To generate the probe-reference pair, the North beam was apertured by a serrated aperture in the laser area to 15 mm diameter and propagated through a type I second harmonic generating crystal (600 µm thick Beta Barium Borate). This has a high nonlinear index to maximise the amount of frequency doubled (400 nm) light. Remaining 800 nm light was dumped by $> 99\%$ transmitting dichroic mirrors at 800 nm (and $> 99\%$ reflecting at 400 nm). The beam was then split in the two arms of a Michelson interferometer (shown in Figure 6.5), with a variable path difference between the mirrors. The path difference was used to set the time delay between the probe and reference, and was fixed to 6 ps in the experiment. The probe-reference subsequently propagated through a stretcher block (160 mm BK7) to stretch the pulses to about 1.4 ps (as described in

Section 6.2.3). They were then injected onto the drive beam axis through the back of a holed mirror (HM in Figure 6.5) with a 1″ hole cut through its centre. The probe beam was focused through the gas cell using the same f/40 spherical mirror. A spherical mirror ($f = 2.54\,\mathrm{m}$ focal length) was used as an f/25 to collect the transmitted light from the back of the gas cell. A half wave plate and linear polariser setup was used to filter out any plasma-originating blue light generated by the drive beam [103, 113] (the plasma-generated blue light has the same linear polarisation as the drive beam and is perpendicular to the probe beam polarisation). A set of mirrors and lenses was used to transport the beam and image the centre of the cell onto the entrance slit of an imaging spectrometer (Acton SP2 − 750), which projected the probe beam spectrum onto a CCD camera (Andor Newton). In the following two sections, I will describe the drive and probe beam characterisations that were carried out alongside the experimental measurements. In the first, Section 6.2.2, I describe the focal scan analysis that was done to establish the position of the focus along the laser axis, using the D4σ method to measure the focal spot. In Section 6.2.3 I describe a method for measuring the spectral phase, including the GDD, of the probe and reference pulses.

6.2.2 Focal scan analysis

To obtain a value for the parameter a_0 and the beam spot size used in the experiment, I performed a focal scan by capturing images of the beam over a 15 mm range using a $10X$ imaging microscope together with a CCD camera mounted on a motorised translation stage. The imaging position relative to focus could be varied by adjusting a motorised linear translation stage, located inside the vacuum chamber. At each stage position, three images were taken and analysed, using the D4σ method [114]. The beam width is then defined as four times the standard deviation of the beam intensity:

$$D4\sigma = 4\sqrt{\frac{\int_{-\infty}^{\infty}\int_{-\infty}^{\infty} I(x,y)(x-\bar{x})^2 dxdy}{\int_{-\infty}^{\infty}\int_{-\infty}^{\infty} I(x,y) dxdy}}, \tag{6.9}$$

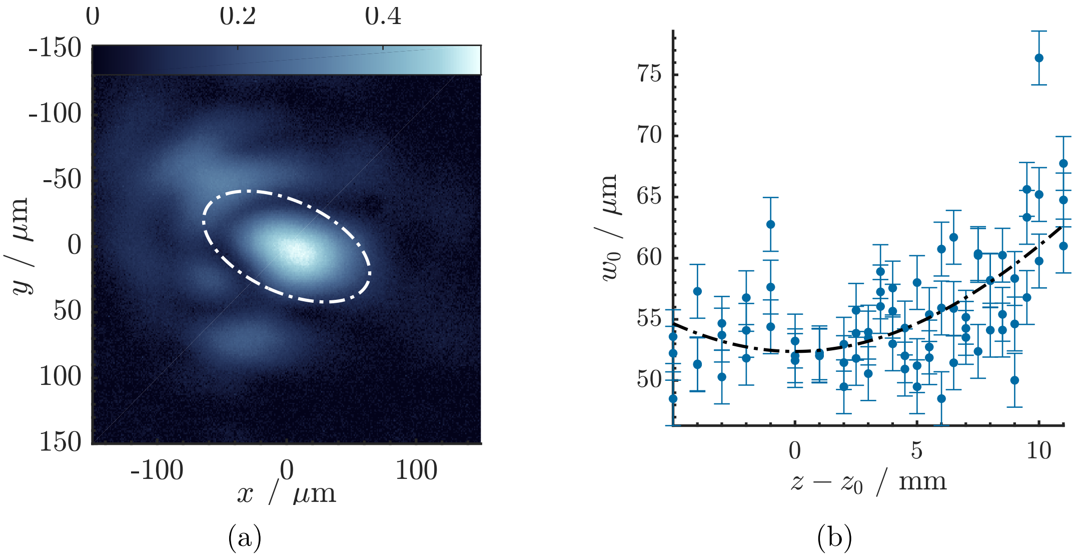

Figure 6.7: (a) Plot of the drive beam a_0 values at the focal position. The white ellipse shows a fit of the focal spot using the D4σ method. (b) Average beam size w_0 at different z-positions. The error bars correspond to the camera resolution of 2.2 µm, and the black line shows the fit to the measured data.

and the beam centroid $\bar{x}$ is calculated as:

$$\bar{x} = \frac{\int_{-\infty}^{\infty}\int_{-\infty}^{\infty} I(x,y)x dx dy}{\int_{-\infty}^{\infty}\int_{-\infty}^{\infty} I(x,y) dx dy}. \tag{6.10}$$

Figure 6.7 shows the average beam radius of each shot as a function of the position along the beam axis at which the shot was taken, together with a fit of the function:

$$w(z) = w_0\sqrt{1+\left(\frac{z-z_0}{z_R}\right)^2}, \tag{6.11}$$

where z_R is the Rayleigh range $z_R = \pi w_0^2/\lambda$, w_0 the beam spot at focus, and λ the laser wavelength. Using this fit, I identified the focus position z_0 as well as the focal spot w_0. Together with the measured pulse energy and duration from Table 6.2, I then calculated the normalised momentum a_0 of the drive laser at focus. This was done by multiplying the value of each pixel with the beam intensity divided by the total pixel count in the image. This gives the beam intensity $I(i,j)$ measured at each pixel (i,j), from which I calculated a_0 as:

$$a_0(i,j) \approx 0.85\sqrt{I(i,j)[10^{18}\,\mathrm{W\,cm^{-2}}](\lambda[\mu\mathrm{m}])^2}. \tag{6.12}$$

6.2.3 Measuring the spectral phase

The FDH method relies on stretching the probe pulse in time by adding group delay dispersion (GDD). In the spectral phase of a light pulse, the GDD is the second order coefficient $\varphi^{(2)}$ of the Taylor series expansion around $(\omega-\omega_0)$:

$$\varphi(\omega) \approx \varphi^{(0)} + \varphi^{(1)}(\omega-\omega_0) + \frac{1}{2}\varphi^{(2)}(\omega-\omega_0)^2 + \frac{1}{6}\varphi^{(3)}(\omega-\omega_0)^3. \tag{6.13}$$

The difference in delay between the different wavelength components after propagation through the dispersive medium causes the pulse to stretch out in time. In the case of Gaussian pulses, the FWHM pulse duration τ_out after a pulse with FWHM duration τ_in has propagated through a dispersive medium can be estimated by (assuming $\varphi^{(3)}=0$) [115]

$$\frac{\tau_\mathrm{out}}{\tau_\mathrm{in}} = \left(1 + \frac{(\varphi^{(2)})^2}{4\beta^2}\right)^{1/2} \tag{6.14}$$

$$\beta = \tau_\mathrm{in}^2/(8\ln 2). \tag{6.15}$$

For a dispersive material with a given group velocity dispersion (GVD), the GDD can be obtained from the GVD times the propagation length in the media:

$$\varphi^{(2)} = \mathrm{GVD}\times L. \tag{6.16}$$

The calculated value of the GDD accumulated by propagation through a 160 mm long BK7 block with a group velocity dispersion (GVD) of 124.49 $\mathrm{fs^2\,mm^{-1}}$ [116] was found to be approximately $\varphi^{(2)} \approx 19\,918\,\mathrm{fs}^2$. Here I present the method used to measure the group delay dispersion (GDD), $\varphi^{(2)}$, and the third order spectral phase, $\varphi^{(3)}$, of the probe and reference pulses. The method consists of overlapping one of the probe or reference pulse with the much shorter drive pulse in the gas-filled cell, which causes an ionisation blowout feature in the 400 nm spectrum due to the high gradient refractive index. This feature is observed as a significant loss of intensity at the corresponding frequency in the probe spectra (since the probe and reference pulses are significantly stretched, the different frequency components occur at different times ζ in the pulses). By changing the time delay between the drive and probe pulses, the blowout feature is tracked as it moves across the probe spectrum, providing a mapping between time ζ and frequency $\omega(\zeta)$. This is shown in Figure 6.8. By definition, the instantaneous frequency is the first derivative of the temporal phase with respect to time:

$$\omega(\zeta) = \frac{d\phi(\zeta)}{d\zeta}. \tag{6.17}$$

In Section 5.2.3 one saw that the temporal phase and the spectral phase are related by a Fourier transform. Let the electric field in the frequency domain be $\mathcal{E}(\omega)$ and in the temporal domain $E(\zeta)$:

$$\mathcal{E}(\omega) = |\mathcal{E}(\omega)| \exp\left(i\varphi(\omega)\right) \tag{6.18}$$

$$E(\zeta) = |E(\zeta)| \exp\left(i\phi(\zeta)\right), \tag{6.19}$$

with the spectral phase $\varphi(\omega)$ and temporal phase $\phi(\zeta)$, which I can obtain from the complex argument of the electric fields:

$$\varphi(\omega) = \arg[E(\omega)] \approx \varphi^{(0)} + \varphi^{(1)}(\omega - \omega_0) + \frac{1}{2}\varphi^{(2)}(\omega - \omega_0)^2 + \frac{1}{6}\varphi^{(3)}(\omega - \omega_0^3) \tag{6.20}$$

$$\phi(\zeta) = \arg[E(\zeta)], \tag{6.21}$$

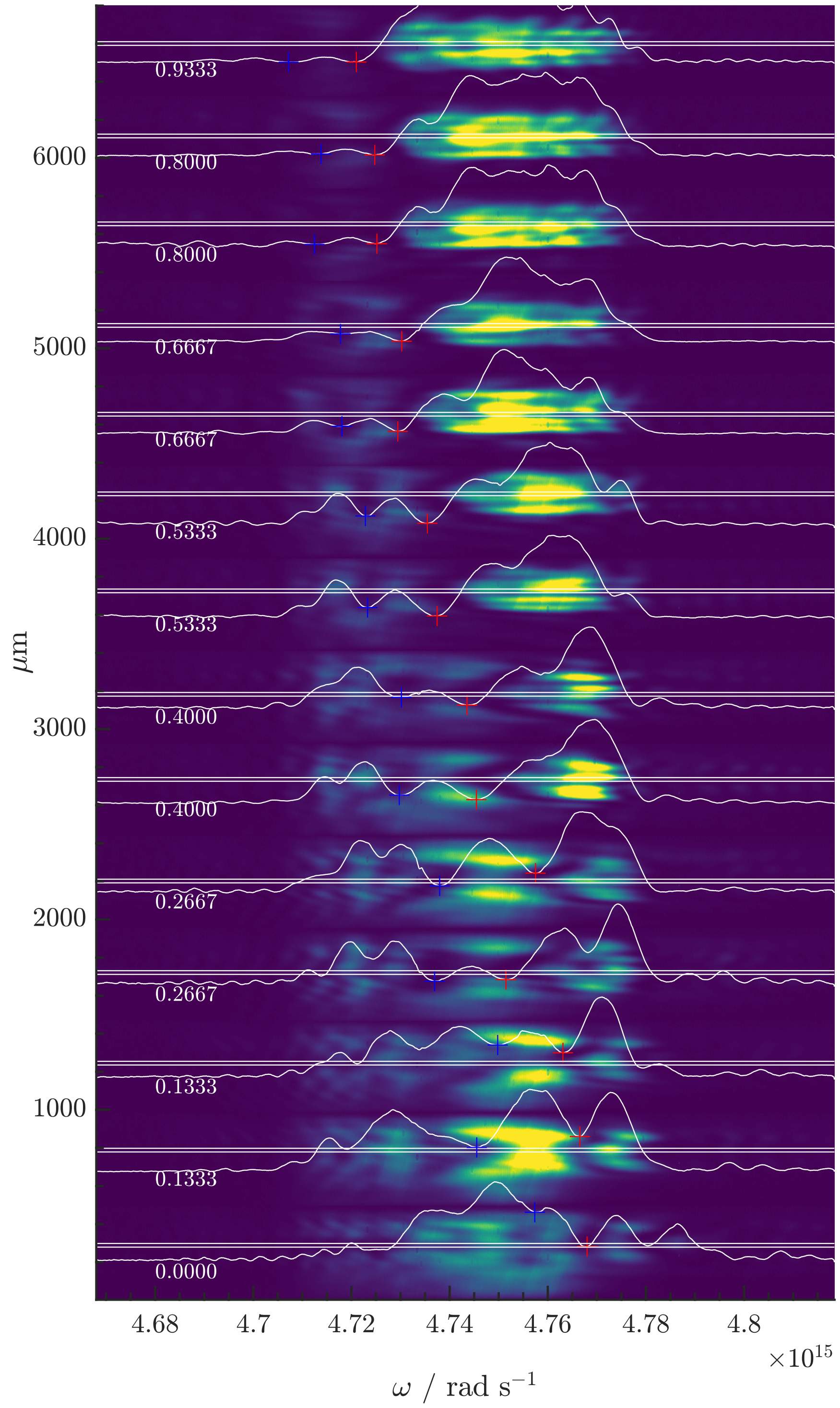

Figure 6.8: The ionisation blowout feature in the blowout spectrum for a series of 14 shots in top-to-bottom order of decreasing delay between the drive and probe pulses (the delay in units of ps is shown in white text next to each spectrum). The white lineouts show the transverse average between the parallel horizontal lines in the centre of each spectrum, and the red cross marks the tracked blowout feature.

where I assumed that the spectral phase can be expanded up to a polynomial of third order. The temporal and frequency representations of the electric field are related through the Fourier transforms:

$$\mathcal{E}(\omega) = \frac{1}{\sqrt{2\pi}} \int_{-\infty}^{\infty} E(\zeta) \exp(-i\omega\zeta) \mathrm{d}\zeta \tag{6.22}$$

$$E(\zeta) = \frac{1}{\sqrt{2\pi}} \int_{-\infty}^{\infty} \mathcal{E}(\omega) \exp(\mathrm{i}\omega\zeta) \mathrm{d}\zeta. \tag{6.23}$$

Using the ionisation blowout measurement in Figure 6.8 I obtain for each temporal delay coordinate ζ the corresponding $\omega(\zeta)$ from the blowout in the spectrum. A measurement of the unperturbed spectrum $|\mathcal{E}(\omega)|$ (i.e. taken without drive beam or plasma) is shown in Figure 6.9a, and the forward Fourier-transformed spectrum shows the pulse shape in the temporal domain in Figure 6.9b. I now have enough information to estimate the spectral phase $\varphi(\omega)$. The process can be described as follows.

1. Assume a spectral phase $\varphi'(\omega)$ up to third order, of the form in Equation 6.20
2. Calculate the Fourier transform of $\mathcal{E}(\omega) = |\mathcal{E}(\omega)| \exp(i\varphi'(\omega))$ using Equation 6.23 to obtain the temporal representation of the electric field $E(\zeta)$, as shown in Figure 6.9b (this figure shows the final obtained phase)
3. Use Equation (6.21) to obtain the temporal phase and calculate its temporal derivative
$$\frac{d\phi(\zeta)}{d\zeta} = \frac{d}{d\zeta}\arg[E(\zeta)].$$
4. Vary the guess $\varphi'(\omega)$, repeating steps 1 - 3, to obtain the spectral phase that minimises

$$\varphi^{\min}(\zeta) = \arg\min \sum \left(\left| \omega(\zeta) - \frac{d\phi(\zeta)}{d\zeta} \right|^2 \right). \tag{6.24}$$

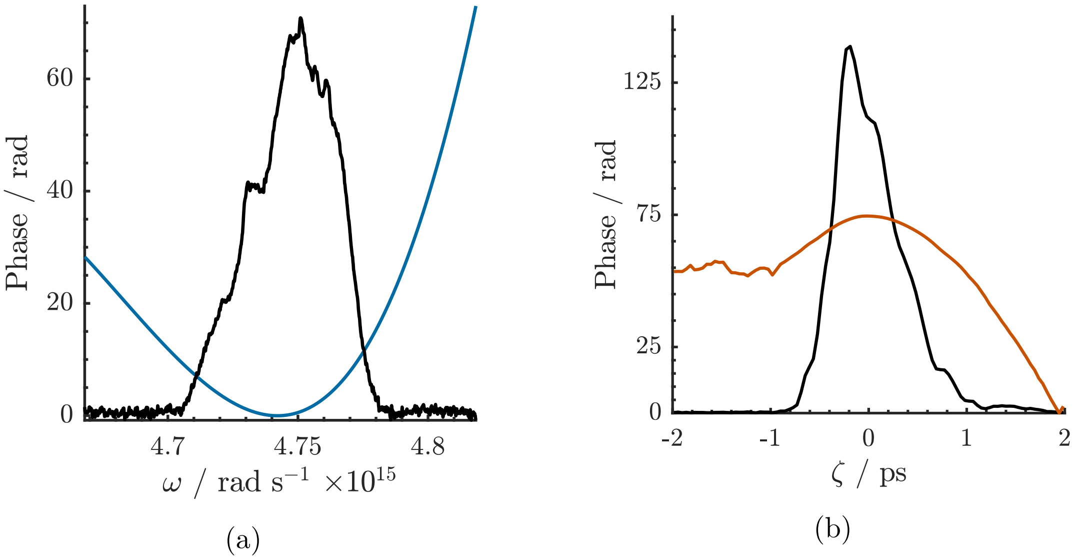

Figure 6.9: Electric field amplitude (black lines) and phase (blue lines) in the (a) spectral domain and (b) temporal domain. The spectral amplitude in (a) can be measured directly, while the spectral phase can be obtained using the procedure described in this section. The temporal amplitude and phase in (b) are obtained by Fourier-transforming the spectral amplitude and phase.

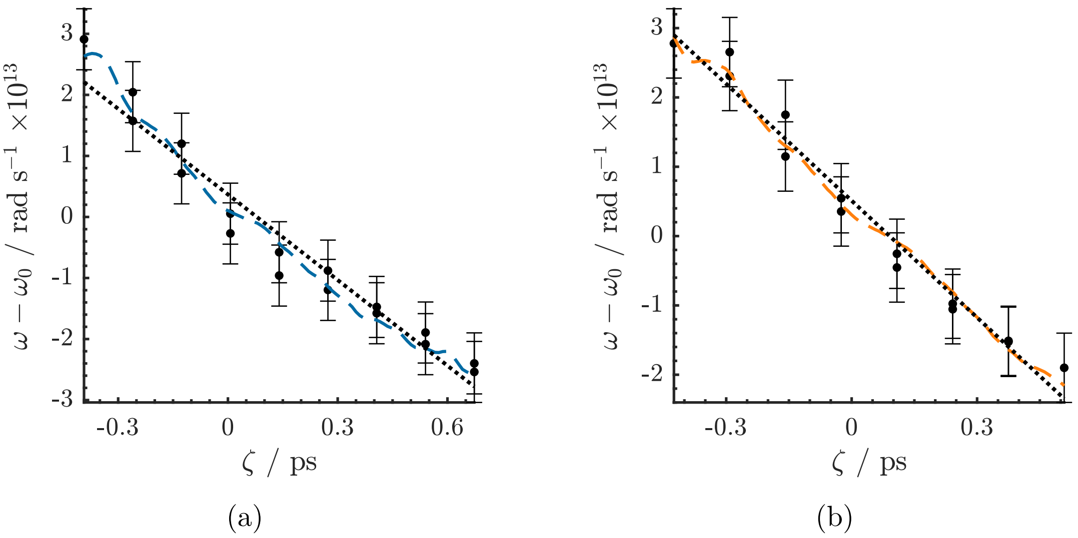

Figure 6.10: Measurement of the GDD of the (a) probe and (b) reference pulses. The black dots indicate the location of the ionisation front feature in time and frequency. The error bars indicate the estimated uncertainty in locating the intensity minima, from Figure 6.8. The dashed lines show the fitted first derivative of the temporal phase $d\phi(\zeta)/d\zeta$ of each pulse. The dotted lines show a linear fit to the data.

The benefit of this procedure is that it allows the measurement of the spectral phase up to third order. This is required in analysis methods such as FDH which require knowledge of the full spectral phase of the probe and reference pulses, as I showed in Section 5.2.4. I performed this measurement for the probe and reference pulses individually. Shown in Figure 6.10 are the measured frequency mappings $\omega(\zeta) - \omega_0$, where ω_0 is the central frequency of the pulses, and $\omega(\zeta)$ the frequency measured using the blowout method. This is compared with the first derivative of the temporal phase $d\phi^{\mathrm{min}}(\zeta)/d\zeta$ deduced from the fitted spectral phase $\varphi(\omega)$, obtained from Equation 6.24. The obtained components of the probe and reference spectral phases are summarised in Table 6.3. The errors were estimated using a non-linear least squares fitting procedure [117] (see appendix B). I also compared this method to a previous method to estimate the GDD, where the third order spectral phase terms are assumed to be negligible. In this case, it can be shown that the second order spectral phase is approximately equal to the inverse of the second order temporal phase [105],

$$\varphi^{(2)} \approx \frac{1}{\phi^{(2)}}, \tag{6.25}$$

which in turn is estimated using the derivative of the instantaneous frequency:

$$\phi^{(2)} \approx \frac{d\omega(\zeta)}{d\zeta}, \tag{6.26}$$

where $\omega(\zeta)$ is measured using the same blowout technique as above. This means I am able to find the GDD by performing a linear fit to the location of the blowout feature as a function of time, as shown in Figure 6.10. Using this technique, I obtained the following values of the GDD for the probe: $\varphi^{(2)} = (23\,000 \pm 1400)\,\mathrm{fs}^2$ and reference pulses: $\varphi^{(2)} = (18\,000 \pm 1000)\,\mathrm{fs}^2$ (the errors were calculated from the fit to the data, as explained in Appendix B). These are close, but not identical to, the values obtained using the method described above. This is likely due to the fact it does not take into account the non-zero third order phase term $\varphi^3(\omega)$ that was observed in the phase.

Table 6.3: Spectral phase components obtained using the spectral blowout technique.

Pulse	$\varphi^2(\omega)$	$\varphi^3(\omega)$
Probe	$(18\,600 \pm 790)\,\mathrm{fs}^2$	$(-4.0 \pm 1.0) \times 10^5\,\mathrm{fs}^3$
Reference	$(17\,592 \pm 800)\,\mathrm{fs}^2$	$(-2.0 \pm 1.0) \times 10^5\,\mathrm{fs}^3$

6.3 Temporally encoded spectral shifting analysis

In the following section I describe how to obtain the wakefield amplitude, $\delta n_e/n_0$, using the TESS analysis method on data obtained from an FDH diagnostic. For a detailed description of the theory behind TESS and FDH I refer the reader to Section 5.2.3.

In FDH, a spectral interferogram is generated from recording light incident on the vertical slit of an imaging spectrometer using a CCD camera (see Figure 6.11). The vertical axis corresponds to a spatial dimension, and the horizontal axis to wavelengths. We perform a one-dimensional inverse Fourier transform (FT) along the spectral axis to transform the interferogram into the temporal domain. The FT is symmetric around zero, however the "negative time" components can be discarded as they are identical to those at positive time. I also cut the data vertically to remove the camera pixels which were not exposed to light. Three reference shots were taken for each data run, without any gas in the cell, in order to remove from the FT any background. The shots were

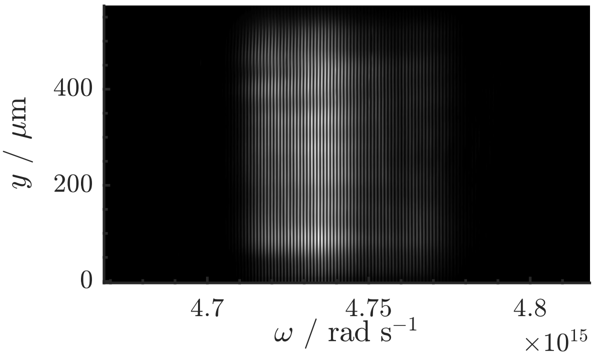

Figure 6.11: Recording of a wakefield in a spectral interferogram. The fringes are caused by the 6 ps delay between the probe and reference pulses. The presence of a wakefield causes a modulation of the spectral fringes, which can only be seen by performing an inverse Fourier transform of the data.

aligned spatially by using the vertical edges of the measured spectras to account for spatial jitter of the probe beam and normalised to their integrated intensity to account for shot-to-shot variation in the probe beam fluence, before the average of them was subtracted from the FT. The result of this background removal procedure is shown in Figure 6.12, where the TESS peaks are visible in Figure 6.12b. In order to identify the TESS satellites we perform a filter operation on the FT using a Gaussian kernel to remove highly localised noise which could be incorrectly identified as a peak. Peaks are subsequently located within a region based on the expected separation from the sideband. The region was selected so that TESS peaks could lie within ±0.15 ps from the expected separation, in order to avoid wrongly identifying noise, or the sideband, as TESS peaks. It also had a vertical extent of ±70 µm around the centre of of the FT, as most of the TESS peaks were found to lie within this range. After obtaining the positions of the TESS peaks in the FT, any residual background was removed by first fitting a two-dimensional quadratic polynomial to a background region, shown in Figure 6.13. The quadratic polynomial was then subtracted from the peak region. Finally, a 2D Gaussian function was fitted to the identified peak, as shown in Figure 6.14. In order

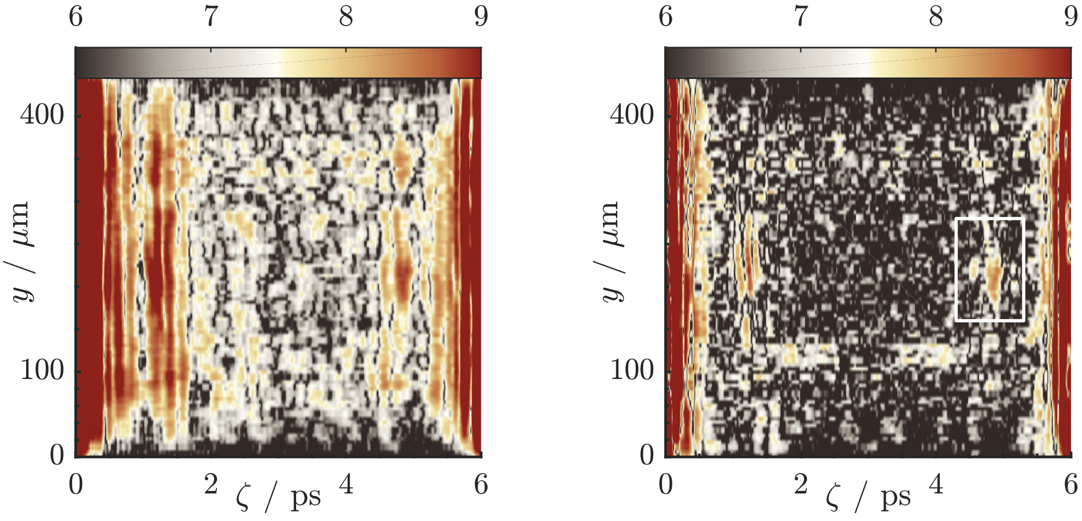

(a)

(b)

Figure 6.12: Absolute value of the Fourier transform of the spectral interferogram, (a) before processing and (b) after subtracting reference shot (colour scale is logarithmic).

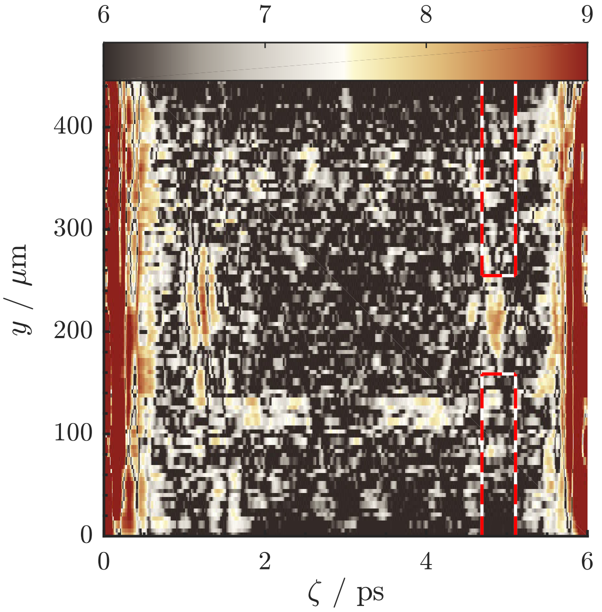

Figure 6.13: A quadratic function is fitted to the background regions enclosed by the white lines and subtracted from the peak in the centre.

to obtain the sideband height at the same vertical position as the TESS peak, I fitted a Gaussian to each of five lineouts centred on the TESS peak, and take the average of these as the sideband height. The ratio of the Gaussian peak to the sideband height, r, was then used to obtain the wakefield amplitude. To extract the wakefield amplitude I

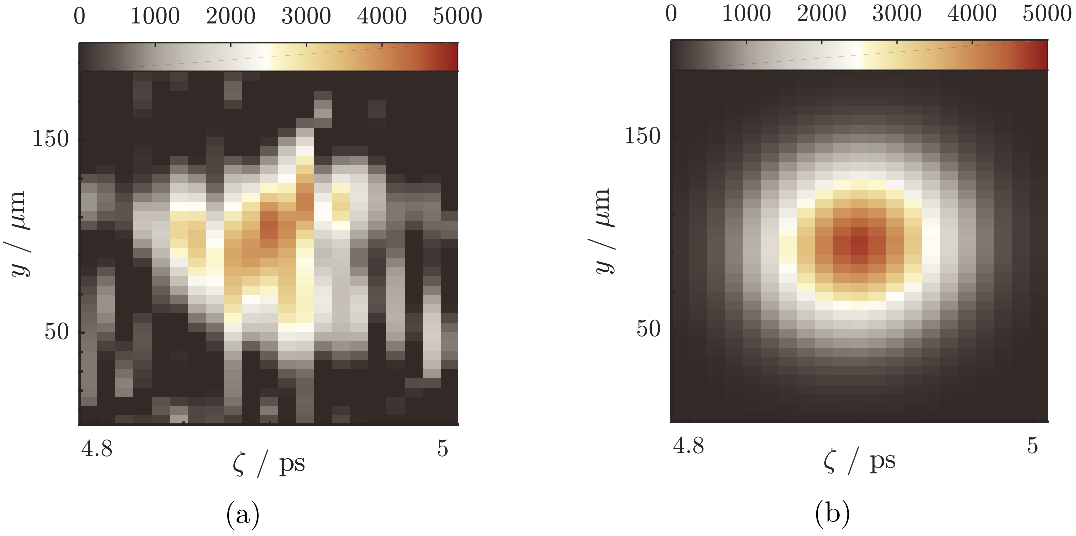

(a)

(b)

Figure 6.14: (a) Peak after quadratic background subtraction, (b) Gaussian 2D fit to the peak. The height of the Gaussian fit was used as the peak height, and the radius at which the Gaussian falls to $(1/e^2)$ of its maxima was used as the transverse width of the peak.

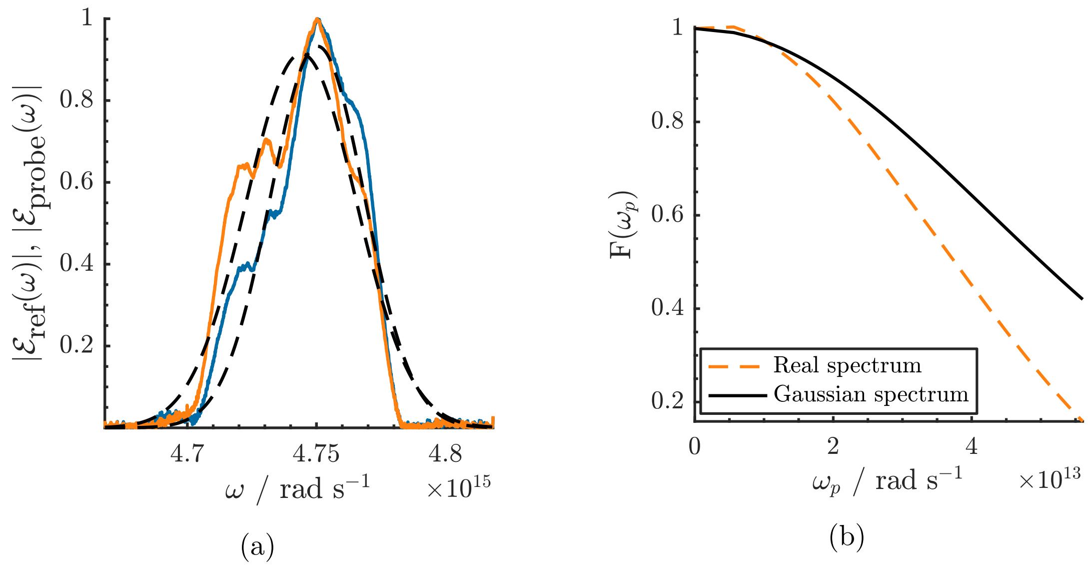

Figure 6.15: (a) Lineouts of the spectral intensities of the probe (red line) and reference pulses (blue line). The dashed lines show Gaussian fits to these spectra. (b) spectral overlap function $\mathcal{F}(\omega_p)$ as a function of the electron density, for the measured spectra and Gaussian spectra fitted to the measured spectra.

also need the spectral overlap factor, $\mathcal{F}(k\omega_p)$, which is calculated using equation (5.46), with $k = 1$:

$$\mathcal{F}(\omega_p) = \frac{\int_{-\infty}^{\infty} |\mathcal{E}_{\text{probe}}(\omega + \omega_p)||\mathcal{E}_{\text{ref}}(\omega)|d\omega}{\int_{-\infty}^{\infty} |\mathcal{E}_{\text{probe}}(\omega)||\mathcal{E}_{\text{ref}}(\omega)|d\omega}. \tag{6.27}$$

I used Equation (6.27) with the separately measured probe and reference pulses spectra averaged over their spatial axis. The measured spectra together with the spectral overlap as a function of plasma density are plotted in Figure 6.15. In Section 5.2.3, I showed that using the TESS method, the wakefield amplitude is calculated as:

$$\frac{\delta n_e}{n_{e0}} = \phi_0 \frac{4\pi}{\omega_p^2 \lambda L}, \tag{6.28}$$

where L is the plasma length and λ the probe wavelength. The phase amplitude ϕ_0 can be retrieved by solving the transcendental equation:

$$r = \frac{J_1(\phi_0)}{J_0(\phi_0)} \mathcal{F}(\omega_p). \tag{6.29}$$

In Equation (5.48), it was showed that if $\phi_0 \ll 1$, then $J_0(\phi_0) \approx 1$ and $J_{\pm 1}(\phi_0) \approx \phi_0/2$. One therefore obtains the phase amplitude ϕ_0 from

$$\phi_0 \approx \frac{2r}{\mathcal{F}(\omega_p)} \tag{6.30}$$

Together with the satellite-to-sideband ratio r, the spectral overlap factor $\mathcal{F}(\omega_p)$, and the measured plasma density (and hence, the plasma frequency ω_p), there is now sufficient information to calculate the wakefield amplitude $\delta n_e/n_{e0}$. In Section 6.3.1, I show to apply these steps to analyse a run in which the pressure is changed. I also compare these results to a theoretical prediction. Next, in Section 6.3.2, I apply the same analytic method to runs in which the temporal delay was changed between the probe and drive pulses, in order to measure the wakefield decay timescale.

6.3.1 Pressure scan analysis

Here I present the analysis of a pressure scan which was performed during the experiment by varying the backing pressure between $10 - 40$ mbar in hydrogen. For each shot, a one-pixel wide slice in the y-direction centred on the TESS peak, was selected and used to populate a waterfall plot with shots taken at different pressures. This plot is shown in Figure 6.16, and shows the TESS peaks moving away from the sideband with increasing pressure as expected from the relation $\tau = \varphi^{(2)}\omega_p$. I then measured the positions of the peaks relative to the sideband as a function of plasma density. I used this data to fit the expression $\tau = \varphi^{(2)}\omega_p$, using the GDD, $\varphi^{(2)}$, as the fitting parameter. This constitutes a different method to measure the GDD to the method presented in Section 6.2.3. First, I fitted directly to the data and obtained a GDD value of $\varphi^{(2)} = (15\,203 \pm 327)\,\mathrm{fs}^2$. However as can be seen in Figure 6.17, the fit was not very good and appeared to be offset from the data. The reason for this could be for example that the pressure reading was offset by a constant pressure, and that gas was leaking out from the system before the gas cell (the pressure gauge was located outside the vacuum chamber, a distance of 2 m from the cell)*. I therefore performed a second fit, where I allowed the pressure be modified by a constant offset and a scaling factor: $P \to \alpha P + P_0$. Using this method, I obtained $\alpha = 0.8$, $P_0 = 4\,\mathrm{mbar}$, and $\varphi^{(2)} = (19\,698 \pm 98)\,\mathrm{fs}^2$, which is shown in Figure 6.17. This is within 10% of the values of the GDD obtained using the spectral blowout technique in Section 6.2.3. I also compared the measured wakefield amplitude to that predicted from linear plasma theory. In Section 2.4, I showed an expression for the linear wakefield amplitude as a

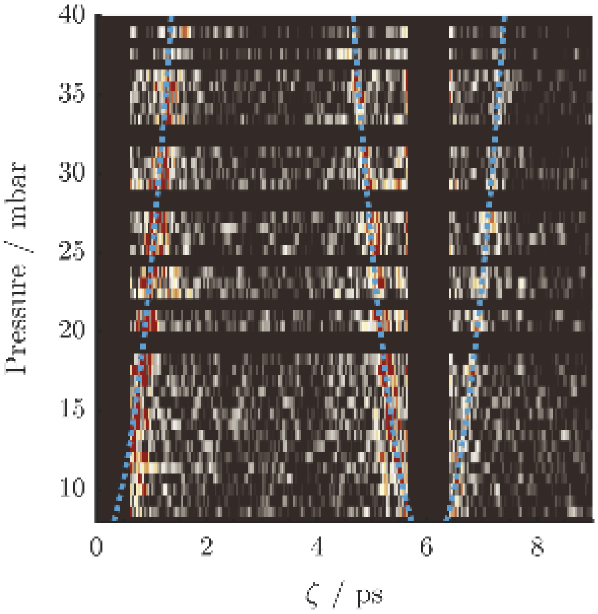

Figure 6.16: Waterfall plot showing lineouts of the absolute values of the Fourier transforms at different backing pressures. The white lines shows a fit to the expected offset, using the equation $\tau = \omega_p \varphi^{(2)}$.

---

*In later experiments, a second pressure gauge was used close to the gas cell in order to measure the drop in gas pressure.

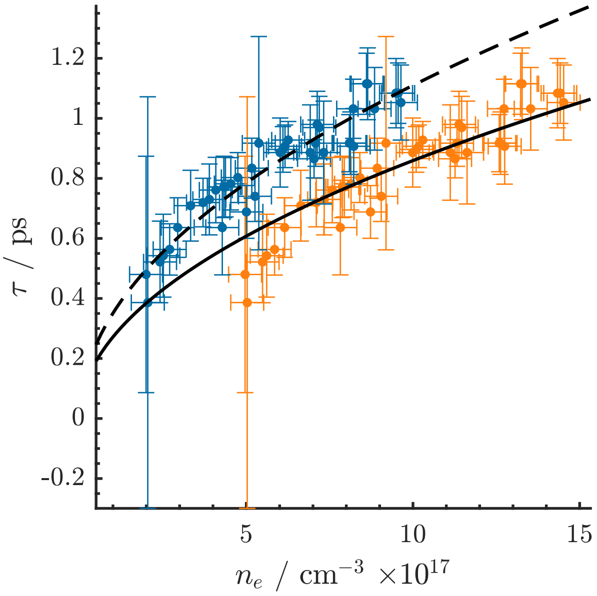

Figure 6.17: Plot showing a fit to the temporal separation τ between the sideband and the peaks on the right hand side of it. The red points show the temporal separations assuming that the measured cell pressure P_{meas} is correct, and the blue points are assuming that a correction of form $\alpha P_{\text{meas}} - P_0$ should be applied. The horizontal error bars correspond to the pressure resolution of 1 mbar of the pressure gauge, and the vertical bars show the estimated error of the TESS satellite location. The solid (dashed) line shows a fit to the red (blue) points of the form $\tau = \omega_p \varphi^{(2)}$.

function of the plasma frequency and the drive laser parameters:

$$\frac{\delta n_e}{n_0} = A \left[1 + \underbrace{\left(\frac{2c}{\omega_{pe}\sigma}\right)^2 \left(1 - \frac{r^2}{\sigma^2}\right)}_{\text{Radial wakefield}} \right] \exp\left(-\frac{r^2}{\sigma^2}\right) \sin\left(\omega_{pe}(t - z/c)\right), \tag{6.31}$$

$$A = \frac{I\sqrt{\pi}}{c^3 n_c m_e} \left(\frac{\omega_{pe}\tau_0}{2}\right) \exp\left[-\left(\frac{\omega_{pe}\tau_0}{2}\right)^2\right]. \tag{6.32}$$

Here, $n_c = \omega^2 \epsilon_0 m_e / e^2$ is the critical plasma density, ω the laser frequency, ϵ_0 the vacuum permittivity, and m_e the electron mass. Inserting the measured values of the laser intensity I at focus, the pulse duration τ_0, the beam spot size σ and the plasma frequency ω_p I calculated the predicted amplitude using Equation (6.32) (multiplied with n_0 to show the absolute rather than relative wakefield amplitude). The result is plotted alongside the experimental results in Figure 6.18.

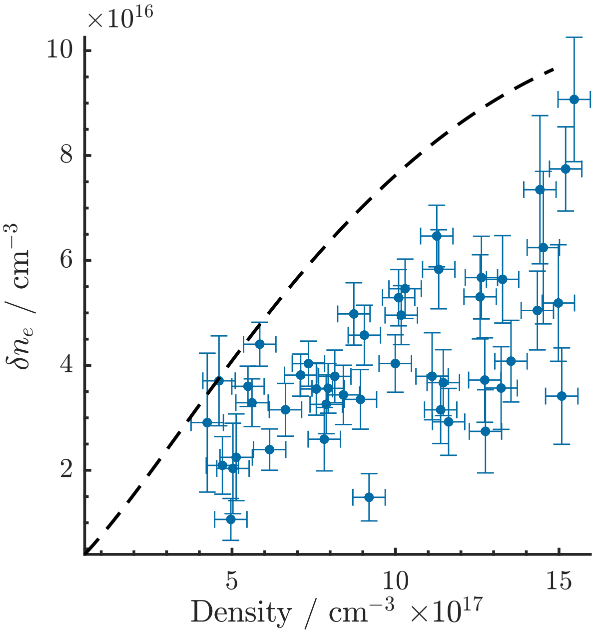

Figure 6.18: Plot showing the measured absolute wakefield amplitude δn_e as a function of plasma density n_e (blue points). The horizontal error bars correspond to the 1 mbar resolution of the pressure gauge, and the vertical error bars to the background noise of the interferogram FTs, as explained in Section 6.3.2. The black line shows the theoretical prediction (equation (6.32)) using the experimental parameters from Table 6.2.

6.3.2 Wakefield decay measurements

In order to measure the wakefield amplitude at different temporal delays after the initial wakefield excitation, a time delay stage located in the drive beam line was used to adjust the relative timing between the drive pulse and the probe pulse. At each timing position, ten shots were taken for each gas (hydrogen and deuterium) at a nominal pressure of 20 mbar and all other experimental conditions as summarised in Table 6.2. The wakefield decay measured over 4 ps (the maximum delay that could be measured due to the experimental constraints — any longer delay, and the drive would start overlapping with the reference pulse). The uncertainty in the wake amplitude measurement of each shot was determined using the standard deviation of the background segments shown in Figure 6.13. The deduced wakefield amplitude, and its associated error, is shown in Figure 6.19 for the case of hydrogen gas. From the fitted 2D Gaussian functions to the

TESS peaks I also defined a transverse width: the radius at which the height of the Gaussian falls to $(1/e^2)$ of its maximum. This was compared to the drive beam spot size w_0, and is shown in Figure 6.20a for hydrogen and 6.20b for deuterium.

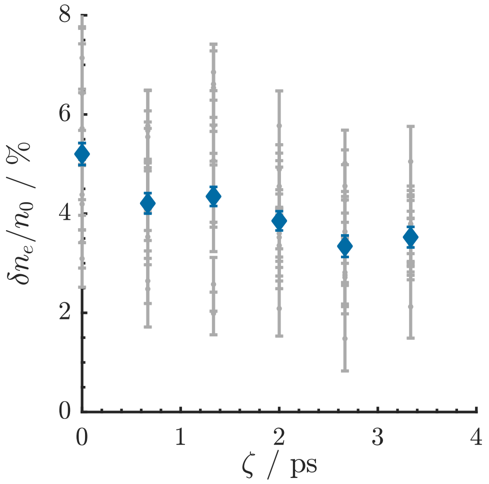

Figure 6.19: Plot showing the wakefield amplitude and uncertainty of each shot (gray lines) and the average amplitude (blue diamonds) and error of the mean (blue lines) at each temporal delay.

In order to characterise the decay time of the wakefield I performed a nonlinear fit to the measured wakefield amplitude at different temporal delays, using a function of the form $y = A\exp(-\zeta/\tau)$, where τ is the lifetime. See appendix B for more details on how to perform such a non-linear fit. The result is shown in Figure 6.21a for hydrogen and in Figure 6.21b for deuterium. I also performed the same analysis assuming that the measured pressure P_{meas} did not correspond to the actual cell pressure, and had to be corrected by $\alpha P_{\text{meas}} - P_0$, according to the pressure scan analysis presented in Section 6.3.1 where I found $\alpha = 0.8$ and $P_0 = 4\,\text{mbar}$. The resulting τ_{wf}, in units of the number of plasma periods $(2\pi\omega_p^{-1})$ obtained from this analysis are summarised in Table 6.4.

The obtained experimental results were also compared with those obtained from 2D PIC simulations, described in Section 6.1.2.

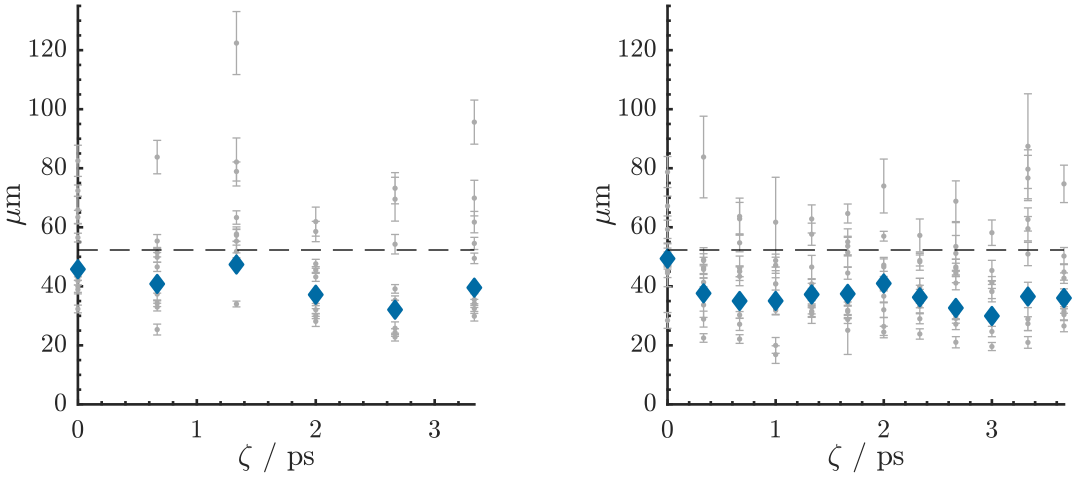

(a) (b)

Figure 6.20: The measured ($1/e^2$) radial extent of the plasma wakefields for (a) hydrogen and (b) deuterium. The gray dots and vertical lines represent the spatial width and uncertainty of the fitted Gaussian functions to the TESS satellites, as shown in Figure 6.14b. The blue diamonds show the average at each temporal delay, weighted by the uncertainty of each shot. The dashed black lines show the ($1/e^2$) radial extent (w_0) of the drive beam at focus.

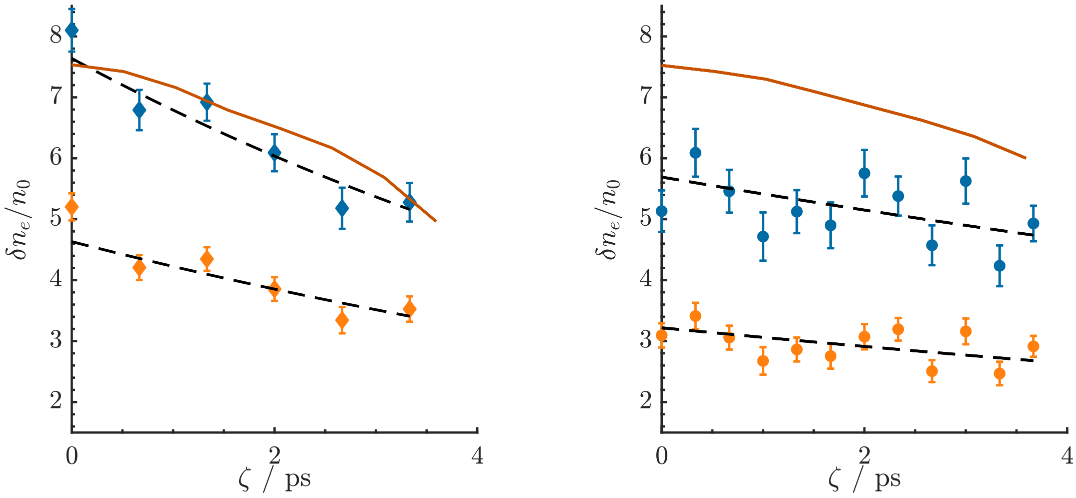

(a) (b)

Figure 6.21: Plot showing the decay of (a) hydrogen and (b) deuterium plasma wakefields. The red lines indicate the simulation results. The blue points show the average wakefield amplitude of 10 shots, at cell pressure P_{meas} for each shot. The red points show the average wakefield amplitude of the same shots, assuming a correction to the cell pressure $\alpha P_{\text{meas}} - P_0$, with $\alpha = 0.8$ and $P_0 = 4\,\text{mbar}$. The vertical bars indicate the error of the mean. The black striped lines show fits of the function $\exp(-\zeta/\tau_{\text{wf}})$ to the experimental data. The obtained τ_{wf} from these fits are summarised in Table 6.4.

Table 6.4: Characteristic wakefield decay time τ_{wf} in units of plasma periods, for hydrogen and deuterium plasmas. The results under P_{meas} show τ_{wf} for the measured cell pressure, whereas the results under $\alpha P_{\mathrm{meas}} - P_0$ show the results when applying a correction to the cell pressure based on the analysis presented in Section 6.3.1.

Plasma species	τ_{wf} / $2\pi\omega_p^{-1}$	
	(Cell pressure: P_{meas})	(Cell pressure: $\alpha P_{\mathrm{meas}} - P_0$)
Hydrogen	75 ± 19	97 ± 32
Deuterium	178 ± 97	178 ± 102

6.4 Conclusions

The results presented in this chapter confirm the feasibility of the FDH/TESS diagnostic to measure wake decay at delays as long as 4 ps. I have shown that an excited wakefield survives up to this delay, and measured the characteristic decay timescales of both hydrogen and deuterium plasma wakefields at low amplitudes. I found that hydrogen has characteristic decay time of 97 ± 32 plasma periods and and deuterium 178 ± 102 plasma periods. If the MP-LWFA pulses are spaced by one plasma period, this indicates that ~ 100 and ~ 180 pulses can be supported in hydrogen and deuterium plasmas respectively. However, future work is needed to confirm this conclusion; both simulations and experiments using a pulse-train as the drive beam rather than a single pulse. The results are in close agreement both to the timescales expected from PIC simulations and from the modulational instability, indicating that this is a likely to be responsible for the observed wakefield decay. The results are also in agreement with previous experiments which also measured the wakefield decay. However, this is the first experiment to measure wakefield decay in the linear, short-pulse, longitudinal wakefield regime that are of relevance for future LWFA and MP-LWFA experiments.

6.4.1 Future work

The maximum temporal delay could be further extended in order to measure the entire wakefield lifetime by adding a second Michelson interferometer with a 50:50 beam splitter to the probe beam line. This is because with a single Michelson interferometer, as shown Figure 6.5, increasing the separation between the probe and reference pulses decreases the spectral fringe spacing. The requirement for the fringes to be resolved by the spectrometer camera thus imposes a maximum pulse separation. However, this could be overcome by setting a longer pulse separation of for example 12 ps using the first interferometer, and using the second interferometer located before the spectrometer to undo some of the separation to for example 6 ps. Since this would generate further copies of the probe and reference pulses, care must be taken to ensure that the interfering pulses measured on the spectrometer are the correct ones.

CHAPTER 7

FREQUENCY DOMAIN HOLOGRAPHY

In addition to analysing the wakefield decay data using the TESS technique in the previous chapter, I also attempted to use the FDH analysis method to obtain the wakefield amplitude. In this chapter, I will outline how this analysis is carried out, and some fundamental limitations that arise when the frequency band of the probe and references pulses are similar to the plasma frequency. Finally, I will demonstrate that the TESS method can overcome these limitations and is therefore more robust than FDH analysis.

7.1 FDH analysis in practice

As outlined in Section 5.2.4, in FDH analysis one performs filtering in the time domain to isolate the third term in $S(\omega)$, the spectral interferogram:

$$S(\omega) = |\mathcal{E}'_{\text{probe}}(\omega)|^2 + |\mathcal{E}_{\text{ref}}(\omega)|^2 + \mathcal{E}'_{\text{probe}}(\omega)\mathcal{E}^*_{\text{ref}}(\omega) + c.c., \tag{7.1}$$

where *c.c.* stands for the complex conjugate of the previous term. The modulated probe pulse spectrum is then recovered by removing the reference spectrum and phase from this "sideband" term:

$$\mathcal{E}'_{\text{probe}}(\omega) = \frac{\mathcal{E}'_{\text{probe}}(\omega)\mathcal{E}^*_{\text{ref}}(\omega)}{|\mathcal{E}_{\text{ref}}(\omega)|} \exp\left[i\varphi_{\text{ref}}(\omega)\right]. \tag{7.2}$$

To obtain the temporal amplitude and phase one performs an inverse Fourier transform:

$$E'_{\text{probe}}(\zeta) = \frac{1}{\sqrt{2\pi}} \int \mathcal{E}'_{\text{probe}}(\omega) \exp\left(i\omega\zeta\right) d\omega \tag{7.3}$$

$$\phi(\zeta) = \Im\{\log[E'_{\text{probe}}(\zeta)]\} = \phi_{\text{probe}}(\zeta) + \phi_{\text{wf}}(\zeta), \tag{7.4}$$

where $\phi_{\text{wf}}(\zeta)$ is the wakefield phase that we seek to measure. In practice, I performed the following steps:

1. Used an inverse FT of the obtained spectral interferogram.
2. Applied a window centred on the temporal sideband located at $\Delta\zeta$ and shift the sideband to $\zeta = 0$ (Figure 7.1a).
3. Used a forward FT to spectral domain; this yields the spectral sideband $\mathcal{E}'_{\text{probe}}(\omega)\mathcal{E}^*_{\text{ref}}(\omega)$ (Figure 7.1b).
4. Divide by the reference pulse $|\mathcal{E}_{\text{ref}}(\omega)| \exp\left[-i\varphi_{\text{ref}}(\omega)\right]$ in order to recover the the wakefield-modulated probe spectrum $\mathcal{E}'_{\text{probe}}(\omega)$ (Figure 7.1c). I describe how the reference phase $\varphi_{\text{ref}}(\omega)$ was measured using the spectral blow-out technique in Section 6.2.3.
5. Performed an inverse FT to the temporal domain to obtain the probe pulse in the temporal domain $E(\zeta)$ (Figure 7.2)
6. Isolate the wakefield phase from the probe temporal phase (Figure 7.3a)

In order to remove the noise which was caused by the low-amplitude regions of the reference spectrum I applied a tapered Tukey window to the sideband before the division,

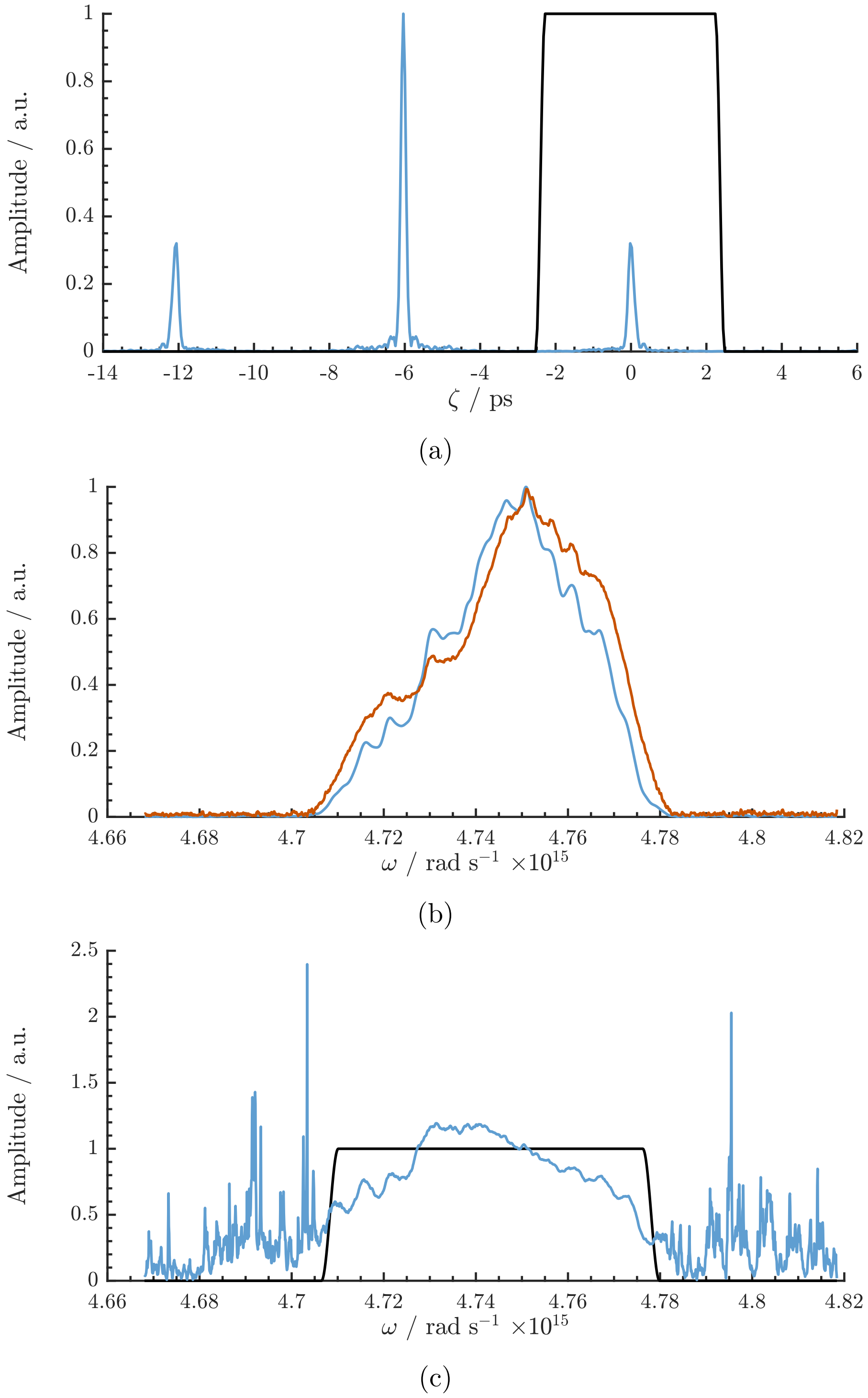

Figure 7.1: The FDH analysis procedure: (a) shifted and isolated sideband from the inverse Fourier-transformed spectral interferogram (blue) using a tapered Tukey window (black), (b) the forward Fourier transformed sideband term $\mathcal{E}_{\text{probe}}(\omega)\mathcal{E}^*_{\text{ref}}(\omega)$ (blue) and the measured reference spectrum (red), and (c) the recreated probe spectrum (blue) and window used to remove noise caused by division with the reference spectrum (black).

shown in Figure 7.1c. Performing an inverse Fourier transform, I then obtained the probe temporal profile. We saw earlier that the corresponding phase is a sum of the probe phase and the wakefield phase:

$$\phi(\zeta) = \phi_{\mathrm{probe}}(\zeta) + \phi_{\mathrm{wf}}(\zeta). \tag{7.5}$$

In order to recover the wakefield phase $\phi_{\mathrm{wf}}(\zeta)$ I needed to remove the probe phase terms $\phi_{\mathrm{probe}}(\zeta)$ (these are due to the second and higher order terms in the spectral phase). In order to do so, I obtained the phase of a shot taken without a wakefield $\phi(\zeta)$. This is shown in Figure 7.2. I then performed a fit to this phase by finding the probe spectral phase terms that most closely correspond to this temporal phase. This method for measuring the spectral phase is almost identical to how I measured the spectral phase in Section 6.2.3, except that I perform a fit to the temporal phase itself rather than to its derivative. The obtained spectral phase components are those of the probe beam, $\varphi^{(2)} = (20\,030 \pm 20)\,\mathrm{fs}^2$, $\varphi^{(3)} = (3.6 \pm 0.5)\,\mathrm{fs}^3$. These values are close to those measured using the spectral blowout technique, summarised in Table 6.3. Note that the results are not identical since the reference pulse spectral phase is used in this procedure and therefore contributes an additional source of error. After subtracting the fitted temporal phase, the remaining phase is the oscillating phase shift induced by the wakefield on the probe pulse. The obtained phase map is shown in Figure 7.3a, and a lineout taken through the centre of the wakefield is shown in Figure 7.3b (here I used Equation (5.55) to convert from phase to density). It was observed that the measured wakefield was modulated, showing a maximum away from the centre and decaying towards the centre of the pulse. In order to understand this phenomena, I performed numerical and analytical calculations using a simulated probe spectrum; this process is described in the next section.

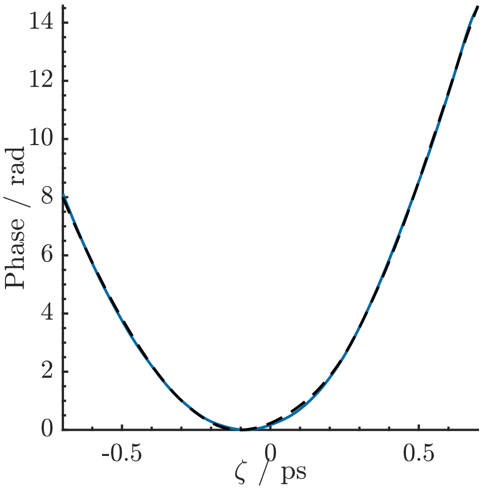

Figure 7.2: Temporal phase obtained from the FDH analysis. The blue line shows the experimentally obtained phase, and the black dashed line shows a fit of the spectral phase using the probe measured spectrum.

7.2 Cause of the wakefield modulation

In other to understand the reason for modulation of the recovered wakefield, it can be studied as a deconvolution problem [118]. Here, the goal is to recover an unknown function $f(t)$ that has been convolved with a known transfer function $K(t)$:

$$g(t) = \int K(t - t')f(t')dt' \equiv K * f(t), \tag{7.6}$$

where $g(t)$ is called the image. By performing a Fourier transform, the function $f(t)$ is easily recovered by division in the frequency domain. It was then be transformed back to the temporal domain:

$$\hat{g}(\omega) = \hat{f}(\omega)\hat{K}(\omega) \tag{7.7}$$

$$\hat{f}_{\text{rec}}(\omega) = \frac{\hat{g}(\omega)}{\hat{K}(\omega)} \tag{7.8}$$

$$f(t) = \text{FT}[\hat{f}_{\text{rec}}(\omega)], \tag{7.9}$$

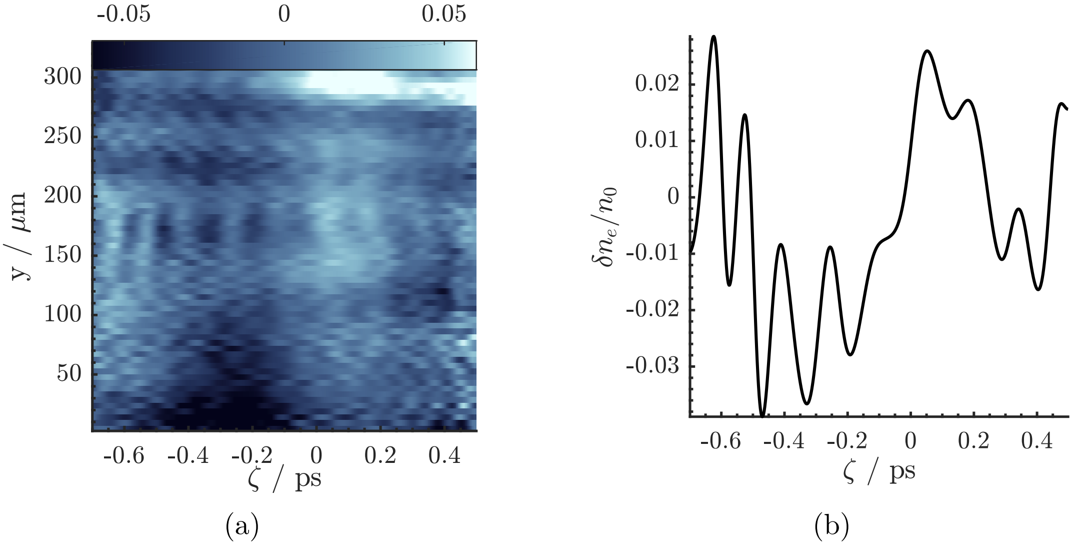

Figure 7.3: (a) The spatial variation of the electron density recovered by the FDH method (b) lineout showing the wakefield amplitude through the centre of the wakefield.

where the hats signify the Fourier transform of the respective functions. The deconvolution process is very sensitive to noise due to the division by the transfer function $\hat{K}(\omega)$, which will be very small outside some frequency range. Denoting the band $\mathcal{B}(y)$ of a function y as the region over which it is non-zero, we see from Equation (7.7) that $\hat{g}(\omega)$ is band-limited by the function with the smallest band $\mathcal{B}(\hat{g}) = \min\{\mathcal{B}(\hat{K}), \mathcal{B}(\hat{f})\}$. One therefore sees from Equation (7.8) that the recovered $\hat{f}_{\text{rec}}(\omega)$ is also band-limited by:

$$\mathcal{B}(\hat{f}_{\text{rec}}) = \min\{\mathcal{B}(\hat{g}), \mathcal{B}(\hat{K})\} \tag{7.10}$$

$$= \min\{\min\{\mathcal{B}(\hat{K}), \mathcal{B}(\hat{f})\}, \mathcal{B}(\hat{K})\} \tag{7.11}$$

$$= \min\{\mathcal{B}(\hat{f}), \mathcal{B}(\hat{K})\}. \tag{7.12}$$

This shows that in order to fully recover $\hat{f}(\omega)$, the band of $\hat{K}$ must be equal or greater than that of $\hat{f}$: $\mathcal{B}(\hat{K}) \geq \mathcal{B}(\hat{f})$. The division in Equation (7.8) looks just like that in FDH if one identifies $K(\omega)$ as the reference spectrum $\mathcal{E}_{\text{ref}}(\omega)$ and $f(\omega)$ as the modulated probe spectrum $\mathcal{E}'_{\text{probe}}(\omega)$. In Section 5.2.3, I showed that the effect of a sinusoidal phase modulation with amplitude ϕ_0 on the probe pulse is to generate an infinite number of copies of the spectrum, offset by $k\omega_p$ and multiplied by a Bessel function of the first kind $J_k(\phi_0)$ (where k is an integer). I now briefly revisit this theory in order to understand the effects of spectral cut-off of the modulated probe pulse, starting with the Jacobi-Anger expansion of the modulated probe:

$$\begin{aligned} E'(\zeta) &= E(\zeta)\exp[i\phi_0\sin(\omega_p\zeta)] && (7.13)\\ &= E(\zeta)\sum_{k=-\infty}^{\infty} J_k(\phi_0)\exp(ik\omega_p\zeta). && (7.14) \end{aligned}$$

Including only the three terms $k = -1$, $k = 0$, $k = 1$ one has:

$$\begin{aligned} E'(\zeta) &\approx E(\zeta)\Big[J_{-1}(\phi_0)\exp(-i\omega_p\zeta) + J_0(\phi_0) + J_1(\phi_0)\exp(i\omega_p\zeta)\Big] && (7.15)\\ &= E(\zeta)\Big[J_0(\phi_0) + J_1(\phi_0)\exp(i\omega_p\zeta) - J_1(\phi_0)\exp(-i\omega_p\zeta) + \Big] && (7.16)\\ &= E(\zeta)\Big\{J_0(\phi_0) + J_1(\phi_0)[\exp(i\omega_p\zeta) - \exp(-i\omega_p\zeta)]\Big\} && (7.17)\\ &\approx E(\zeta)\left\{1 + \frac{\phi_0}{2}[2i\sin(\omega_p\zeta)]\right\} && (7.18)\\ &= E(\zeta)\Big\{1 + i\phi_0\sin(\omega_p\zeta)\Big\}. && (7.19) \end{aligned}$$

In Equation (7.18), I used the expansion of the the Bessel function from equation (5.48), where I showed that $J_0(\phi_0) \approx 1$ and $J_1(\phi_0) \approx \phi_0/2$ if $\phi_0 \ll 1$. The last expression, equation (7.19), corresponds to the first two terms of the Taylor expansion of the exponential function: $\exp(x) \approx 1 + x$, and the phase of the bracketed expression is the same as in equation (7.13). Since I am primarily concerned with the phase, this shows that the three terms $k = -1$, $k = 0$, and $k = 1$ are necessary and sufficient to recover the probe phase. In the spectral domain, I can therefore expand equation 5.31 using only these three terms:

$$\begin{aligned} \mathcal{E}'_{\text{probe}}(\omega) &= \sum_k J_k(\phi_0)\mathcal{E}_{\text{probe}}(\omega - k\omega_p) && (7.20)\\ &\approx J_{-1}(\phi_0)\mathcal{E}_{\text{probe}}(\omega + \omega_p) + J_0(\phi_0)\mathcal{E}_{\text{ref}}(\omega) + J_1(\phi_0)\mathcal{E}_{\text{probe}}(\omega - \omega_p). && (7.21) \end{aligned}$$

Assuming that the probe and reference spectra have initially equal band, it follows that $\mathcal{B}(\mathcal{E}'_{\text{probe}}) > \mathcal{B}(\mathcal{E}_{\text{probe}}) = \mathcal{B}(\mathcal{E}_{\text{ref}})$ due to the terms that are shifted by $\omega \pm \omega_p$. This means that the recorded probe spectrum is partially cut to a smaller band by the reference spectrum. Using a reference pulse with a band greater than the plasma frequency ω_p, $\mathcal{B}(\mathcal{E}_{\text{ref}}) \geq \omega_p$, means that more of the probe pulse can be recovered which reduces this modulation. In Section 7.2.1, I perform a numerical calculation using FFT to study the effect of the band-limited spectrum on the recovered wakefield, and in Section 7.2.2 I obtain an analytic expression of the band-limited probe pulse in the temporal domain. I show that these are in good agreement and use these to obtain a limit of the plasma frequency ω_p for which the wakefield amplitude can be recovered, for a given bandwidth. Finally, in Section 7.3 I show that TESS analysis can overcome this issue by measuring the spectral overlap factor, which can be seen as a correction term.

7.2.1 FFT calculation

I performed a numerical calculation assuming a super-Gaussian spectrum of the probe pulse (see Figure 7.4a) to study the effect of the band-limited probe spectrum on the recovered wakefield amplitude. The $k = -1$, $k = 0$, and $k = 1$ terms in the modulated probe spectrum are plotted separately in Figure 7.4b. Note that large parts of the modulated spectrum appear outside the band of the reference spectrum. Performing an FFT of the full probe spectrum and the band-limited probe spectrum, I obtained the wakefield amplitudes from the phase of the probe in the temporal domain. This is plotted in Figure 7.5a. Using a band-limited probe leads to a modulation in the recovered wakefield amplitude that is similar to the one observed experimentally in Figure 7.3b. In Figure 7.5b I plot the wakefield amplitude in the centre of the simulated wakefield (measured using the first wakefield trough and peak on either side of $\zeta = 0$) as a function of the plasma frequency. This shows that the modulation decreases at lower plasma frequencies, as expected from the above discussion.

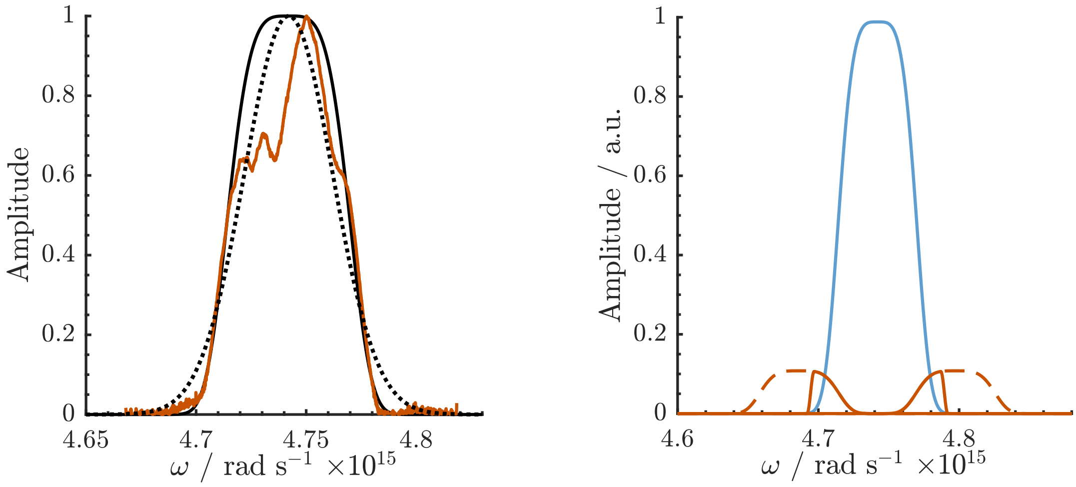

(a)

(b)

Figure 7.4: (a) Measured probe spectrum (red), assumed super-Gaussian spectrum (black solid line), and assumed Gaussian spectrum (black dotted line). (b) Modulated super-Gaussian probe spectrum. The blue line corresponds to the amplitude of the $k = 0$ term and the red lines to the amplitudes of the individual $k = \pm 1$ terms from Equation (7.21). The red dashed lines show the parts of the $k = \pm 1$ terms that are cut off due to the band-limited reference spectrum.

7.2.2 Theoretical calculation

I also found an analytic expression that could be used to study the recovered phase of a band-limited probe spectrum. Assuming a Gaussian probe spectrum of width $\delta\omega$, GDD $\varphi^{(2)}$ and centre frequency ω_0, one has the following expression of the probe spectrum:

$$\mathcal{E}(\omega) = \exp\left[\frac{(\omega - \omega_0)^2}{2\delta\omega^2}\right] \exp\left[i\frac{\varphi^{(2)}}{2}(\omega - \omega_0)^2\right]. \tag{7.22}$$

Calculating the Fourier transform of the band-limited probe is equivalent to setting the integration limits of the transform to $\omega_L > -\infty$ and $\omega_U < \infty$. The Fourier transform

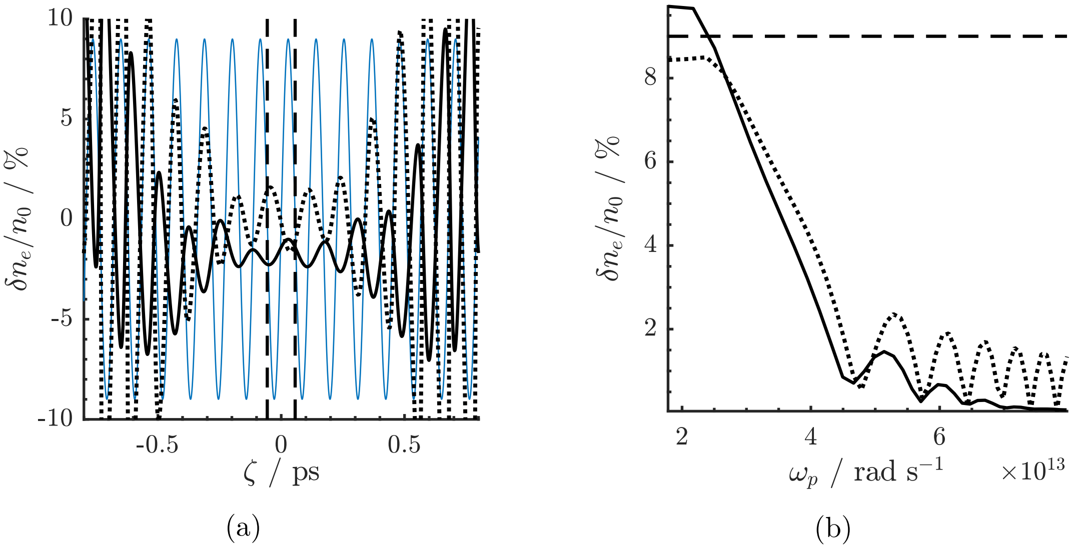

Figure 7.5: (a) Wakefield amplitude obtained using the full super-Gaussian probe spectrum (blue), the band-limited super-Gaussian spectrum (black solid line), and the theoretical calculation based on the Gaussian spectrum as described in Section 7.2.2 (black dotted line). In this plot I have assumed a plasma frequency of $\omega_p = 5.5 \times 10^{13}$ rad s^{-1}. (b) Centre wakefield amplitude as a function of plasma frequency. The solid line shows the recovered wakefield amplitude between the dashed black lines in the centre of (a), using the band-limited super-Gaussian probe spectrum. The dotted line shows the centre amplitude from the theoretical calculation assuming a Gaussian spectrum. The horizontal dashed line shows the true wakefield amplitude.

is thus:

$$
\begin{aligned}
E(\zeta) &= \mathrm{FT}[\mathcal{E}(\omega)] && (7.23)\\
&= \frac{1}{\sqrt{2\pi}} \int_{\omega_L}^{\omega_U} \exp\left[\frac{(\omega-\omega_0)^2}{2\delta\omega^2}\right] \exp\left[i\frac{\varphi^{(2)}}{2}(\omega-\omega_0)^2\right] \exp(i\omega\zeta)d\omega && (7.24)\\
&= \frac{1}{\sqrt{2\pi}} \int_{\omega_L}^{\omega_U} \exp\left[\frac{(\omega-\omega_0)^2}{2\delta\omega^2} + i\frac{\varphi^{(2)}}{2}(\omega-\omega_0)^2 + i\omega\zeta\right] d\omega. && (7.25)
\end{aligned}
$$

I complete the square in the argument and make the change of variables:

$$
\begin{aligned}
u(\omega,\zeta) &= \frac{\omega\varepsilon - \Omega(\zeta)}{\sqrt{\varepsilon}} && (7.26)\\
d\omega &= \frac{1}{\sqrt{\varepsilon}} du. && (7.27)
\end{aligned}
$$

I have also introduced the constants

$$\varepsilon = \frac{1}{2\delta\omega^2} + i\varphi^{(2)} \tag{7.28}$$

$$\Omega(\zeta) = \varepsilon\omega_0 + i\zeta. \tag{7.29}$$

With these substitutions I obtain the following expression of the integral

$$\begin{aligned} E(\zeta) &= \frac{1}{2\sqrt{2\varepsilon}} \exp\left[\frac{\Omega(\zeta)^2}{\varepsilon} - \varepsilon\omega_0^2\right] \frac{2}{\sqrt{\pi}} \int_{u(\omega_L,\zeta)}^{u(\omega_U,\zeta)} \exp(-u^2)du & (7.30)\\ &= \frac{1}{2\sqrt{2\varepsilon}} \exp\left[\frac{\Omega(\zeta)^2}{\varepsilon} - \varepsilon\omega_0^2\right] \{\mathrm{erf}[u(\omega_U,\zeta)] - \mathrm{erf}[u(\omega_L,\zeta)]\}, & (7.31) \end{aligned}$$

where the error function is defined as:

$$\mathrm{erf}(x) = \frac{2}{\sqrt{\pi}} \int_0^x \exp(-t^2)dt. \tag{7.32}$$

Note that in the limit $\omega_L \to -\infty$, $\omega_U \to \infty$, I obtain

$$E(\zeta) = \frac{1}{2\sqrt{2\varepsilon}} \exp\left[\frac{\Omega(\zeta)^2}{\varepsilon} - \varepsilon\omega_0^2\right]. \tag{7.33}$$

To obtain the band-limited wakefield amplitude, I simply evaluate:

$$\phi_{\mathrm{wf}}(\zeta) = \arg\{\mathrm{FT}[\mathcal{E}'_{\mathrm{probe}}(\omega)]\} - \arg\{\mathrm{FT}[\mathcal{E}_{\mathrm{probe}}(\omega)]\}, \tag{7.34}$$

with the modulated probe spectrum given by:

$$\mathcal{E}'_{\mathrm{probe}}(\omega) = J_{-1}(\phi_0)\mathcal{E}_{\mathrm{probe}}(\omega+\omega_p) + J_0(\phi_0)\mathcal{E}_{\mathrm{ref}}(\omega) + J_1(\phi_0)\mathcal{E}_{\mathrm{probe}}(\omega-\omega_p), \tag{7.35}$$

and the Fourier transform FT calculated according to equation (7.24). For a band-limited Gaussian probe spectrum (where the unmodulated probe spectrum have a bandwidth of $\delta\omega = 2 \times 10^{13}$ rad s^{-1}, shown in Figure 7.4a) with lower frequency

$\omega_L = 4.705 \times 10^{15}$ rad s^{-1} and upper frequency $\omega_U = 4.78 \times 10^{15}$ rad s^{-1}, we obtain the wakefield amplitude plotted in Figure 7.5a. Using the centre of the wakefield, around $\zeta = 0$, as a measure of the modulation we calculate this amplitude as a function of plasma frequency. The result is shown in Figure 7.5b. The wakefield amplitude can be recovered if the plasma frequency is $\omega_p \leq 3 \times 10^{13}$ rad s^{-1}, corresponding to a density $n_0 \leq 2.8 \times 10^{23}\,\mathrm{cm}^{-3}$ (in a hydrogen plasma).

7.3 FDH versus TESS

In the previous section I showed that an issue with frequency domain holography is that the wakefield can only be correctly recovered if the reference spectrum has band greater than the plasma frequency. An important question is therefore if this is an issue for TESS analysis as well. To answer this, I start by reviewing the expression for the spectral interference $S(\omega)$:

$$S(\omega) = |\mathcal{E}'_{\mathrm{probe}}(\omega)|^2 + |\mathcal{E}_{\mathrm{ref}}(\omega)|^2 + \mathcal{E}'_{\mathrm{probe}}(\omega)\mathcal{E}^*_{\mathrm{ref}}(\omega) + c.c., \tag{7.36}$$

where *c.c.* stands for the complex conjugate of the previous term. By performing an inverse Fourier transform of this term, I obtain:

$$S(\zeta) = \frac{1}{\sqrt{2\pi}} \int |\mathcal{E}'_{\mathrm{probe}}(\omega)|^2 \exp{(i\omega\zeta)} d\omega + \frac{1}{\sqrt{2\pi}} \int |\mathcal{E}_{\mathrm{ref}}(\omega)|^2 \exp{(i\omega\zeta)} d\omega \tag{7.37}$$

$$+ \frac{1}{\sqrt{2\pi}} \int \mathcal{E}'_{\mathrm{probe}}(\omega)\mathcal{E}^*_{\mathrm{ref}}(\omega) \exp{(i\omega\zeta)} d\omega + c.c.. \tag{7.38}$$

Focussing on the third term which is used in TESS analysis, I use Equation (7.20) to expand this as (omitting the prefactor $1/\sqrt{2\pi}$)

$$\int \mathcal{E}'_{\text{probe}}(\omega)\mathcal{E}^*_{\text{ref}}(\omega)\exp(-i\omega\zeta)d\omega = \sum_k J_k(\phi_0) \underbrace{\int \mathcal{E}_{\text{probe}}(\omega - k\omega_p)\mathcal{E}^*_{\text{ref}}(\omega)\exp(-i\omega\zeta)d\omega}_{H(\zeta,k\omega_p)} . \tag{7.39}$$

It can be shown [105] that the integral $H(\zeta, k\omega_p)$ is maximised at $\zeta = k\varphi^{(2)}\omega_p$, where it takes the magnitude:

$$|H(k\varphi^{(2)}\omega_p, k\omega_p)| = \int |\mathcal{E}_{\text{probe}}(\omega - k\omega_p)||\mathcal{E}_{\text{ref}}(\omega)|d\omega. \tag{7.40}$$

The TESS analysis method consists measuring the relative amplitudes of $k = 1$ term and the $k = 0$ term from Equation (7.39), so I get:

$$r = \frac{J_1(\phi_0)}{J_0(\phi_0)}\frac{|H(\varphi^{(2)}\omega_p, \omega_p)|}{|H(0,0)|} \tag{7.41}$$

$$\frac{|H(\varphi^{(2)}\omega_p, \omega_p)|}{|H(0,0)|} = \frac{\int |\mathcal{E}_{\text{probe}}(\omega - \omega_p)||\mathcal{E}_{\text{ref}}(\omega)|d\omega}{\int |\mathcal{E}_{\text{probe}}(\omega)||\mathcal{E}_{\text{ref}}(\omega)|d\omega} = \mathcal{F}(\omega_p). \tag{7.42}$$

This is just the spectral overlap function $\mathcal{F}(\omega_p)$ from Equation (6.27). I therefore have:

$$r = \frac{J_1(\phi_0)}{J_0(\phi_0)}\mathcal{F}(\omega_p), \tag{7.43}$$

from which I obtain the phase amplitude ϕ_0 of the assumed sinusoidal wakefield. I therefore conclude that TESS, in contrast to FDH, does not require the band of the reference spectrum to be greater than the plasma frequency. Instead, it only requires that the spectral overlap function $\mathcal{F}(\omega_p)$ is greater than zero, and by measuring the (unmodulated) probe and reference spectra separately it can be estimated using the measured plasma density as shown in Chapter 6.

7.4 Conclusions

In this chapter I presented an attempt to recover the wakefield temporal profile using FDH analysis of the data that was presented in Chapter 6, and observed that the obtained wakefield was modulated. By making the connection to the well-known problem of Fourier deconvolution, I showed that this is because the band of the reference spectrum limits the band of the recovered probe spectrum. By using simulated probe and reference spectra I showed using numerical and theoretical calculations that the band-limited probe spectrum generates a modulated wakefield amplitude similar to that observed experimentally. In order for FDH to work as described in this chapter, the reference spectra must therefore be wider than the plasma frequency. I also showed that in TESS analysis, the requirement on the band of the reference spectra is less strict, as long as one can correct for the partial overlap of the probe and reference spectra by calculating the spectral overlap factor.

CHAPTER 8

SUMMARY

Particle accelerators have a wide range of applications in science and technology, and have directly contributed to a substantial fraction of research awarded with Nobel prizes in physics since 1938. Compared to traditional particle accelerators, laser plasma acceleration (LPA) is a much more compact acceleration method capable of generating femtosecond long particle bunches that could lead to new applications in fields such as biotechnology and material science.

In this thesis, I have described several different laser-driven accelerator schemes: laser wakefield acceleration (LWFA), laser beatwave acceleration (LBWA), self-modulated laser wakefield acceleration (SM-LWFA), and multi-pulse laser wakefield acceleration (MP-LWFA). I have argued that MP-LWFA provides a way towards high-repetition rate laser plasma accelerators, which is a requirement for their wider applications in science and technology. Another requirement is the development of low-density plasma waveguides capable of guiding the high-intensity drive laser pulses over a ~ 10 centimetre distance, or several Rayleigh ranges.

The problem of diagnosing these low-density plasma waveguides, i.e. measuring their density profiles, is described in Chapters 3 and 4. Plasma diagnostics for LPA experiments (Chapter 3) are challenging as they simultaneously require a high spatial and temporal resolution. As an example, plasma channel waveguides have a size on the order of 100 µm, requiring a resolution better than 10 µm. They are also rapidly evolving, on the scale of picoseconds, requiring sub-ps temporal resolution. A third challenge is the low plasma density, on the order of $n_0 \approx 10^{17} - 10^{18}\,\mathrm{cm}^{-3}$, leading to small refractive index differences. This is at the lower range of what interferometers using 800 nm or 400 nm light can measure, due to a low integrated phase shift (on the order of 100 mrad when probing transversely). I showed that adding a second probe along a different axis of projection (the experimental design is shown in Figure 3.7) can help to reconstruct the density of asymmetric plasma channels. In order to reduce the shot-to-shot variation, a kHz probe beam should be used for plasma diagnostics in the future. Because of wavefront errors in the probe beam, a reference shot is usually recorded without any plasma that can be used to remove these errors. As these wavefront errors change over time due to mechanical vibrations and deformations of the optical elements in the laser chain, recording the probe and reference shots at short time-intervals ensures that they are taken at similar conditions. It is also conceivable to use longer probe wavelengths, as this increases the phase shift acquired by propagated through the plasma. In permanent installations of laser plasma acceleration an operationally simple probe layout is required in order to reduce maintenance. Due to their extreme simplicity, Shack-Hartmann sensor are most likely to fulfil this task, since they have a very simple optical setup. As of now however, they lack the spatial resolution needed to resolve the plasma channels (currently approximately 150 µm).

In Chapter 4 I provided an overview of the process by which an interferogram (or deflectogram) is analysed. The obtained phase can in turn be converted into a density using the calculations presented in Section 3.2. I discussed three different methods for calculating the projected phase from an interferogram: fringe tracing, the Fourier transform method, and the continuous wavelet transform method. I showed that the latter two are preferred due to their higher sensitivity. Furthermore, the continuous wavelet transform method offers the additional benefit of working even when the fringe frequency is not constant. Next, I discussed the problem of phase unwrapping a 2D image, since the phase obtained in the interferogram analysis can only be determined up to a factor of 2π. Assuming that the phase is continuous everywhere discontinuities in the obtained phase can be corrected by adding factors of 2π. If the Itoh condition is satisfied this can be done uniquely for a 2D phase image. However, the presence of residues (2×2 group of pixels with a path integral of $\pm 2\pi$) breaks this, which means that there is more than one way to unwrap the phase. Several algorithms have been developed to ensure a unique phase unwrapping solution of which we discuss two common approaches: branch cutting (the Goldstein algorithm) and quality-guided unwrapping.

Since the measured phase is a projection of the plasma structure, the final step of phase inversion is necessary in order to obtain the true phase. Up to this point, the procedure for analysing interferograms and deflectograms is identical, but here different solutions of the inversion problem are employed as the former measures projected phase and the latter the deflected angle. For interferograms, I showed that fitting Laguerre-Gaussian basis functions with known inverted forms is a robust way to obtain the inverted phase, even in the presence of one-dimensional asymmetries in the original phase. I also showed that using the two-axis projection interferometer, the second projection axis allows one to determine the angle and position of asymmetries in any direction in the plane. I also showed how the phase obtained from deflectometry can be inverted using the two-point algorithm to calculate the Abel inversion. Finally, I showed a full example of how to analyse an interferogram that was captured in an experimental campaign to measure the density of plasma channels.

In the second part of the thesis, Chapters 5 and 6, I discussed another crucial aspect of building a high-repetition rate laser plasma accelerator using the MP-LWFA scheme: that of wakefield decay. In the theory chapter (Chapter 2), I explained that ions are usually assumed to be stationary in the calculations, only providing a constant background for the oscillating electrons in the plasma. While this assumption holds in the LPA schemes where the drive pulse is much shorter than the plasma wavelength, this is not necessarily true if the drive pulse (or train of drive pulses) is much longer than that. Ion motion leads several plasma instabilities that eventually leads to the decay of plasma wakefields (with stable ions, they would eventually decay from other mechanisms that occur over much longer timescales). Several wakefield decay mechanisms are described in Chapter 5: Landau damping, collisional damping, and the modulational instability. I showed that of these, the modulational instability is the fastest, occurring on the picosecond timescale. I also presented several previous experiments that have measured the wakefield decay time. In Chapter 6, I presented the results of an experimental campaign to measure the decay time of hydrogen and deuterium plasma wakes in the linear regime. I have for the first time studied a parameter regime that is relevant both for current and future LWFA experiments. The primary motivation of this experiment was to investigate the feasibility of the MP-LWFA scheme as the wakefield lifetime limits the number of pulses that can be used in a pulse train as a wakefield driver. Using for the first time a FDH diagnostic and the TESS analytic method to measure the decay of a plasma wakefield I measured the wakefield amplitude between 0-4 ps after ionisation. Our results indicate that within this timeframe the wakefields have a characteristic decay time scale of ~ 100 plasma periods in hydrogen plasmas and up to ~ 180 plasma periods in deuterium. Assuming that the drive pulses are separated by one plasma period, this means that pulse trains up to ~ 100 (~ 180) pulses may be useful to excite a wakefield in hydrogen (deuterium); beyond this limit it is likely that the wakefield would saturate and additional pulses would only maintain, rather than add, to the wakefield amplitude.

8.1 Future work

In this thesis I have presented a possible path towards high repetition rate laser wakefield accelerators, with results that open the door to future work. Guiding high-intensity laser pulses in low-density plasma channels have already been achieved over 100 mm by the author's group. This experimental work should be extended to accelerating electrons in these channels; this would require an electron injection scheme (for example through ionisation injection or downramp injection). Another issue is the generation of plasma channels at high repetition rates ($\geq$ kHz), where the timescale is approaching plasma timescales such as the recombination time. Thirdly, the staging of several channels after each other is required for future collider experiments, and a way to couple both the laser and electron beam into the channels is required.

I showed results indicating that the plasma wakefield decay after a single pulse is sufficiently slow to not be a concern for the MP-LWFA scheme. Here, further work is required to ensure that this conclusion holds for pulse trains as well as for single pulses. For example, the continuous excitation of wakefields in addition to the build-up of plasma instabilities through the modulational instability could change the seeding of the instability. This should be done both in simulations and experimentally, by repeating the experiments described in Chapter 6 with a pulse train rather than a single pulse. Furthermore, other instabilities such as the oblique mode instability should be studied in the context of wakefield decay [119].

A further direction of the work is the combination of the MP-LWFA scheme with the plasma channel work; the interaction between a pulse train and a plasma waveguide should be investigated theoretically and experimentally.

Combining the MP-LWFA technique with the low-density, all-optical plasma channels developed by the group is a promising direction in the pursuit of multi-GeV laser-plasma accelerators capable of high-repetition-rate operation. It is hoped that the work presented in this thesis is a contribution towards that objective.

Appendices

APPENDIX A

THE CONTINUOUS WAVELET TRANSFORM COEFFICIENTS

I want to calculate the wavelet coefficients for the function $f(x) = a(x)\cos\left[\theta(x)\right]$, given wavelets of the form:

$$\varphi_{s,u}(x) = g_{s,u,\xi}(x)\exp(-i\xi u), \tag{A.1}$$

where $\xi = \eta/s$ and $g_{s,u,\xi}(x)$ is given by:

$$g_{s,u,\xi}(x) = \frac{1}{\sqrt{s}} g\left(\frac{x-u}{s}\right)\exp(-i\xi x). \tag{A.2}$$

I will follow the procedure described in Stéphane [75]. The wavelet coefficients are given by:

$$\begin{align} Wf(u,s) &= \int_{-\infty}^{+\infty} f(x)\varphi_{s,u}(x)dx \tag{A.3}\\ &= \int_{-\infty}^{+\infty} a(x)\cos\theta(x) g_{s,u,\xi}(x)\exp(-i\xi u)dx \tag{A.4}\\ &= \exp(-i\xi u)\int_{-\infty}^{+\infty} a(x)\cos\theta(x) g_s(x-u)\exp(-i\xi x)dx. \tag{A.5}\end{align}$$

In equation A.5 I introduced the notation:

$$g_s(x) = \frac{1}{\sqrt{s}} g\left(\frac{x}{s}\right). \tag{A.6}$$

I evaluate the integral in equation (A.5), expanding $\cos[\theta(x)] = \{\exp[i\theta(x)] + \exp[-i\theta(x)]\}/2$:

$$\begin{aligned}
&\int_{-\infty}^{+\infty} a(x)\cos\theta(x) g_s(x-u)\exp(-i\xi x)dx \\
&= \frac{1}{2}\int_{-\infty}^{+\infty} a(x)\{\exp[i\theta(x)] + \exp[-i\theta(x)]\} g_s(x-u)\exp(-i\xi x)dx \\
&= \underbrace{\frac{1}{2}\int_{-\infty}^{+\infty} a(x)\exp[i\theta(x)] g_s(x-u)\exp[-i\xi x]dx}_{I(\theta)} \\
&+ \underbrace{\frac{1}{2}\int_{-\infty}^{+\infty} a(x)\exp[-i\theta(x)] g_s(x-u)\exp[-i\xi x]dx}_{I(-\theta)}\,.
\end{aligned} \tag{A.7}$$

In the first integral, I perform a change of variable from x to $x+u$:

$$\begin{aligned}
I(\theta) &= \frac{1}{2}\int_{-\infty}^{+\infty} a(x)\exp[i\theta(x)] g_s(x-u)\exp(-i\xi x)dx \\
&= \frac{1}{2}\int_{-\infty}^{+\infty} a(x+u)\exp[i\theta(x+u)] g_s(x)\exp[-i\xi(x+u)]dx.
\end{aligned} \tag{A.8}$$

I assume that $a(x)$ and $\theta'(x)$ are slowly varying and expand:

$$\begin{aligned}
a(x+u) &\approx a(u) \\
\theta(x+u) &\approx \theta(u) + x\theta'(u).
\end{aligned} \tag{A.9}$$

Here I am making the assumption that $|a'(u)|$ is small compared to $|a(u)|$; it can be shown that this leads to an error on the order $\epsilon \leq s|a'(u)|/|a(u)|$ [75]. Using this I write:

$$\begin{aligned} I(\theta) &= \frac{1}{2}\int_{-\infty}^{+\infty} a(u)\exp[i\theta(u) + x\theta'(u)]g_s(x)\exp\left[-i\xi(x+u)\right]dx && \text{(A.10)}\\ &= \frac{1}{2}\exp(i(\theta(u)-\xi u))a(u)\int_{-\infty}^{+\infty} g_s(x)\exp\Big\{-it\Big[\xi-\theta'(u)\Big]\Big\}dx && \text{(A.11)}\\ &= \frac{1}{2}\exp(i(\theta(u)-\xi u))a(u)\int_{-\infty}^{+\infty} \frac{1}{\sqrt{s}}g\left(\frac{x}{s}\right)\exp\Big\{-it\Big[\xi-\theta'(u)\Big]\Big\}dx. && \text{(A.12)}\end{aligned}$$

Where I have replaced $g_s(t) = (1/\sqrt{s})g(x/s)$ in the integral above. Through a change of variables $x \to x' = x/s$ I obtain:

$$\int_{-\infty}^{+\infty} \frac{1}{\sqrt{s}}g\left(\frac{x}{s}\right)\exp\Big(-it\Big(\xi-\theta'(u)\Big)\Big)dx = \int_{-\infty}^{+\infty}\sqrt{s}g\left(x'\right)\exp\Big(-isx'\Big(\xi-\theta'(u)\Big)\Big)dx'. \tag{A.13}$$

Rewriting slightly, I recognise the expression for $\hat{g}(\omega)$, the Fourier components of g at the frequency $\omega = s\left[\xi - \theta'(u)\right]$:

$$\sqrt{s}\int_{-\infty}^{+\infty} g\left(x'\right)\exp\Big(-isx'\Big(\xi-\theta'(u)\Big)\Big)dx' = \sqrt{s}\hat{g}\Big(s\Big[\xi-\theta'(u)\Big]\Big). \tag{A.14}$$

Finally, I obtain the expression:

$$I(\theta) = \frac{\sqrt{s}}{2}\exp\Big\{i\left[\theta(u)-\xi u\right]\Big\}a(u)\hat{g}\Big(s\Big[\xi-\theta'(u)\Big]\Big). \tag{A.15}$$

Similarly, for $I(-\theta)$ I obtain:

$$I(-\theta) = \frac{\sqrt{s}}{2}\exp\Big\{-i\left[\theta(u)+\xi u\right]\Big\}a(u)\hat{g}\Big(s\Big[\xi+\theta'(u)\Big]\Big). \tag{A.16}$$

Assuming that the Fourier transform of the window function $\hat{g}(\omega)$, which is maximum at $\omega = 0$ has a limited bandwidth $\delta\omega$, and that $\theta' \geq \delta\omega/s$, I see that $\hat{g}\left(\xi + \theta'(u)\right) \approx 0$ and I may neglect this term. The expression for the wavelet coefficients of $f(x)$ can now be obtained by using equation (A.15) in equation (A.5) and:

$$\begin{aligned} Wf(u,s) &= \exp(-i\xi u)\frac{\sqrt{s}}{2}\exp\Big\{i\left[\theta(u)-\xi u\right]\Big\}\, a(u)\hat{g}\left(s\Big[\xi-\theta'(u)\Big]\right) && \text{(A.17)} \\ &= \frac{\sqrt{s}}{2}a(u)\exp[i\theta(u)]\hat{g}\left(s\Big[\xi-\theta'(u)\Big]\right). && \text{(A.18)} \end{aligned}$$

APPENDIX B

NON-LINEAR LEAST SQUARES FITTING

Given a set of measured data $y(x)$ that we assume can be described by a non-linear function $f(x, \theta)$ with p parameters $\theta = [\theta_0, \ldots, \theta_{p-1}]$ and a normally distributed error term $\epsilon(x)$, I have the equation:

$$y(x) = f(x, \theta) + \epsilon(x). \tag{B.1}$$

The fitting procedure consists of finding the parameters θ so that the following expression is minimised (following Seber and Wild [117]):

$$S(\theta) = \sum_x [y(x) - f(x, \theta)]^2. \tag{B.2}$$

The optimal parameters $\hat{\theta}_i$ are those where the derivative of $S(\theta)$ with respect to θ_i equals zero:

$$\left.\frac{\partial S(\theta)}{\partial \theta_i}\right|_{\hat{\theta}_i} = 0. \tag{B.3}$$

The variance $\mathrm{Var}(\hat{\theta})$ can be obtained using methods from linear regression [120]. Later in this section, I will show these methods can be generalised to the non-linear case. A linear regression problem can formulated as a matrix equation:

$$\mathbf{Y} = \mathbf{X}\boldsymbol{\beta} + \epsilon, \tag{B.4}$$

$$\begin{pmatrix} Y_1 \\ Y_2 \\ \vdots \\ Y_n \end{pmatrix} = \begin{pmatrix} x_{10} & x_{11} & x_{12} & \cdots & x_{1,p-1} \\ x_{20} & x_{21} & x_{22} & \cdots & x_{2,p-1} \\ \vdots & \vdots & \vdots & \vdots & \vdots \\ x_{n0} & x_{n1} & x_{n2} & \cdots & x_{n,p-1} \end{pmatrix} \begin{pmatrix} \boldsymbol{\beta}_0 \\ \boldsymbol{\beta}_1 \\ \vdots \\ \boldsymbol{\beta}_{p-1} \end{pmatrix} + \begin{pmatrix} \varepsilon_1 \\ \varepsilon_2 \\ \vdots \\ \varepsilon_n \end{pmatrix}, \tag{B.5}$$

where $\mathbf{Y}$ is a vector of length n, $\mathbf{X}$ a matrix of dimension $n \times p$, $\boldsymbol{\beta}$ is a vector of length p and ϵ a vector of length n. Thus each value in $\mathbf{Y}$ corresponds to one measured data point, each value in $\mathbf{X}$ to an experimental parameter, each value in $\boldsymbol{\beta}$ to an unknown parameter to be estimated, and each value in $\boldsymbol{\epsilon}$ to an error of that measurement. In order to find the best fit $\boldsymbol{\beta}$, I minimise the squared error term $\boldsymbol{\epsilon}^T\boldsymbol{\epsilon}$ with respect to $\boldsymbol{\beta}$ (this is equivalent to Equation (B.2)). I therefore write:

$$\begin{aligned} \boldsymbol{\epsilon}^T\boldsymbol{\epsilon} &= (\mathbf{Y} - \mathbf{X}\boldsymbol{\beta})^T(\mathbf{Y} - \mathbf{X}\boldsymbol{\beta}) && \text{(B.6)} \\ &= \mathbf{Y}^T\mathbf{Y} - \boldsymbol{\beta}^T\mathbf{X}^T\mathbf{Y} - \mathbf{Y}^T\mathbf{X}\boldsymbol{\beta} + \boldsymbol{\beta}^T\mathbf{X}^T\mathbf{X}\boldsymbol{\beta} && \text{(B.7)} \\ &= \mathbf{Y}^T\mathbf{Y} - 2\boldsymbol{\beta}^T\mathbf{X}^T\mathbf{Y} + \boldsymbol{\beta}^T\mathbf{X}^T\mathbf{X}\boldsymbol{\beta}. && \text{(B.8)} \end{aligned}$$

In equation (B.7), I used that $\mathbf{Y}^T\mathbf{X}\boldsymbol{\beta} = (\boldsymbol{\beta}^T\mathbf{X}^T\mathbf{Y})^T = \boldsymbol{\beta}^T\mathbf{X}^T\mathbf{Y}$ (note that the product is a single number and so equal to its transpose). Differentiating with respect to $\boldsymbol{\beta}$ and setting $\partial\boldsymbol{\epsilon}^T\boldsymbol{\epsilon}/\partial\boldsymbol{\beta}|_{\hat{\boldsymbol{\beta}}} = 0$, I obtain the condition:

$$\begin{aligned} \mathbf{X}^T\mathbf{X}\hat{\boldsymbol{\beta}} &= \mathbf{X}^T\mathbf{Y} && \text{(B.9)} \\ \Rightarrow \hat{\boldsymbol{\beta}} &= (\mathbf{X}^T\mathbf{X})^{-1}\mathbf{X}^T\mathbf{Y}. && \text{(B.10)} \end{aligned}$$

In order to obtain the variance of the estimated parameters $\hat{\boldsymbol{\beta}}$, I simply use Equation (B.10):

$$\begin{aligned}
\mathrm{Var}[\hat{\boldsymbol{\beta}}] &= \mathrm{Var}[(\mathbf{X}^T\mathbf{X})^{-1}\mathbf{X}^T\mathbf{Y}] && \text{(B.11)}\\
&= \left(\mathbf{X}^T\mathbf{X}\right)^{-1}\mathbf{X}^T\,\mathrm{Var}[\mathbf{Y}]\mathbf{X}\left(\mathbf{X}^T\mathbf{X}\right)^{-1} && \text{(B.12)}\\
&= \sigma^2\left(\mathbf{X}^T\mathbf{X}\right)^{-1}\left(\mathbf{X}^T\mathbf{X}\right)\left(\mathbf{X}^T\mathbf{X}\right)^{-1} && \text{(B.13)}\\
&= \sigma^2\left(\mathbf{X}^T\mathbf{X}\right)^{-1}. && \text{(B.14)}
\end{aligned}$$

In Equation (B.12), I used the following matrix properties:

$$\mathrm{Var}[\mathbf{A}\mathbf{Y}] = \mathbf{A}\,\mathrm{Var}[\mathbf{Y}]\mathbf{A}^T \tag{B.15}$$

$$[(\mathbf{X}^T\mathbf{X})^{-1}\mathbf{X}^T]^T = \mathbf{X}(\mathbf{X}^T\mathbf{X})^{-1}. \tag{B.16}$$

In order to estimate the variance $\mathrm{Var}[\mathbf{Y}] = \sigma^2$, I use the population variance $s^2 = (\mathbf{Y} - \mathbf{X}\boldsymbol{\beta})^T(\mathbf{Y} - \mathbf{X}\boldsymbol{\beta})$ (for the full derivation see Seber and Lee [120]):

$$\sigma^2 \approx \frac{s^2}{n-p}. \tag{B.17}$$

I thus obtain the final expression

$$\mathrm{Var}[\hat{\boldsymbol{\beta}}] \approx \frac{s^2}{n-p}\left(\mathbf{X}^T\mathbf{X}\right)^{-1}. \tag{B.18}$$

I can follow a similar procedure to estimate the variance of the parameters of a non-linear fit, by linearising the fitted function around the true value of the parameters θ^* [117]:

$$f(x,\theta) \approx f(x,\theta^*) + \sum_i^{p-1} \left.\frac{\partial f}{\partial \theta_i}\right|_{x,\theta^*}(\theta_i - \theta^*). \tag{B.19}$$

I can now rewrite equation (B.1) as a linear matrix equation:

$$\mathbf{Y} \approx \mathbf{f}(\theta^*) + \mathbf{F}\boldsymbol{\beta} + \boldsymbol{\epsilon}. \tag{B.20}$$

where I have defined:

$$\mathbf{F} = [F_{i,j}] = \left[\left. \frac{\partial f_i}{\partial \theta_j} \right|_{x,\theta^*} \right] \tag{B.21}$$

$$\boldsymbol{\beta} = (\theta - \theta^*). \tag{B.22}$$

F is known as the Jacobian matrix of $f(x, \theta)$. I can visualise Equation (B.20) as:

$$\begin{pmatrix} Y_1 - f(x_1, \theta^*) \\ Y_2 - f(x_2, \theta^*) \\ \vdots \\ Y_n - f(x_n, \theta^*) \end{pmatrix} = \begin{pmatrix} F_{10} & F_{11} & F_{12} & \cdots & F_{1,p-1} \\ F_{20} & F_{21} & F_{22} & \cdots & F_{2,p-1} \\ \vdots & \vdots & \vdots & \vdots & \vdots \\ F_{n0} & F_{n1} & F_{n2} & \cdots & F_{n,p-1} \end{pmatrix} \begin{pmatrix} (\theta_0 - \theta_0^*) \\ (\theta_1 - \theta_1^*) \\ \vdots \\ (\theta_{p-1} - \theta_{p-1}^*) \end{pmatrix} + \begin{pmatrix} \varepsilon_1 \\ \varepsilon_2 \\ \vdots \\ \varepsilon_n \end{pmatrix}. \tag{B.23}$$

Defining $\mathbf{Z} \equiv \mathbf{Y} - \mathbf{f}(\theta^*)$ I can rewrite: Equation (B.20) as

$$\mathbf{Z} \approx \mathbf{F}\boldsymbol{\beta} + \boldsymbol{\epsilon}. \tag{B.24}$$

One sees that Equation (B.24) is identical to the linear case, and if $\hat{\theta}$ are the parameters that best estimate θ^* their variance is given by an expression similar to Equation (B.18):

$$\text{Var}(\hat{\theta}) = \text{Var}(\hat{\boldsymbol{\beta}}) = \sigma^2 (\hat{\mathbf{F}}^T \hat{\mathbf{F}})^{-1} \tag{B.25}$$

$$\sigma^2 = \frac{1}{n-p} \boldsymbol{\epsilon}^T \boldsymbol{\epsilon}, \tag{B.26}$$

where I have defined

$$\hat{\mathbf{F}} = \left[\left. \frac{\partial f_i}{\partial \theta_j} \right|_{x,\hat{\theta}} \right] \tag{B.27}$$

$$\hat{\boldsymbol{\beta}} = (\theta - \hat{\theta}). \tag{B.28}$$

References

[1] E.F. Haussecker and A.W. Chao. "The influence of accelerator science on physics research". In: *Physics in Perspective* 13.2 (2011), pp. 146–160. ISSN: 14226944. DOI: 10.1007/s00016-010-0049-y.

[2] Lord Rutherford and Received February. "Experiments with high velocity positive ions. Further developments in the method of obtaining high velocity positive ions." In: 136.I (1932), pp. 229–243.

[3] D. Guénot, D. Gustas, A. Vernier, et al. "Relativistic electron beams driven by kHz single-cycle light pulses". In: *Nature Photonics* 11.5 (2017), pp. 293–296. ISSN: 17494893. DOI: 10.1038/nphoton.2017.46. arXiv: 1611.09543.

[4] F Salehi, M Le, and H M Milchberg. "Acceleration of quasi-mono-energetic electron bunches to 5 MeV at 1 kHz with few-cycle laser pulses". In: *Frontiers in Optics Laser Science APS/DLS*. Optical Society of America, 2019, JW4A.116. DOI: 10.1364/FIO.2019.JW4A.116. URL: http://www.osapublishing.org/abstract.cfm?URI=FiO-2019-JW4A.116.

[5] Marie Ouillé, Aline Vernier, Frederik Böhle, et al. "Relativistic-intensity near-single-cycle light waveforms at kHz repetition rate". In: *Light: Science and Applications* 9.1 (2020). ISSN: 20477538. DOI: 10.1038/s41377-020-0280-5. URL: http://dx.doi.org/10.1038/s41377-020-0280-5.

[6] M W. Lin. “Development of laser wakefield electron acceleration driven by high-repetition rate ultrafast lasers”. In: *Asia-Pacific Conference on Plasma Physics* (2020), p. 2020.

[7] A. Picksley, A. Alejo, J. Cowley, et al. “Guiding of high-intensity laser pulses in 100-mm-long hydrodynamic optical-field-ionized plasma channels”. In: *Physical Review Accelerators and Beams* 23.8 (2020), p. 81303. ISSN: 24699888. DOI: 10.1103/PhysRevAccelBeams.23.081303. URL: https://doi.org/10.1103/PhysRevAccelBeams.23.081303.

[8] R J Shalloo, C Arran, L Corner, et al. “Hydrodynamic optical-field-ionized plasma channels”. In: *Physical Review E* 97.5 (2018), p. 053203. ISSN: 2470-0045. DOI: 10.1103/PhysRevE.97.053203. URL: https://link.aps.org/doi/10.1103/PhysRevE.97.053203.

[9] R J Shalloo, C Arran, A Picksley, et al. “Low-density hydrodynamic optical-field ionized plasma channels generated with an axicon lens”. In: *Physical Review Accelerators and Beams* (2019), pp. 10–15.

[10] T. Tajima and J.M. Dawson. “Laser electron accelerator”. In: *Physical Review Letters* 4.4 (1979), pp. 267–270. ISSN: 00319007. DOI: 10.1103/PhysRevLett.43.267.

[11] E. Esarey, C. B. Schroeder, and W. P. Leemans. “Physics of laser-driven plasma-based electron accelerators”. In: *Reviews of Modern Physics* (2009). ISSN: 00346861. DOI: 10.1103/RevModPhys.81.1229.

[12] F. Chen. *Introduction to plasma physics and controlled fusion*. Springer International Publishing, 2015. ISBN: 9783319223094. URL: https://books.google.co.uk/books?id=mFg-CwAAQBAJ.

[13] B. Holzer. “Plasma wake acceleration”. In: *Cern Accelerator School*. 2016. DOI: 10.5170/CERN-2016-001.

[14] L.M. Gorbunov and V.I. Kirsanov. “Excitation of plasma waves by an electromagnetic wave packet”. In: *Sov. Phys. JETP* 66.290-294 (1987), p. 40.

[15] J. R. Marques, F. Dorchies, F. Amiranoff, et al. “Laser wakefield: experimental study of nonlinear radial electron oscillations”. In: *Physics of Plasmas* 1162.October (1997). DOI: 10.1063/1.873001.

[16] J.M. Dawson. “Nonlinear electron oscillations in a cold plasma”. In: *The Physical Review* 113.2 (1959), pp. 383–387. ISSN: 0029-5582.

[17] G.A. Mourou, T. Tajima, and S.V. Bulanov. “Optics in the relativistic regime”. In: *Reviews of Modern Physics* 78.2 (2006). ISSN: 00346861. DOI: 10.1103/RevModPhys.78.309.

[18] A. Butler, D. J. Spence, and S.M. Hooker. “Guiding of high-intensity laser pulses with a hydrogen-filled capillary discharge waveguide”. In: *Physical Review Letters* 89.18 (2002). DOI: 10.1103/PhysRevLett.89.185003.

[19] C. G. Durfee III and H. M. Milchberg. “Light pipe for high intensity laser pulses”. In: *Physical Review Letters* 71.15 (1993), pp. 2409–2412. DOI: 10.1103/PhysRevLett.71.2409.

[20] C. G. Durfee, J. Lynch, and H. M. Milchberg. “Development of a plasma waveguide for high-intensity laser pulses”. In: *Physical Review E* 51.3 (1995). DOI: 10.1103/PhysRevE.51.2368.

[21] N. Lemos, T. Grismayer, L. Cardoso, et al. “Plasma expansion into a waveguide created by a linearly polarized femtosecond laser pulse”. In: *Physics of Plasmas* 20.063102 (2013). ISSN: 1070664X. DOI: 10.1063/1.4810797.

[22] R J Shalloo, C Arran, L Corner, et al. “Hydrodynamic optical-field-ionized plasma channels”. In: *Physical Review E* 97.5 (2018), p. 053203. ISSN: 2470-0045. DOI: 10.1103/PhysRevE.97.053203. URL: https://link.aps.org/doi/10.1103/PhysRevE.97.053203.

[23] R. J. Shalloo, C. Arran, A. Picksley, et al. “Low-density hydrodynamic optical-field-ionized plasma channels generated with an axicon lens”. In: *Physical Review Accelerators and Beams* 22.4 (2019), p. 41302. ISSN: 24699888. DOI: 10.1103/PhysRevAccelBeams.22.041302. URL: https://doi.org/10.1103/PhysRevAccelBeams.22.041302.

[24] A. Picksley, A. Alejo, R. J. Shalloo, et al. “Meter-scale conditioned hydrodynamic optical-field-ionized plasma channels”. In: *Physical Review E* 102.5 (2020), p. 53201. ISSN: 24700053. DOI: 10.1103/PhysRevE.102.053201. arXiv: 2008.13683. URL: https://doi.org/10.1103/PhysRevE.102.053201.

[25] K. Nakajima, D. Fisher, T. Kawakubo, et al. “Observation of ultrahigh gradient electron acceleration by a self-modulated intense short laser pulse”. In: *Physical Review Letters* 74.22 (1995), pp. 4428–4431. ISSN: 00319007. DOI: 10.1103/PhysRevLett.74.4428.

[26] A. Modena, Z. Najmudin, A.E. Dangor, et al. “Electron acceleration from the breaking of relativistic plasma waves”. In: *Nature* 377.6550 (1995), pp. 606–608.

[27] R Wagner, S. Chen, A. Maksimchuk, and D. Umstadter. “Acceleration by a laser wakefield in a relativistically self-guided channel”. In: *Physical Review Letters* (1997).

[28] V. Malka, S. Fritzler, E. Lefebvre, et al. “Electron acceleration by a wake field forced by an intense ultrashort laser pulse”. In: *Science* 298.5598 (2002), pp. 1596–1600. ISSN: 00368075. DOI: 10.1126/science.1076782.

[29] S. P. D. Mangles, C. D. Murphy, Z. Najmudin, et al. “Monoenergetic beams of relativistic electrons from intense laser–plasma interactions”. In: *Nature* 431 (2004), pp. 535–538. DOI: 10.1038/nature02939.

[30] J. Faure, Y. Glinec, A. Pukhov, et al. “A laser-plasma accelerator producing monoenergetic electron beams”. In: *Nature* 431.September (2004), pp. 541–544.

[31] C. G. R. Geddes, J. V. Tilborg, E. Esarey, et al. “High-quality electron beams from a laser wakefield accelerator using plasma-channel guiding”. In: 431.September (2004), pp. 538–541. ISSN: 0028-0836. DOI: 10.1038/nature02900.

[32] W. P. Leemans, B. Nagler, A. J. Gonsalves, et al. “GeV electron beams from a centimetre-scale accelerator”. In: *Nature Physics* 2.10 (2006), pp. 696–699. ISSN: 17452473. DOI: 10.1038/nphys418.

[33] S. Kneip, S. R. Nagel, S. F. Martins, et al. “Near-GeV acceleration of electrons by a nonlinear plasma wave driven by a self-guided laser pulse”. In: *Physical Review Letters* (2009). ISSN: 00319007. DOI: 10.1103/PhysRevLett.103.035002.

[34] X. Wang, R. Zgadzaj, N. Fazel, et al. “Quasi-monoenergetic laser-plasma acceleration of electrons to 2 GeV”. In: *Nature Communications* 4.May (2013). ISSN: 20411723. DOI: 10.1038/ncomms2988.

[35] H.T. Kim, K. H. Pae, H. J. Cha, et al. “Enhancement of electron energy to the multi-GeV regime by a dual-stage laser-wakefield accelerator pumped by petawatt laser pulses”. In: *Physical Review Letters* 111.16 (2013). ISSN: 00319007. DOI: 10.1103/PhysRevLett.111.165002. arXiv: 1307.4159.

[36] W. P. Leemans, A. J. Gonsalves, H. S. Mao, et al. “Multi-Gev electron beams from capillary-discharge-guided subpetawatt laser pulses in the self-trapping regime”. In: *Physical Review Letters* 113.24 (2014), pp. 1–5. ISSN: 10797114. DOI: 10.1103/PhysRevLett.113.245002.

[37] Z. Najmudin. “Laser wakefield accelerators”. In: *Proceedings of the CAS-CERN Accelerator School: Plasma Wake Acceleration, Geneva, Switzerland, 23-29 November 2014*. Ed. by B Holzer. Vol. 001. CERN, 2016, pp. 109–118.

[38] N. Lemos, T. Grismayer, L. Cardoso, et al. “Effects of laser polarization in the expansion of plasma waveguides”. In: *Physics of Plasmas* 20 (2013). DOI: 10.1063/1.4825228.

[39] M. N. Rosenbluth and C. S. Liu. “Excitation of plasma waves by two laser beams”. In: *Physical Review Letters* 29.11 (1972).

[40] A. E. Dangor, A. K.L. Dymoke-Bradshaw, and A. E. Dyson. “Observation of relativistic plasma waves generated by the beat-wave with 1 μm lasers”. In: *Physica Scripta* 1990.T30 (1990), pp. 107–109. ISSN: 14024896. DOI: 10.1088/0031-8949/1990/T30/015.

[41] F. Amiranoff, M. Laberge, J.R. Marques, et al. “Observation of Modulational Instability in Nd-Laser Beat-Wave Experiments”. In: *Physical Review Letters* 68.25 (1992).

[42] C.E. Clayton, K. A. Marsh, A. Dyson, et al. “Ultrahigh-gradient acceleration of injected electrons by laser-excited relativistic electron plasma waves”. In: *Physical Review Letters* 70.1 (1993), pp. 37–40. DOI: 10.1103/PhysRevLett.70.37.

[43] E. Esarey, J. Krall, and P. Sprangle. “Envelope analysis of intense laser pulse self-modulation in plasmas”. In: *Physical Review Letters* 72.18 (1994), pp. 2887–2890. ISSN: 00319007. DOI: 10.1103/PhysRevLett.72.2887.

[44] C. A. Coverdale, C. B. Darrow, C. D. Decker, et al. “Propagation of intense subpicosecond laser pulses through underdense plasmas”. In: *Physical Review Letters* 74.23 (1995), pp. 4659–4662. ISSN: 00319007. DOI: 10.1103/PhysRevLett.74.4659.

[45] D. Strickland and G. Mourou. “Compression of amplified chirped optical pulses”. In: *Optical communications* 56 (1985), pp. 219–221. ISSN: 00304018. DOI: 10.1016/0030-4018(85)90120-8.

[46] C. E. Clayton, J. E. Ralph, F. Albert, et al. “Self-guided laser wakefield acceleration beyond 1 GeV using ionization-induced injection”. In: *Physical Review Letters* 105.10 (2010), pp. 3–6. ISSN: 00319007. DOI: 10.1103/PhysRevLett.105.105003. arXiv: 1511.02280.

[47] N. A. M. Hafz, T. M. Jeong, I. W. Choi, et al. “Stable generation of GeV-class electron beams from self-guided laser-plasma channels”. In: *Nature Photonics* 2.9 (2008), pp. 571–577. ISSN: 17494885. DOI: 10.1038/nphoton.2008.155.

[48] A J Gonsalves, K Nakamura, J Daniels, et al. “Petawatt laser guiding and electron beam acceleration to 8 GeV in a laser-heated capillary discharge waveguide”. In: *Physical Review Letters* 122.8 (2019), p. 84801. ISSN: 1079-7114. DOI: 10.1103/PhysRevLett.122.084801. URL: https://doi.org/10.1103/PhysRevLett.122.084801.

[49] W. P. Leemans, R. Duarte, E. Esarey, et al. “The Berkeley lab laser accelerator (BELLA): A 10 GeV laser plasma accelerator”. In: *AIP Conference Proceedings* 1299.November (2010), pp. 3–11. ISSN: 0094243X. DOI: 10.1063/1.3520352.

[50] P. A. Walker. “Horizon 2020 EuPRAXIA Design Study”. In: *Journal of Physics: Conference Series* 874 (2017), p. 012029. DOI: 10.1088/1742-6596/874/1/012029.

[51] S. Breitkopf, T. Eidam, A. Klenke, et al. “A concept for multiterawatt fibre lasers based on coherent pulse stacking in passive cavities”. In: *Light: Science and Applications* 3.10 (2014). ISSN: 20477538. DOI: 10.1038/lsa.2014.92.

[52] S. M. Hooker, R. Bartolini, S. P. D. Mangles, et al. “Multi-pulse laser wakefield acceleration: a new route to efficient, high-repetition-rate plasma accelerators and high flux radiation sources”. In: *Arxiv* 234003.23 (2014), p. 1401.7874. ISSN: 0953-4075. DOI: 10.1088/0953-4075/47/23/234003. arXiv: 1401.7874.

[53] G. Mourou, B. Brocklesby, T. Tajima, and J. Limpert. “The future is fibre accelerators”. In: 7.April (2013), pp. 1–4. DOI: 10.1038/nphoton.2013.75. URL: http://dx.doi.org/10.1038/nphoton.2013.75.

[54] S. Zhou, D. G. Ouzounov, and F. W. Wise. “Divided-pulse amplification of ultrashort pulses”. In: *Conference on Lasers and Electro-Optics, 2007, CLEO*

2007 32.7 (2007), pp. 871–873. ISSN: 0146-9592. DOI: 10.1109/CLEO.2007.4453041.

[55] C. W. Siders, J. L. W. Siders, A. J. Taylor, S.-G. Park, and A. M. Weiner. "Efficient high-energy pulse-train generation using a 2n-pulse Michelson interferometer". In: *Applied Optics* 37.22 (1998), p. 5302. ISSN: 0003-6935. DOI: 10.1364/AO.37.005302. URL: https://www.osapublishing.org/abstract.cfm?URI=ao-37-22-5302.

[56] R. J. Shalloo, L. Corner, C. Arran, et al. "Generation of laser pulse trains for tests of multi-pulse laser wakefield acceleration". In: *Nuclear Instruments and Methods in Physics Research, Section A: Accelerators, Spectrometers, Detectors and Associated Equipment* 829 (2016), pp. 383–385. ISSN: 01689002. DOI: 10.1016/j.nima.2016.02.044. URL: http://dx.doi.org/10.1016/j.nima.2016.02.044.

[57] J Cowley, C Thornton, C Arran, et al. "Excitation and control of plasma wakefields by multiple laser pulses". In: *Physical Review Letters* (2017), pp. 1–6. DOI: 10.1103/PhysRevLett.119.044802. arXiv: arXiv:1708.04206v1.

[58] D. Umstadter, J. Kim, E. Esarey, E. Dodd, and T. Neubert. "Resonantly laser-driven plasma waves for electron acceleration". In: *Physical Review E* 51.4 (1995).

[59] J. Vieira, R. A. Fonseca, W. B. Mori, and L. O. Silva. "Ion motion in self-modulated plasma wakefield accelerators". In: *Physical Review Letters* 109.14 (2012), pp. 1–5. ISSN: 00319007. DOI: 10.1103/PhysRevLett.109.145005. arXiv: arXiv:1208.3242v1.

[60] S. M. Hooker, R. Bartolini, S. P. D. Mangles, et al. "Multi-pulse laser wakefield acceleration : a new route to efficient, high-repetition-rate plasma accelerators and high flux radiation sources". In: *Journal of Physics B: Atomic, Molecular and Optical Physics* 47 (2014). DOI: 10.1088/0953-4075/47/23/234003.

[61] E. Adli, A. Ahuja, O. Apsimon, et al. “Acceleration of electrons in the plasma wakefield of a proton bunch”. In: *Nature* 561 (2018), pp. 4–9. DOI: 10.1038/s41586-018-0485-4.

[62] I. H. Hutchinson. “Principles of plasma diagnostics: second edition”. In: *Plasma Physics and Controlled Fusion* 44.12 (2002), p. 2603. DOI: 10.1088/0741-3335/44/12/701.

[63] F. I. Parra. *Lecture notes: wave propagation in an inhomogeneous plasma.* Tech. rep. University of Oxford, 2019.

[64] C. B. Schroeder, C. Benedetti, E. Esarey, J. Van Tilborg, and W. P. Leemans. “Group velocity and pulse lengthening of mismatched laser pulses in plasma channels”. In: *Physics of Plasmas* 18.8 (2011). ISSN: 1070664X. DOI: 10.1063/1.3609778.

[65] J. Van Tilborg, J. Daniels, A. J. Gonsalves, et al. “Measurement of the laser-pulse group velocity in plasma waveguides”. In: *Physical Review E - Statistical, Nonlinear, and Soft Matter Physics* 89.6 (2014), pp. 1–5. ISSN: 15502376. DOI: 10.1103/PhysRevE.89.063103.

[66] J. Daniels, J. Van Tilborg, A. J. Gonsalves, et al. “Plasma channel diagnostics for capillary discharges”. In: *AIP Conference Proceedings* 1777.October 2016 (2016). ISSN: 15517616. DOI: 10.1063/1.4965661.

[67] J. Van Tilborg, A. J. Gonsalves, E. Esarey, C. B. Schroeder, and W. P. Leemans. “High-sensitivity plasma density retrieval in a common-path second-harmonic interferometer through simultaneous group and phase velocity measurement”. In: *Phys. Plasmas* 26 (2019). DOI: 10.1063/1.5080269.

[68] O. Kafri and I. Glatt. *The physics of moiré metrology.* Wiley New York, 1990.

[69] J. W. Goodman. *Introduction to Fourier optics.* Roberts and Company Publishers, 2005.

[70] S. Yokozeki and T. Suzuki. “Shearing interferometer using the grating as the beam splitter part 2”. In: *Applied Optics* 10.7 (1971), p. 1690. ISSN: 0003-6935. DOI: 10.1364/ao.10.001690.

[71] A. W. Lohmann and D. E. Silva. “An interferometer based on the Talbot effect”. In: *Optics Communications* 2.9 (1971), pp. 413–415. ISSN: 00304018. DOI: 10.1016/0030-4018(71)90055-1.

[72] S. K. H. Auluck. “High-sensitivity diffraction-compensated moire deflectometry”. In: *Journal of Modern Optics* (1994). DOI: 10.1080/09500349414550801.

[73] M. Takeda, H. Ina, and S. Kobayashi. “Fourier-transform method of fringe-pattern analysis for computer-based topography and interferometry”. In: *Journal of the Optical Society of America* 72.1 (1982), p. 156. ISSN: 0030-3941. DOI: 10.1364/JOSA.72.000156. URL: https://www.osapublishing.org/abstract.cfm?URI=josa-72-1-156.

[74] P. Tomassini, A. Giulietti, L. A. Gizzi, et al. “Analyzing laser plasma interferograms with a continuous wavelet transform ridge extraction technique: the method”. In: *Applied optics* 40.35 (2001), pp. 6561–6568.

[75] M. Stéphane. *A wavelet tour of signal processing.* Third edit. Boston: Academic Press, 2009, pp. 89–153. ISBN: 978-0-12-374370-1. DOI: https://doi.org/10.1016/B978-0-12-374370-1.00008-2. URL: http://www.sciencedirect.com/science/article/pii/B9780123743701000082.

[76] K. Itoh. “Analysis of the phase unwrapping algorithm”. In: *Applied Optics* 21.14 (1982), p. 2470. ISSN: 0003-6935. DOI: 10.1364/ao.21.002470.

[77] R. M. Goldstein, H. A. Zebker, and C. L. Werner. “Satellite radar interferometry: Two-dimensional phase unwrapping”. In: *Radio Science* 23.4 (1988), pp. 713–720. ISSN: 1944799X. DOI: 10.1029/RS023i004p00713.

[78] M. A. Herraez, D. R. Burton, M. J. Lalor, and M. A. Gdeisat. "Fast two-dimensional phase-unwrapping algorithm based on sorting by reliability following a noncontinuous path". In: *Applied Optics* 41.35 (2002), p. 7437. ISSN: 0003-6935. DOI: 10.1364/ao.41.007437.

[79] A.M. Cormack. "Representation of a foundation by its line with some radiological application." In: *J. Appl. Phys* 34.10 (1963), pp. 2722–2727.

[80] N. H. Abel. "Auflösung einer mechanischen Aufgabe." In: *Journal für die reine und angewandte Mathematik* 1826.1 (1826), pp. 153–157. DOI: https://doi.org/10.1515/crll.1826.1.153. URL: https://www.degruyter.com/view/journals/crll/1826/1/article-p153.xml.

[81] A. A. Kovalev, V. V. Kotlyar, and A. P. Porfirev. "Asymmetric Laguerre Gaussian beams". In: *Physical Review A* 93.6 (2016), pp. 1–10. ISSN: 24699934. DOI: 10.1103/PhysRevA.93.063858.

[82] P. S. Kolhe and A. K. Agrawal. "Abel inversion of deflectometric data : comparison of accuracy and noise propagation of existing techniques". In: *Applied Optics* 20 (2009).

[83] G. Sarri, K. L. Lancaster, R. Trines, et al. "Creation of persistent, straight, 2 mm long laser driven channels in underdense plasmas". In: *Physics of Plasmas* 17.11 (2010). ISSN: 1070664X. DOI: 10.1063/1.3505305.

[84] R. Kodama, K. Mima, K. A. Tanaka, et al. "Fast ignitor research at the Institute of Laser Engineering, Osaka University". In: *Physics of Plasmas* 8.5 II (2001), pp. 2268–2274. ISSN: 1070664X. DOI: 10.1063/1.1352598.

[85] K. A. Tanaka, R. Kodama, H. Fujita, et al. "Studies of ultra-intense laser plasma interactions for fast ignition". In: *Physics of Plasmas* 7.5 II (2000), pp. 2014–2022. ISSN: 1070664X. DOI: 10.1063/1.874023.

[86] H. Habara, S. Ivancic, K. Anderson, et al. “Efficient propagation of ultra-intense laser beam in dense plasma”. In: *Plasma Physics and Controlled Fusion* 57.6 (2015). ISSN: 13616587. DOI: 10.1088/0741-3335/57/6/064005.

[87] B T Spiers, M P Hill, C Brown, et al. “Whole-beam self-focusing in fusion-relevant plasma Subject Areas :” in: *Phil. Trans. R. Soc. A* 379 (2021), p. 20200159. URL: https://doi.org/10.1098/rsta.2020.0159.

[88] C. N. Lashmore-Davies. “The relationship between modulational instability and oscillating two-stream instability”. In: *Nuclear Fusion* 15.2 (1975), pp. 213–216. ISSN: 17414326. DOI: 10.1088/0029-5515/15/2/005.

[89] C S Liu and V K Tripathi. *Interaction of electromagnetic waves with electron beams and plasmas*. World Scientific, 1995.

[90] V. E. Zakharov and L. A. Ostrovsky. “Modulation instability: the beginning”. In: *Physica D: Nonlinear Phenomena* 238.5 (2009), pp. 540–548. ISSN: 01672789. DOI: 10.1016/j.physd.2008.12.002. URL: http://dx.doi.org/10.1016/j.physd.2008.12.002.

[91] V. P. Silin. “Parametric resonance in a plasma”. In: *Soviet Journal of Experimental and Theoretical Physics* 21.6 (1965), p. 1127. ISSN: 1063-7761.

[92] V. P. Silin. “Kinetic instability of a plasma located in a strong high frequency field”. In: 24.6 (1967), pp. 1242–1247.

[93] J. R. Sanmartin. “Electrostatic plasma instabilities excited by a high-frequency electric field”. In: *Physics of Fluids* 13.6 (1970), pp. 1533–1542. ISSN: 10706631. DOI: 10.1063/1.1693114.

[94] P. Mora, D. Pesme, A Heron, G. Laval, and N Silvestre. “Modulational instability and its consequences for the beat-wave accelerator”. In: *Physical Review Letters* 61.14 (1988), pp. 1611–1614.

[95] S. G. Thornhill and D. ter Haar. “Langmuir turbulence and modulational instability”. In: *Physics Reports* 43.2 (1978), pp. 43–99. ISSN: 03701573. DOI: 10.1016/0370-1573(78)90142-4.

[96] Paul M Bellan. *Fundamentals of plasma physics.* Cambridge University Press, 2006. DOI: 10.1017/CBO9780511807183.

[97] J. W. Banks, S. Brunner, R. L. Berger, and T. M. Tran. “Vlasov simulations of electron-ion collision effects on damping of electron plasma waves”. In: *Physics of Plasmas* 23.3 (2016). ISSN: 10897674. DOI: 10.1063/1.4943194. arXiv: 1601.01002. URL: http://dx.doi.org/10.1063/1.4943194.

[98] D. B. Melrose. “Plasma formulary”. In: *Instabilities in Space and Laboratory Plasmas* (2011), pp. xi–xii. DOI: 10.1017/cbo9780511564123.002.

[99] M. C. Downer, R. Zgadzaj, A. Debus, U. Schramm, and M. C. Kaluza. “Diagnostics for plasma-based electron accelerators”. In: *Reviews of Modern Physics* 90.3 (2018), p. 035002. ISSN: 0034-6861. DOI: 10.1103/RevModPhys.90.035002. URL: https://link.aps.org/doi/10.1103/RevModPhys.90.035002.

[100] J. B. Rosenzweig, D.B. Cline, B Cole, et al. “Experimental observation of plasma wake-field acceleration”. In: *Physical Review Letters* 61.1 (1988), pp. 98–101.

[101] C. J. Zhang, J. F. Hua, Y. Wan, et al. “Femtosecond probing of plasma wakefields and observation of the plasma wake reversal using a relativistic electron bunch”. In: *Physical Review Letters* 064801.August (2017), pp. 1–6. DOI: 10.1103/PhysRevLett.119.064801.

[102] S. Y. Chen, M. Krishnan, A. Maksimchuk, and D. Umstadter. “Excitation and damping of a self-modulated laser wakefield”. In: *Physics of Plasmas* 7.1 (2000), pp. 403–413. ISSN: 1070664X. DOI: 10.1063/1.873809.

[103] N. H. Matlis, S. Reed, S. S. Bulanov, et al. “Snapshots of laser wakefields”. In: *Nature Physics* 2 (2006), pp. 749–753. DOI: 10.1038/nphys442.

[104] N.H. Matlis, A. Maksimchuk, V. Yanovsky, W.P. Leemans, and M.C. Downer. “Analysis of sinusoidally modulated chirped laser pulses by temporally encoded spectral shifting”. In: *Optics Letters* 41.23 (2016), pp. 1–4. ISSN: 15394794 01469592. DOI: 10.1364/OL.41.005503.

[105] C. Arran. “Techniques for high repetition rate laser wakefield acceleration”. DPhil thesis. University of Oxford, 2018.

[106] C. D. Murphy, R. Trines, J. Vieira, et al. “Evidence of photon acceleration by laser wake fields”. In: *Physics of Plasmas* 13.3 (2006), pp. 1–8. ISSN: 1070664X. DOI: 10.1063/1.2178650.

[107] Hideyuki Kotaki, Masaki Kando, Takatsugu Oketa, et al. “Direct measurement of coherent ultrahigh wakefields excited by intense ultrashort laser pulses in a gas-jet plasma”. In: *Physics of Plasmas* 9.4 (2002), p. 1392. ISSN: 1070664X. DOI: 10.1063/1.1457464.

[108] T. D. Arber, K. Bennett, C. S. Brady, et al. “Contemporary particle-in-cell approach to laser-plasma modelling”. In: *Plasma Physics and Controlled Fusion* 57.11 (2015). ISSN: 13616587. DOI: 10.1088/0741-3335/57/11/113001.

[109] Alistair L.-D. “Ionisation effects for laser-plasma interactions by particle-in-cell code”. PhD thesis. University of Warwick, 2013. URL: https://core.ac.uk/download/pdf/18174584.pdf.

[110] M. B. Shah, D. S. Elliott, and H. B. Gilbody. “Pulsed crossed-beam study of the ionisation of atomic hydrogen by electron impact”. In: *Journal of Physics B: Atomic and Molecular Physics* 20.14 (1987), pp. 3501–3514. ISSN: 00223700. DOI: 10.1088/0022-3700/20/14/022.

[111] L. Spitzer Jr. *Physics of fully ionized gases*. English. N.Y.: Dover Publications, 2006. ISBN: 0486449823 9780486449821.

[112] J. Derouillat, A. Beck, F. Pérez, et al. "SMILEI: A collaborative, open-source, multi-purpose particle-in-cell code for plasma simulation". In: *Computer Physics Communications* 222.February (2018), pp. 351–373. ISSN: 00104655. DOI: 10.1016/j.cpc.2017.09.024. arXiv: 1702.05128.

[113] V. Malka, A. Modena, Z. Najmudin, et al. "Second harmonic generation and its interaction with relativistic plasma waves driven by forward Raman instability in underdense plasmas". In: *Physics of Plasmas* 4.4 (1997), pp. 1127–1131. ISSN: 1070664X. DOI: 10.1063/1.872201.

[114] *ISO 11146-1:2005(en) Lasers and laser-related equipment — Test methods for laser beam widths, divergence angles and beam propagation ratios.* 2005. URL: https://www.iso.org/obp/ui/{\#}iso:std:iso:11146:-1:ed-1:v1:en.

[115] S. D. E. Silvestri, P. Laporta, and O. Svelto. "The role of cavity dispersion in CW mode-locked lasers". In: *Journal of Quantum Electronics* 5 (1984).

[116] M. Polyanskiy. *Refractiveindex.Info.* 2020. URL: http://refractiveindex.info/?shelf=main{\&}book=Cu{\&}page=Rakic{\%}5Cnhttp://refractiveindex.info/?shelf=main{\&}book=Cu{\&}page=Rakic.

[117] G. A. F. Seber and C. J. Wild. *Nonlinear regression.* Wiley-Interscience, 2003.

[118] M. Bertero and P. Boccacci. *Introduction to inverse problems in imaging.* IOP Publishing, 1998.

[119] A. Bret, L. Gremillet, and M. E. Dieckmann. "Multidimensional electron beam-plasma instabilities in the relativistic regime". In: *Physics of Plasmas* 17.12 (2010), pp. 9–11. ISSN: 1070664X. DOI: 10.1063/1.3514586.

[120] G. A. F. Seber and A. J. Lee. *Linear regression analysis.* Second edi. Wiley-Interscience, 2003.